Eclogite and blueschist in the Southern New England Fold Belt:

P–T–t conditions and long-lived subduction on the Gondwanan eastern margin

Thesis submitted in accordance with the requirements of the University of Adelaide for an Honours Degree in Geology

Renée Jade Tamblyn
November 2016

THE UNIVERSITY *of* ADELAIDE

ECLOGITE AND BLUESCHIST IN THE SOUTHERN NEW ENGLAND FOLD BELT: P–T–T CONDITIONS AND LONG-LIVED SUBDUCTION ON THE GONDWANAN EASTERN MARGIN

RUNNING TITLE: Eclogite and blueschist in eastern Gondwana

ABSTRACT

Eclogite and blueschist in the Tasminides represent clear evidence for subduction-related metamorphism on the Gondwanan eastern margin during the Palaeozoic. These eclogites and blueschists are located in the serpentinite-bearing Peel Manning Fault System in the Southern New England Fold Belt (SNEFB) of eastern Australia. U–Pb zircon and Lu–Hf and Sm–Nd multimineral geochronology give ages of ca. 490 Ma for lawsonite-bearing eclogite and ca. 470 Ma for garnet-bearing blueschist at Port Macquarie in the SNEFB, in agreement with Cambro-Ordovician dates for eclogite metamorphism across the eastern Gondwanan margin. In combination with this, Ar–Ar data dates exhumation and cooling in the subduction channel at ca. 460 Ma, suggesting that high-pressure metamorphism at Port Macquarie was continuously active for upwards of 40 Ma. This is supported by mineral equilibria forward modeling, which demonstrates that 24–27 kbar eclogite from Port Macquarie and Pigna Barney in the SNEFB experienced high-pressure but low-temperature retrograde paths, consistent with their residence in the subduction channel. Geochemical and isotopic results suggest that MORB as well as oceanic arc-related material was subducted and metamorphosed in a westwards dipping subduction system on the Australian cratonic margin during the ca. 515–490 Ma Delamerian Orogeny, and subsequently entrapped in the subduction channel during rollback. This rollback resulted in the development of a large backarc system on the upper plate in which the protoliths to the Lachlan Orogen accumulated, as well as on-going blueschist-facies metamorphism in the subduction channel. Ultimately, rollback led to translocation of subduction products and their exhumation over 2000 km eastwards to their current position in the New England orogen. In contrast to this, further south in Tasmania and Antarctica, the subduction of continental material led to

rapid burial and exhumation of eclogite, representing differing styles of Cambro-Ordovician high-pressure metamorphism on the eastern Gondwanan margin.

KEYWORDS

Eclogite, blueschist, subduction, high-pressure, metamorphism, Gondwana, Southern New England Fold Belt, pseudosection

TABLE OF CONTENTS

LIST OF FIGURES AND TABLES

INTRODUCTION

Metamorphism along low geothermal gradients produces eclogite and blueschist facies rocks, which are commonly interpreted to record paleosubduction. Such rocks exist in eastern Australia, and represent clear evidence for subduction-related high-pressure (high-P) metamorphism on the Gondwanan eastern margin throughout the Paleozoic (Shaw and Flood, 1974; Allan and Leitch, 1992; Offler, 1999; Phillips and Offler, 2011; Phillips *et al.,* 2015). Eclogites and associated blueschists outcrop as exotic blocks in the serpentinite-bearing Peel Manning Fault System (PMFS) of the predominately Carboniferous–Permian Southern New England Fold Belt (SNEFB; Fig. 1; Och *et al.,* 2003; Phillips and Offler, 2011; Nutman *et al.,* 2013; Phillips *et al.,* 2015). Eclogite also occurs within supracrustal rocks in central Tasmania and northern Victoria Land in Antarctica (Fig. 1; Di Vincenzo and Palmeri, 2001; Di Vincenzo *et al.,* 2009; Palmeri *et al.,* 2009; Palmeri *et al.,* 2011), and demonstrates the existence of subduction responsible for the development of the Tasminides of eastern Gondwana.

In the SNEFB eclogite facies metamorphism has been dated at 515–490 Ma (Phillips *et al.,* 2015), suggesting that these eclogites and blueschists predate much of the development of the Ordovician–Silurian Tasman Fold Belt, which lies to the west of the southern New England Fold Belt (Fig. 1; Glen *et al.,* 2013). These ages also indicate that high-P metamorphism was approximately coeval with the Cambrian–Ordovician Delamerian Orogeny, which lies to the west of the Tasman Fold Belt (Offler, 1999;

Foden, 2006; Phillips, 2010; Phillips and Offler, 2011). The coincidence in age between the high heat flow Delamerian system and the SNEFB eclogites suggests that they may have been geodynamically linked, with the high-P metamorphism recording the forearc system and the Delamerian system the backarc (Sandiford *et al.,*1992; Phillips *et al.,* 2015). The current position of the high-P rocks now east of the Tasman Fold Belt (Fig. 1) is interpreted to reflect slab rollback, which migrated the locus of subduction-related metamorphism eastwards along with each orogenic stage (e.g. Phillips *et al.,* 2015). This model provides a simple geodynamic scenario that contrasts with the often complex models put forward to explain the development of the Tasman Fold Belt, which involve several collisions and subduction reversals (e.g. Aitchison and Buckman, 2012). Implicit in the rollback model is that west-dipping subduction on the east Gondwanan margin was ongoing, with the possibility that high-P rocks could remain trapped in the forearc position during rollback, transporting them ~2000 km eastwards (e.g. Gerya *et al.,* 2002; Krebs *et al.,* 2009; Baitsch-Ghirardello *et al.,* 2014). This
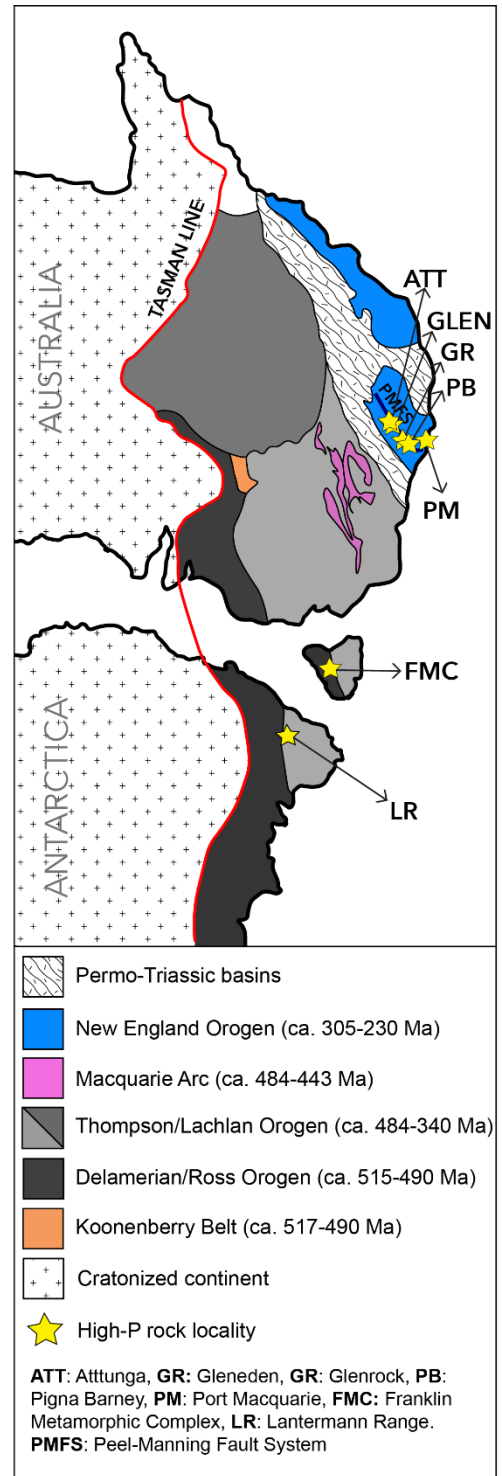
Fig. 1: Relative position of Australia, Tasmania and Antarctica on the Gondwanan eastern margin throughout the Paleozoic. The red line demonstrates the cratonic margin of these continents, whereas related accretionary orogens are marked in shades.

entrapment provides a possible explanation for age differences of ca. 30 Ma between peak eclogite metamorphism and Ar–Ar cooling ages reflecting exhumation from garnet-bearing blueschists in the SNEFB (Phillips *et al.,* 2015).

However, to confound this simple geodynamic scenario, Nutman *et al.* (2013) argued on the basis of interpreted detrital zircon ages that eclogite, and associated high-P rocks at Port Macquarie in the easternmost SNEFB (Fig. 2), was early Triassic (ca. 251 Ma) in age. If a Triassic age for eclogite facies metamorphism at Port Macquarie is correct, it means there are geodynamically distinct eclogite bearing systems in the SNEFB. A further implication of this interpretation is that subduction products continued to be accreted to the Carboniferous–Permian oroclinally-deformed architecture of the southern New England Fold Belt during the early Mesozoic (Rosenbaum *et al.,* 2012; Li and Rosenbaum, 2014). However, the inferred age of eclogite facies metamorphism at Port Macquarie is difficult to reconcile with the regional geology (e.g. Och *et al.,* 2003), and there are no direct age constraints on the metamorphism.

The primary aim of this study is to determine the age of lawsonite-bearing eclogite and associated garnet-bearing blueschist at Port Macquarie using the Lu–Hf and Sm–Nd systems, as well as U–Pb ages from metamorphic zircon to resolve the age of peak metamorphism. Although the presence of serpentinite hosted eclogite and blueschist exotic blocks in the SNEFB has been known for some time, there are no robust constraints on the *P–T* conditions that these rocks experienced. This is partly due to retrograde overprinting, and the presence of high-variance assemblages that are not suited for conventional thermobarometry. Therefore, the second aim of this study is to

undertake mineral equilibria forward modelling on eclogite from Port Macquarie and newly discovered eclogite (this study) at Pigna Barney to place constraints on the thermobarometric regimes experienced by the high-P rocks in the SNEFB. Lastly, analysis of Sm–Nd isotopes from the protoliths to the high-P rocks at Port Macquarie are used to identify the affinities of the metamorphic precursors. These combined methods will allow a thorough interpretation of the timing and setting of high-P metamorphism on the Gondwanan eastern margin, and thus the geodynamics of subduction and accretion during the Paleozoic.

GEOLOGICAL BACKGROUND

The Southern New England Fold Belt

The Tasminides of eastern Australia consist of the Delamerian (515–490 Ma), Lachlan (484–340 Ma), and New England (305–230 Ma) orogens, adjoining from the cratonic margin in the west to the youngest expression of subduction in the east known as the New England Orogen (NEO; Fig. 1; Glen, 2005; Kemp *et al.,* 2009; Glen, 2013). The NEO spans the eastern edge of Australia, and is separated into north and south segments by the overlying Clarence-Moreton Basin, and bound to the west by the Bowen, Gunnedah and Sydney basins (Fig. 2; Leitch, 1974, Cawood *et al.,* 2011). The orogen itself is divided into three components: a Devonian–Carboniferous volcanic arc in the west, a forearc basin, and the accretionary wedge to the east. The arc is obscured by younger sedimentary strata in the south (Jenkins *et al.,* 2002).
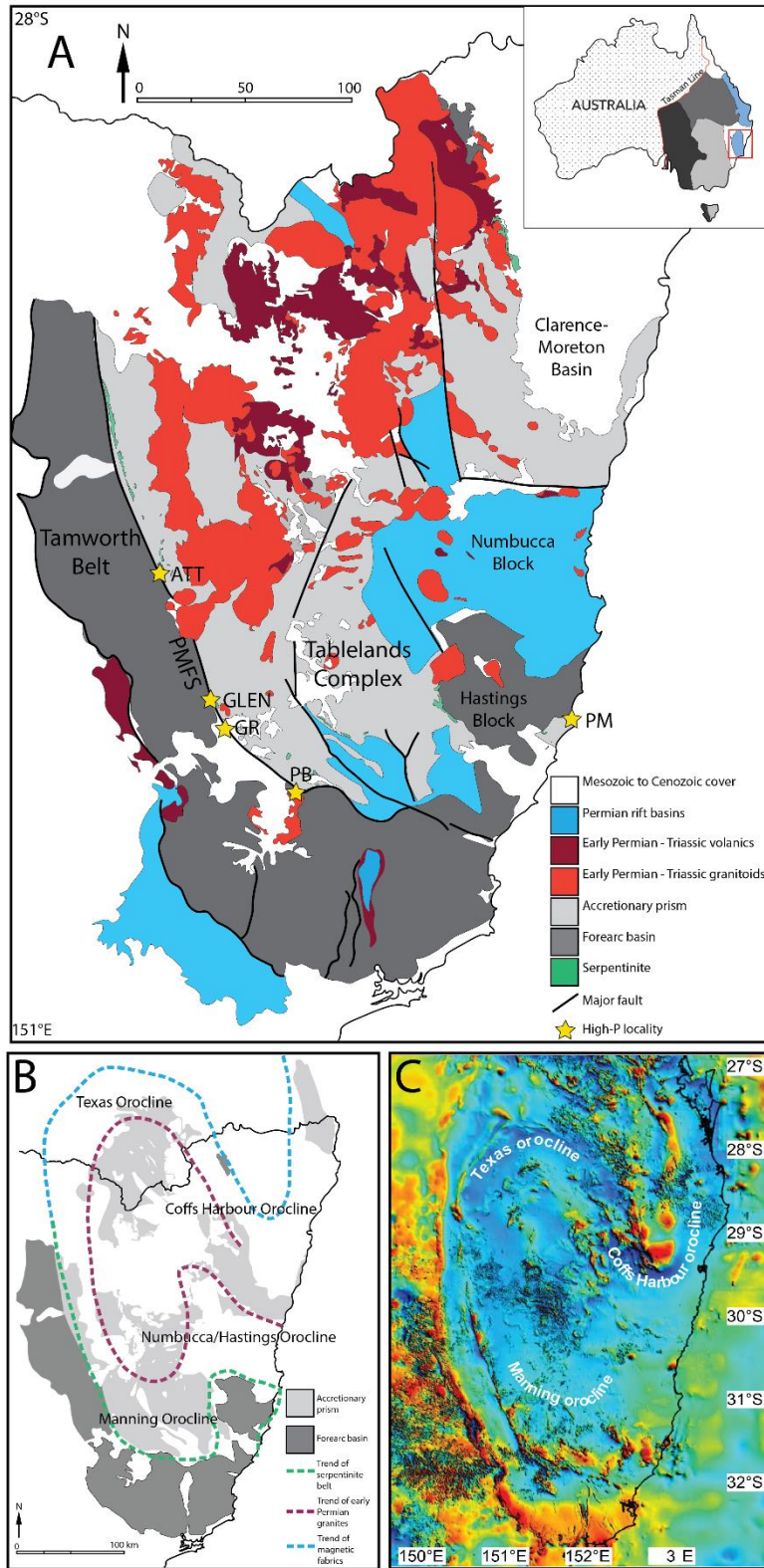
Fig. 2: A) Geological map of the Southern New England Fold Belt (SNEFB). ATT: Attunga; GLEN: Gleneden; GR: Glenrock, PB: Pigna Barney; PM: Port Macquarie; PMFS: Peel Manning Fault System. B) Trace of interpreted oroclines in the SNEFB after Li and Rosenbaum (2012), blue representing magnetic fabrics, maroon the trace of Permian granites, and green the trace of the serpentinite belt. C) Total magnetic intensity of the SNEFB, with oroclines annotated, after Li and Rosenbaum (2012).

In this southern segment (referred to as the SNEFB) the Tamworth Belt, representing the Late Devonian–Carboniferous forearc basin, and the Tablelands complex, representing the Silurian–Carboniferous accretionary complex, are separated by the serpentinite-bearing Peel Manning Fault System (PMFS; Fig. 2; Leitch, 1974; Aitchison and Ireland, 1995; Jenkins *et al.,* 2002). A Devonian oceanic arc complex (the Gamilaroi terrane) outcrops in the forearc belt (Jenkins *et al.,* 2002). Rocks of the forearc experienced gentle deformation at zeolite–prehnite–pumpyellyite facies (Leitch, 1974; Offler *et al.,* 1998; Offler and Hand, 1998). East of the PMFS the accretionary complex consists of multiply deformed, steeply dipping zeolite–greenschist and blueschist facies rocks (Offler and Hand, 1998; Phillips *et al.,* 2010). The SNEFB also contains numerous felsic magmatic rocks of the Permian–Triassic New England Batholith, which intrude the Tablelands Complex and Early Permian Bernard Basin (Leitch, 1974; Shaw and Flood, 1981; Phillips *et al.*, 2011). These are interpreted to represent a period of crustal extension and increased thermal gradient, coincident with change from an accretionary orogen to backarc system (Leitch *et al.,* 1993; Jenkins *et al.,* 2002; Phillips *et al.,* 2011).

Subsequent to its formation, the SNEFB has been deformed into four major oroclines (Fig. 2b; Li and Rosenbaum, 2012; Rosenbaum *et al.,* 2012). The Manning and Numbucca/Hastings oroclines contort the serpentinite belt that exhumes the high-P exotic blocks, adding further complexity to their relationship with the enclosing geology.

High-pressure localities

High-P metamorphism in the SNEFB has been recorded at Attunga, Gleneden, Glenrock, Pigna Barney and Port Macquarie (Fig. 2), and investigated by a number workers (Table 1; Allan and Leitch, 1992; Fukui *et al.,* 1995; Wantanabe *et al.*, 1999; Phillips and Offler, 2001; Sano *et al.,* 2004; Hyodo, 2008; Phillips, 2010; Och *et al.,* 2010; Nutman *et al.,* 2013; Phillips *et al.,* 2015). Peak eclogite facies metamorphism at Attunga has been constrained in the mid to late Cambrian (Phillips *et al.,* 2015), whereas cooling associated with exhumation has been dated from high-P blocks across the SNEFB in the Ordovician–Silurian (Fukui *et al.,* 1995; Sano *et al.,* 2004; Och *et al.,* 2010; Phillips, 2010; Phillips and Offler, 2011; Phillips *et al.,* 2015). Geodynamically related eclogites outcrop in the Franklin Metamorphic Complex of Tasmania and in the Lantermann Range in North Victoria Land, Antarctica (Fig. 1; Table 1), which preserve similar Cambrian ages of peak metamorphism. However, these eclogites occur closer to the cratonic margin (Fig. 1; Di Vincenzo *et al.,* 1997; Di Vincenzo and Palmeri, 2001; Palmeri *et al.,* 2009), than those preserved in the SNEFB.

Serpentinite hosted high-P rocks at Rocky Beach, Port Macqaurie (Fig. 2), have been described in detail by Och *et al.* (2003). They occur as metre to decimetre blocks of lawsonite-garnet eclogite, blueschist conglomerate, omphacite–garnet eclogite, granofelsic omphacite, garnet-bearing blueschist and massive blueschist, encased in chlorite–actinolite schist (Fig. 3). Ordovician (ca. 470 Ma) K–Ar ages have been obtained from late-stage phengite from the blueschists, interpreted as cooling associated with exhumation (Fukui *et al.,* 1995). In contrast, Nutman *et al.* (2013) dated zircons interpreted to be detrital within the eclogite protoliths, to provide an apparent

13
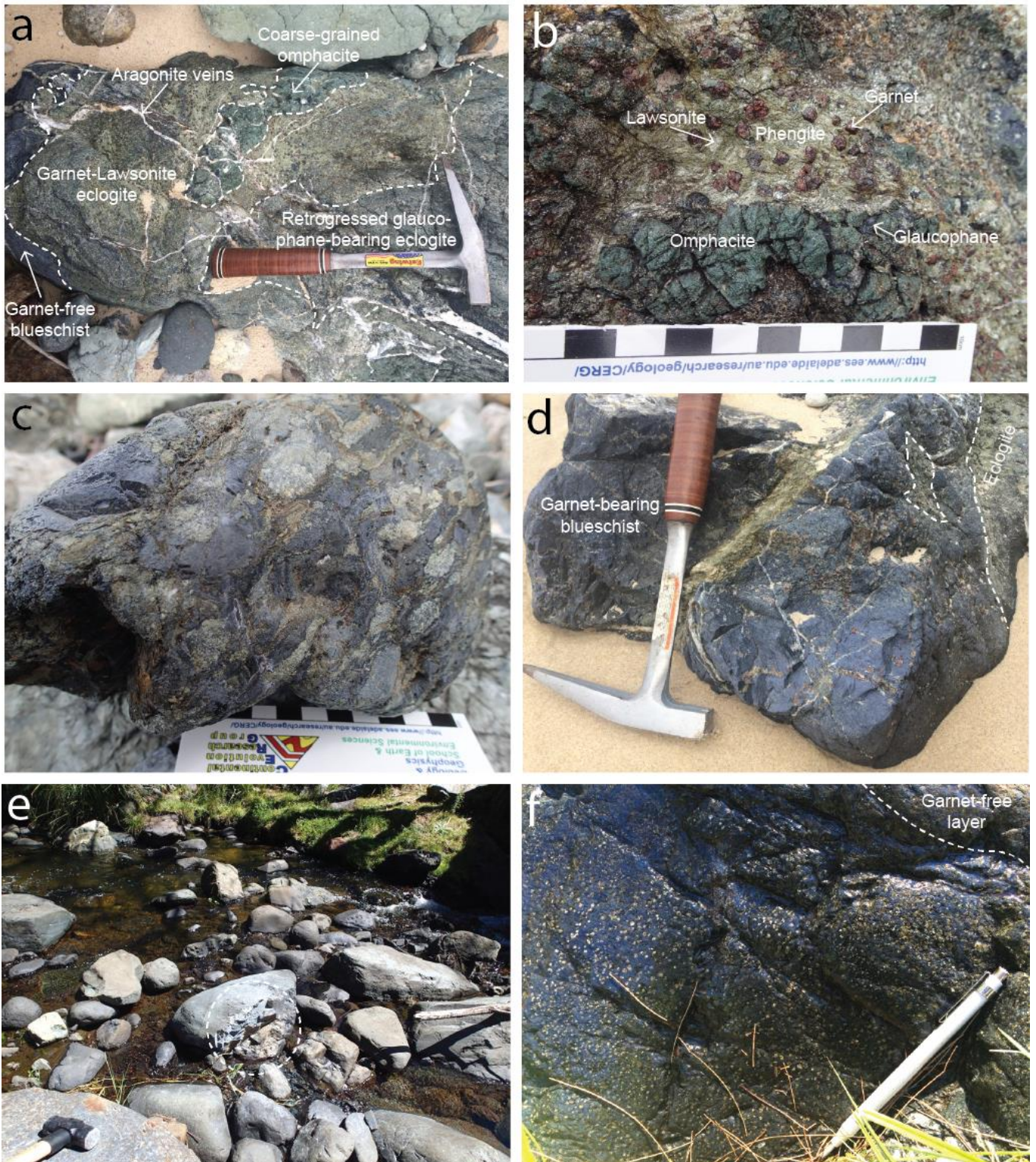
Fig. 3: A) Relationships of intermingled high-pressure rock types at Rocky Beach, Port Macquarie, including garnet–lawsonite eclogite sample RB11. **B)** Lawsonite bearing eclogite at Port Macquarie (RB11), sampled for geochronology and forward modelling. **C)** Blueschist conglomerate sampled from Port Macquarie, sampled for whole rock Sm–Nd analyses (RB05, RB06 and RB07). **D)** Garnet-bearing blueschist sampled for geochronology (RB12) from Port Macquarie. **E)** Boulders of blueschist in the river at Pigna Barney with the location of newly discovered eclogite marked by circle (PB16) sampled for forward modelling. **F)** Garnet-rich layer in blueschist at Pigna Barney.

maximum possible age for eclogite metamorphism of 251±6 Ma, attributing older K–Ar

ages to excess argon. Och *et al.* (2003) obtained *P–T* conditions for the eclogite

metamorphism of ~18 kbar and 560 °C using conventional thermobarometry and

rudimentary *P–T* grids, and lower-*T* conditions of ~360–450 °C for blueschist

metamorphism. Alternatively, Nutman *et al.* (2013) suggested that the eclogites and

blueschists experienced the same *P–T* history, with maximum conditions less than 450

°C and 10 kbar. They argued the blueschist-eclogite transition is controlled by

differences in bulk composition of the protolith.

Blueschist at Pigna Barney (Fig. 2) has been described by Cross (1983), Offler, (1999),

and Phillips *et al.* (2015). Fine to medium-grained glaucophane schist is hosted by

serpentinite as an accumulation of meter-scale blueschist blocks (Fig.3), ~200 m long

and ~50 m wide. The schist occasionally contains relict garnet and lawsonite, and in this

study a small domain of relict omphacite–lawsonite–garnet eclogite was found within

the blueschist. Single grain phengite Ar–Ar ages of 482±2 Ma have been obtained from

the blueschist (Phillips *et al.,* 2015), which is in agreement with other K–Ar and Ar–Ar

ages from blueschist at Pigna Barney and Glenrock Station, northwest along the PMFS,

interpreted to reflect cooling and exhumation (Fig. 2; Fukui *et al.,* 1995; Sano *et al.,*

2004; Phillips, 2010; Phillips and Offler, 2011). Conventional thermobarometry

estimates pressures of ~7.5 kbar and temperatures of 300–350 °C have been obtained

for the blueschists (Phillips *et al.,* 2015).

Table 1: Summary of previous work on high-pressure rocks of the eastern Gondwanan margin. Exhumation rate for the Port Macquarie and Lantermann Range rocks is calculated as the rate from peak metamorphism to retrogressional metamorphism associated with exhumation (i.e. retrograde mica overprinting or passing through the 350 °C closure temperature for Ar–Ar in mica). Exhumation rate for the Collingwood River eclogites is calculated from peak metamorphism to time at surface, given by overlying unconformable contacts.

Location	Rock type	Protolith	Temperature	Pressure	Peak age	Retrograde Age	Exhumation Rate
Port Macquarie	Eclogite	MORB	**560 °C** (Och *et al.*, 2003) **450 °C** (Nutman *et al.,* 2013)	**18 kbar** (Och *et al.,* 2003)		**460 Ma (Ar–Ar)** (Phillips unpublished)	**~7 °C/Ma and 0.45 km/Ma** (using data from this study)
	Blueschist	MORB	**450 – 360 °C** (Och *et al.,* 2003, Nutman *et al*, 2013)			**470 Ma (K-Ar)** (Fukui *et al.,*1995)	**~10 °C/Ma**
Pigna Barney	Blueschist	Enriched and normal MORB (Phillips *et al.,* 2015)	**620 – 700 °C (amphibolite)** **300 – 350 °C (blueschist)** (Phillips *et al.,* 2015)	**12.5 – 17.5 kbar (amphibolite)** **7.5 kbar (blueschist)** (Phillips *et al.,* 2015)		**482 Ma (K-Ar)** Fukui *et al.,* 1995 **470 Ma (Ar–Ar)** (Phillips *et al.,* 2015)	
Glenrock	Blueschist	Continental arc (Phillips *et al.,* 2015)	**470 °C** (Phillips and Offler, 2009)	**8.5 – 9 kbar** (Phillips and Offler, 2009)		**473 Ma (K-Ar)** (Fukui *et al.,* 1995) **473 Ma (Ar–Ar)** (Phillips *et al.*, 2015)	
Attunga	Eclogite	T-MORB (Phillips *et al.,* 2015)	**550 °C (eclogite)** **650 – 700 °C (amphibolite)** (Phillips *et al.,* 2015)	**22 kbar (eclogite)** **7.7 – 10 kbar (amphibolite)** (Phillips *et al.,* 2015)	**514 Ma (U–Pb) (eclogite)** **480 Ma (U–Pb) (amphibolite)** (Phillips *et al.,* 2015)	At surface by ca. 270 Ma	
Gleneden	Eclogite	Oceanic tholeiite (Allan and Leitch, 1992)	**384 – 516 °C** (Allan and Leitch, 1992)	**7 – 14 kbar** (Allan and Leitch, 1992)			
Collingwood River (Tasmania)	Eclogite	Ultradepleted lithosphere (Palmeri *et al.,* 2009)	**600 – 650 °C** (Palmeri *et al.,* 2009)	**>15 kbar** (Palmeri *et al.,* 2009)	**510-505 Ma (field relations with schist)** (Berry *et al.,*, 2007)	**By 498 Ma (overlain contact)**	**~54 °C/Ma**
Lantermann Range (Antarctica)	Eclogite	T – E type MORB (Palmeri *et al.,* 2011)	**700 - 850 °C (eclogite)** (Palmeri *et al.,* 2011) **600 - 750 °C (amphibolite)** (Palmeri *et al.,* 2011)	**16 - 34 kbar (eclogite)** (Palmeri *et al.,* 2011) **5 - 11 kbar (amphibolite)** (Palmeri *et al.,* 2011)	**ca. 500 Ma (Sm–Nd)** (Di Vincenzo *et al.,*1997)	**498 – 490 Ma (Ar–Ar amphibole)** (Di Vincenzo and Palmeri, 2001)	**~30 °C/Ma and 5-2 km/Ma** (Di Vincenzo and Palmeri, 2001)

ANALYTICAL METHODS

Zircon U–Pb Geochronology

Zircon U–Pb geochronology was undertaken in-situ on 10–15 μm zircons in sample RB11a, for the purpose of dating metamorphism. Sample preparation and analytical procedures are outlined in Appendix 1a.

Lu–Hf and Sm–Nd Geochronology

Lu–Hf and Sm–Nd isotope analysis was conducted on samples RB11 and RB12. Crushing, magnetic separations, heavy liquid procedures and hand-picking were implemented to obtain pure (>99%) mineral samples. Isotope analysis were undertaken by Robert Anczkiewicz at the Polish Academy of Sciences, Krakow, Poland. Analysis followed the methods of Anczkiewicz and Thirlwall (2003) with modifications for the Lu–Hf method from Anczkiewicz *et al.* (2004).

Rare earth element mapping in garnet

Rare earth and other elements (Ca, Lu, Hf, Sm, Nd, Y) were mapped in garnets from samples RB11 and RB12 to determine zoning profiles and to interpret Sm–Nd and Lu–Hf ages. This was done on an ASI m50 LA–ICP–MS with attached 7700 MS at Adelaide Microscopy. The data was processed in Iolite, using Ca as the index element. Quantitative maps were interrogated using the Matlab script XMapTools (Lanari *et al.*, 2014).

Whole rock Sm–Nd

Whole rock Sm–Nd isotopes were obtained for samples RB05, RB06 and RB07. Samples were first obliterated using a mill head, and isotope ratios obtained by David Bruce at University of Adelaide using the method described by Morrissey *et al.* (2011).

Electron Probe Micro Analyses

Element X-ray maps and mineral composition element analyses were undertaken at Adelaide Microscopy, using a CAMECA SXFive electron microprobe. Operational procedures are presented in Appendix 1b.

Phase Equilibria Forward Modelling

Phase equilibria calculations were undertaken using the software THERMOCALC (Powell and Holland, 1988; Holland and Powell, 2011) in the model chemical system $Na_2O–CaO–K_2O–FeO–MgO–Al_2O_3–SiO_2–H_2O–O$, where 'O' is a proxy for Fe_2O_3, using the internally-consistent thermodynamic dataset 'ds5' (filename tc-ds55.txt; Holland and Powell, 1998) and activity–composition (*a–x*) models (Diener *et al.,* 2012; Green *et al.,* 2007; White *et al.,* 2007; Holland *et al.,* 1998; Holland and Powell, 2003; Holland and Powell, 1998).

Calculations in THERMOCALC are manually completed by the user, involving many trial and error calculations to determine which phases appear or disappear as a function of pressure, temperature and/or rock composition. 'Starting guesses' (compositional variables for phases) need to be understood and constantly updated as calculations are conducted, as in mafic rocks multiple minerals have the ability to jump solvi and approach similar compositions. A single model comprises >150–300 manual

calculations, which can take several months or more for complex models such as metamorphosed mafic rocks. This method is very different to automated approaches, such as Perple_X (Connolly and Petrini, 2002; Connolly, 2005) and Theriac (di Capitani and Petrakakis, 2010) See Appendix 1c for detailed methods.

Phase Abundance Contours

Contouring of phase equilibria models for the normalised abundances ('mode') of phases was calculated using the Matlab-based, automated software TCInvestigator v1.0 (Pearce *et al.,* 2015).

RESULTS

Samples

Table 2: Sample description (coordinates in WGS84, zone 56J).

Location	Rock type	Sample	Description	UTM coordinates
Port Macquarie	Eclogite	*RB11*	Lawsonite-garnet eclogite	0492903, 6521938
	Blueschist	*RB12*	Garnet-bearing blueschist	
	Blueschist conglomerate	*RB05, RB06, RB07*	Lawsonite clasts in a blue and green amphibole matrix	
Pigna Barney	Blueschist	*PB16*	Blueschist with rare relict garnets and lawsonite	0364764, 6482045
	Eclogite	*PB16*	Lawsonite-omphacite-garnet bearing domain in blueschist	

Petrography

RB11

Peak minerals in sample RB11 consist of porphyroblastic lawsonite (up to 7 mm) and garnet (up to 5 mm) in an omphacite, phengite and titanite-bearing matrix (Fig. 4a). The rock contains a well-developed foliation defined by phengite. Lawsonite contains inclusions of early titanite, and garnet contains inclusions of lawsonite, titanite, rutile, apatite, quartz, zircon, and glaucophane that define sigmoidal inclusion trail patterns (Fig. 5a). Garnet is partially pseudomorphed by chlorite, and omphacite by glaucophane. Retrograde minerals include predominately glaucophane and chlorite, but also pyrite, stilpnomelane, phengite and veins of aragonite and quartz (Fig. 4c).

RB12

RB12 blueschist contains ~3 mm garnet porphyroblasts that commonly form in veins or trails (Fig. 4b). Garnets are heavily fractured and pseudomorphed by chlorite. The matrix contains predominately glaucophane, with some minor phengite and quartz. Prismatic rutile is mantled by titanite (Fig. 4d). Calcite, quartz and albite veining with pyrite cross cuts the sample.

RB05, RB06 and RB07

These samples are deformed conglomerates that have been metamorphosed at blueschist facies. However, clasts retain relict primary igneous textures. The rocks consist of pale elongate clasts in an L-type fabric, up to 5 cm on their short axis and 15 cm on their elongate axis (Fig. 3c). These samples have similar mineralogy; the clasts consist of either predominately lawsonite crystals (up to 1 mm) or fine-grained glaucophane, in a matrix of very fine-grained glaucophane, chlorite and titanite.

PB16

Newly discovered eclogite sample PB16 from Pigna Barney contains garnet, omphacite, phengite and lawsonite in one small (~5 cm x ~2 cm) domain of the rock. Garnets are highly fractured and partially pseudomorphed by chlorite, whereas omphacite is partially replaced by glaucophane (Fig. 4e). Fine-grained partial replacements of relict lawsonite (up to 4 mm) contain albite, plagioclase and phengite (Fig. 4f). The blueschist assemblage in PB16 is characterised by abundant glaucophane, which defines a strong foliation and wraps garnet, and less abundant titanite, epidote and actinolite (Fig. 4f).

21
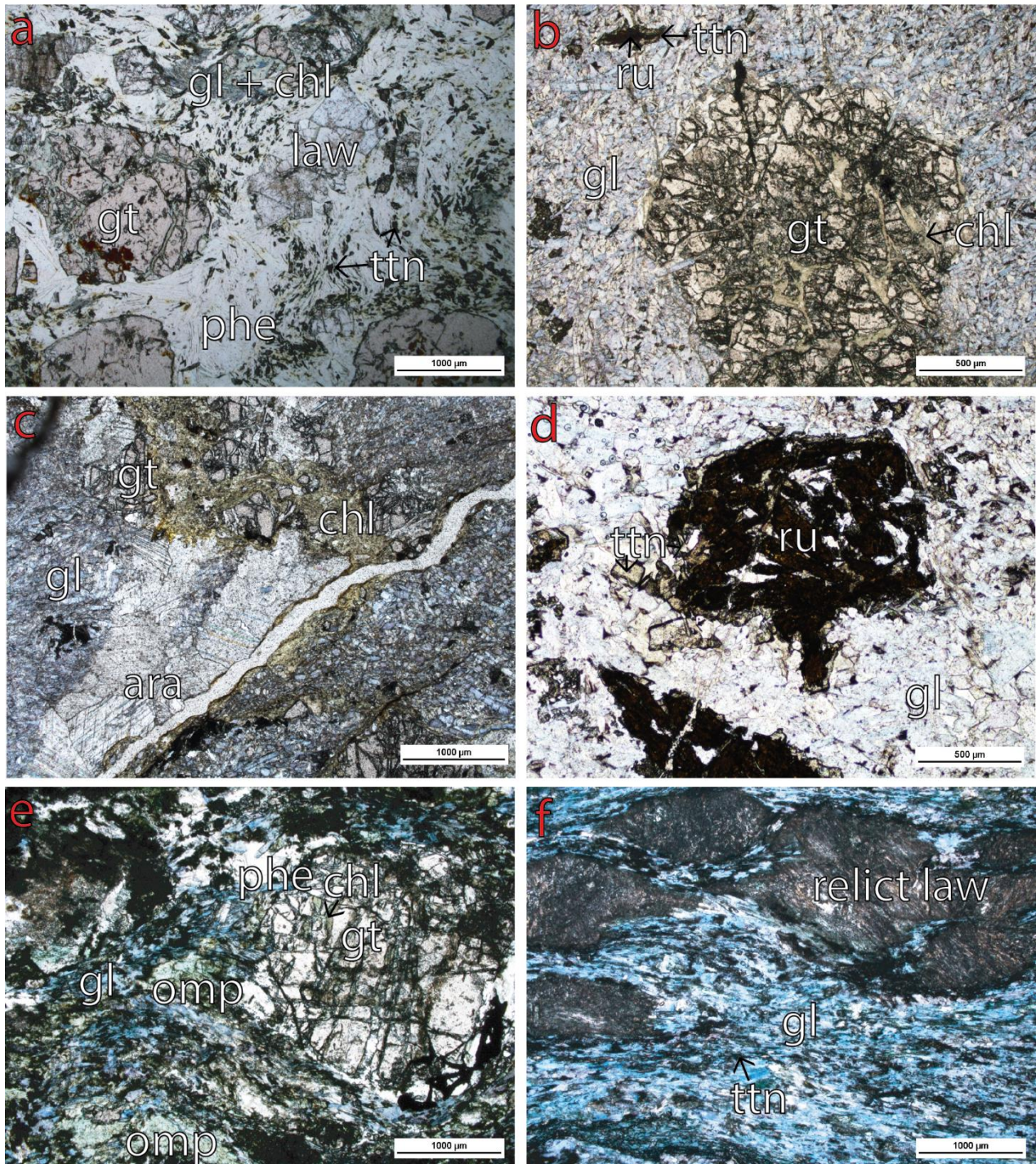
Fig. 4: Photomicrographs of samples from this study. A) Eclogite RB11 in PPL, showing peak eclogitic minerals garnet, lawsonite, phengite and titanite, and a domain of retrograde chlorite and glaucophane. B) Blueschist RB12 in PPL, showing a fractured garnet with chlorite in the fractures, and the predominantly glaucophane matrix. C) Aragonite in a partially retrogressed eclogite from Port Macquarie under PPL. D) Rutile rimmed by titanite in blueschist sample RB12 in PPL, possibly pseudomorphing a protolith Ti bearing mineral such as ilmenite. E) Relict eclogite from sample PB16 in PPL, with phengite, garnet and omphacite partially preserved in a domain, with retrograde chlorite and glaucophane. F) Sample PB16 almost fully retrogressed to blueschist facies, with the predominantly glaucophane + titanite matrix wrapping relict lawsonite pseudomorphs.

Abbreviations: gt: garnet, chl: chlorite, law: lawsonite, phe: phenite, ttn: titanite, gl: glaucophane, ru: rutile, omph: omphacite, arag: aragonite.

Mineral chemistry

Representative analyses of all minerals are listed in Appendix 2a, and summarized in Table 3. The composition of garnet for all samples is dominantly almandine (46–64%) with 27–33% grossular. Samples show spessartine enrichment in cores (10–26%) and almandine enrichments in rims (54–64%; Fig. 5e). Garnets are prograde-zoned (Fig. 5a-d), with Mn enrichments in cores. Garnet from sample RB11a shows oscillatory zonation in Mn, with Fe enrichments in cores and a distinct Mg enrichment in the outermost rims (Fig. 5a, 5e). Blueschist garnets RB12 and PB16 are highly fractured and show little chemical zonation except for Mn (Fig. 5c-d, additional maps in Appendix 2b). The clinopyroxene in eclogite is omphacite (42% diopside, 34–39% jadeite). Mica from Port Macquarie eclogite is phengite (41% celedonite, 24% ferroceledonite, 34% muscovite). Titanite from eclogites contains 0.32–0.36 wt% Al and 0.13–0.14 wt% Fe^{3+}.

Table 3: Representative mineral end-member compositions of garnet, clinopyroxene and mica in samples; values for listed end-members are proportions. Also shown are trace amounts of Fe^{3+} and Al in titanite (in wt%), relevant to phase equilibria calculations (discussed later). X(gt): the $Fe^{2+}/(Fe^{2+} + Mg)$; j(cpx): Na; f(cpx): Fe^{3+} cations; x(cpx): the $Fe^{2+}/(Fe^{2+} + Mg)$ ratio, as defined in the *a-x* model in THERMOCALC.

	RB11		*RB12*		*PB16*	
	Garnet Rim	**Garnet Core**	**Garnet Rim**	**Garnet Core**	**Garnet Rim**	**Garnet Core**
x(gt)	0.94	0.99	0.90	0.93	0.91	0.92
Almandine	0.64	0.46	0.67	0.52	0.54	0.53
Pyrope	0.03	0.01	0.04	0.01	0.00	0.02
Grossular	0.30	0.27	0.24	0.29	0.33	0.33
Spesspartine	0.02	0.26	0.01	0.15	0.07	0.10

	RB11	*PB16*			*RB11*		*RB11*	*PB16*
	Cpx	**Cpx**			**Mica**		**Titanite**	**Titanite**
j (Cpx)	0.47	0.46	Paragonite	0.01		Al	0.36	0.32
f (Cpx)	0.16	0.25	Margarite	0.00		Fe^{3+}	0.14	0.13
x (Cpx)	0.20	0.23	Muscovite	0.34				
Jadeite	0.39	0.34	Celedonite	0.41				
Diopside	0.42	0.42	Ferro-celedonite	0.24				
Hendenbergite	0.11	0.13						
Aegirine	0.08	0.12						
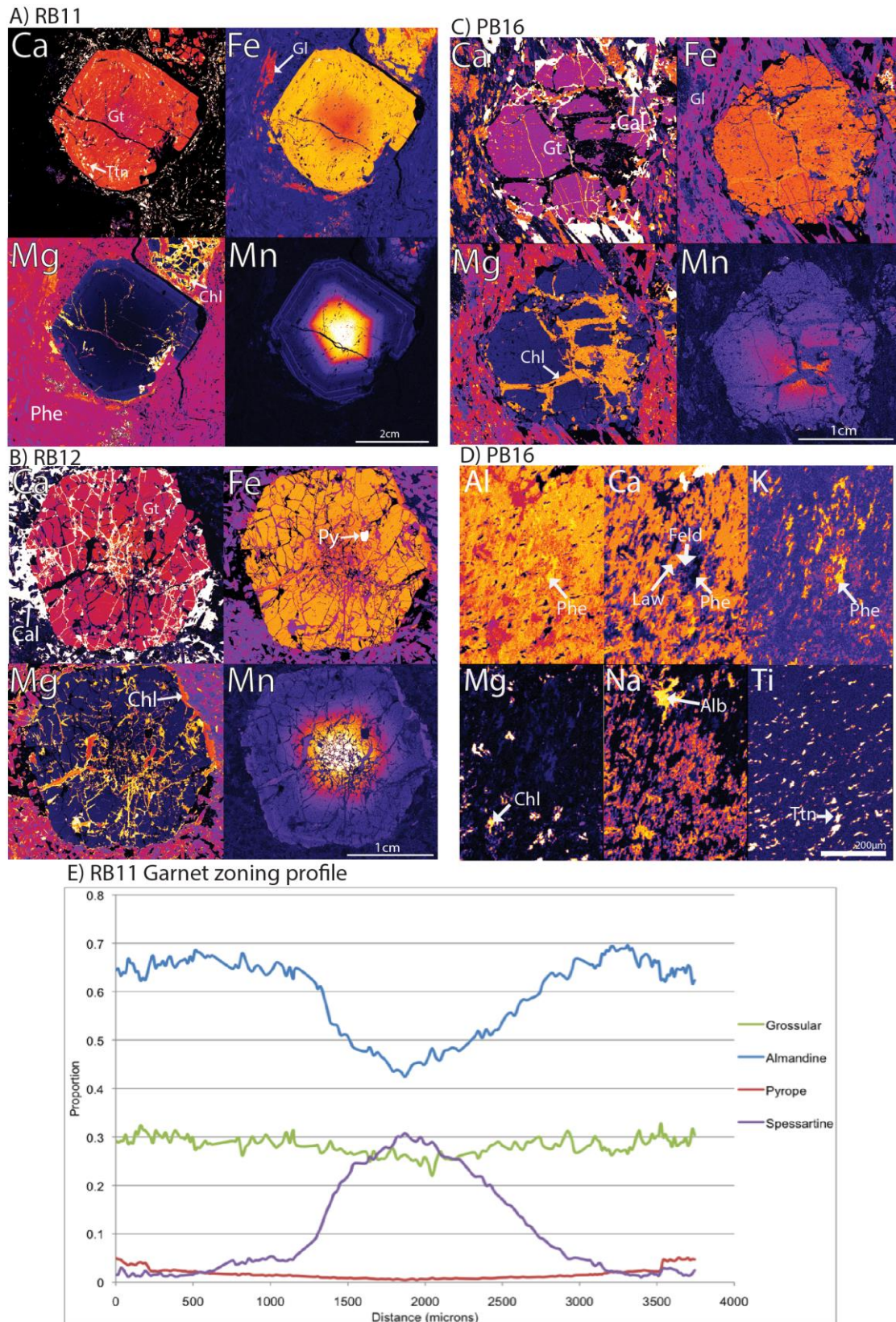
Fig. 5: EPMA Elemental maps, purple indicates low concentration of an element, scaling up to white which represents high concentration of that element. A) Elemental maps of garnet from eclogite RB11; B) Elemental maps of garnet from blueschist RB12; C) Elemental maps of garnet from eclogite PB16; D) Elemental map of fine-grained reaction textures containing albite, mica, lawsonite and Ca-rich feldspar that replaced lawsonite from eclogite PB16; E) Rim to rim traverse across garnet from RB11, showing mineral end-member proportions.

Laser ablation ICP–MS maps

LA–ICP–MS maps of garnet were acquired for samples RB11 and RB12 to identify elemental concentrations and distributions of Lu, Hf, Sm, Nd and Y to aid in the interpretation of Lu–Hf and Sm–Nd ages (Fig. 6). Garnet from RB11 has no discernible zoning in Sm and Nd, but shows inclusion hotspots, interpreted to be titanite, with ~70 ppm Sm and up to 300 ppm Nd. The garnet shows strong enrichment of Lu within ~1.2 mm of the core (up to 11 ppm) and subtle oscillatory zonation towards the rim (from 1 to 4 ppm). Hf concentrations are restricted to inclusion hotspots (up to 60 ppm), which probably represent partial sampling of zircon micro-inclusions, whereas the garnet shows no overall zonation, with Hf concentrations ~5 ppm. Garnet from blueschist sample RB12 is fragmented and retrogressed, and shows similar inclusion hotspots of Sm (~160 ppm) and Nd (~180 ppm) as evident in RB11, most likely titanite. Lu is enriched up to 100 ppm in an irregular pattern in the core, whereas Hf concentrations across the garnet average ~20 ppm.
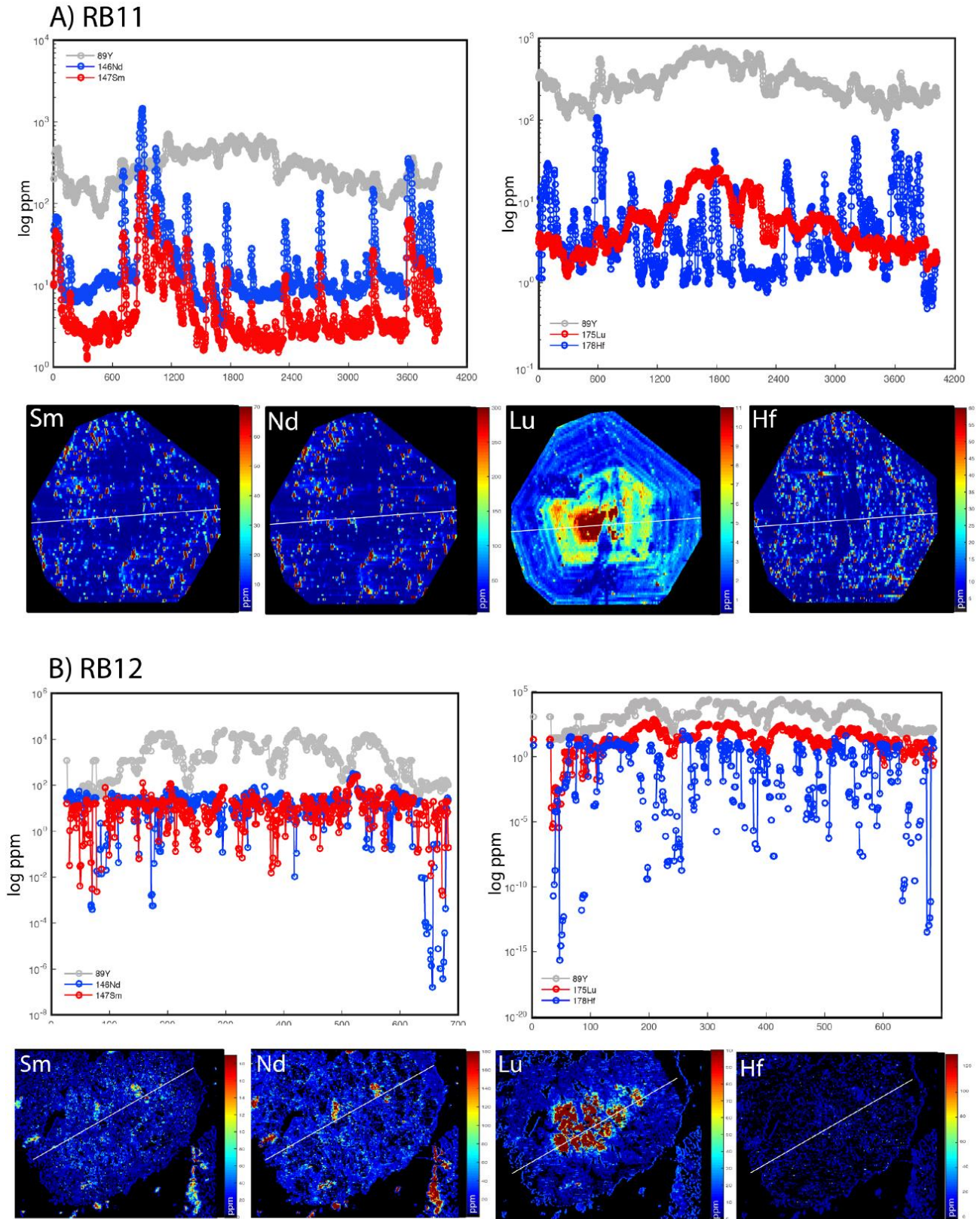
Fig. 6: a and b: Transects across garnets from rim to rim showing Sm and Nd concentrations (left) and Lu and Hf concentrations (right) with Y for reference (grey). Maps show quantitative measurements of these REEs across the entire garnet, with white line showing the location of the transect. RB12 is 700 microns across and RB11 is 4200 microns across.

U–Pb Zircon geochronology

Texturally in-situ U–Pb dating of zircons was undertaken on eclogite sample RB11. The zircons occur as ~5-10 micron inclusions in garnet, and are mostly concentrated as small clusters in the garnet rim (Fig. 7c-e). Zircons of 5-10 micron size also occur in the matrix, typically in the regions surrounding garnet (Fig. 7d-e). Low U contents and the small size of the zircons made U–Pb dating of the eclogite challenging. Twenty-one analyses of sixty-four total were excluded due to high concentrations of [204]Pb, and ten analyses were excluded as disconcordant (>30%). Thirty-three analyses of in-situ
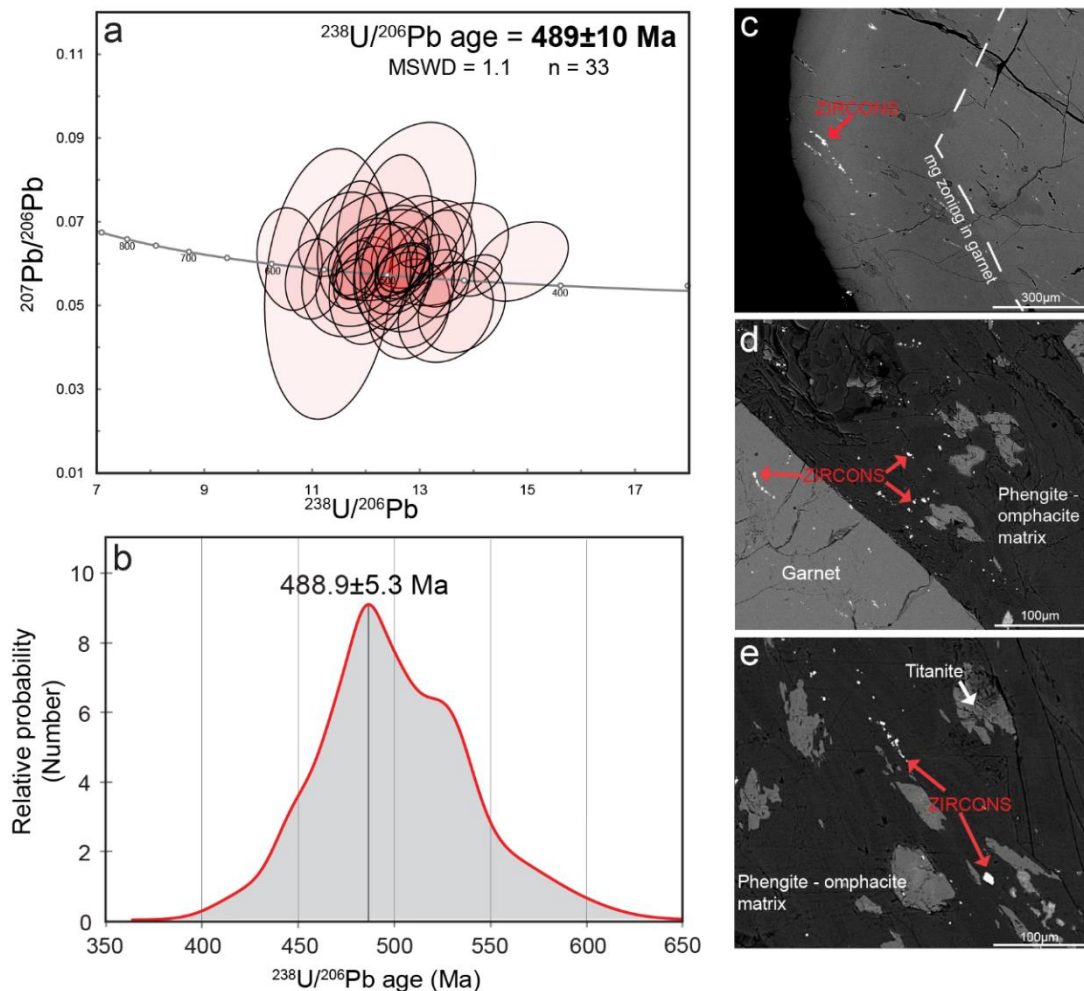
Fig. 7: A) Terra-Wasserberg Concordia of zircon data from sample RB11. B) Relative probability of analyses, showing 1 peak. C-E) BSE images of garnet and the surrounding matrix showing the textural locations of analysed zircons.

zircons in sample RB11 yielded a weighted average ^{238}U/^{206}Pb age of 489±10 Ma (Fig. 7a; data and standard information in Appendix 3). There was no statistical age difference between zircons contained as inclusions in garnet and zircon in the matrix.

Lu–Hf and Sm–Nd geochronology

Lu–Hf and Sm–Nd analyses of garnet, whole rock and lawsonite yielded various isochron ages, dependant on the isotopic system used or the mineral separates selected (Table 4; Fig. 8). The Sm–Nd garnet–whole rock isochron from eclogite sample RB11 gave an older age of 533±9.8 Ma (Fig. 8a), whereas garnet–whole rock isochrons from blueschist sample RB12 yielded an Sm–Nd age of 464.0±3.9 Ma (Fig. 8b). One garnet fraction from sample RB12 was excluded from analyses due to high (7.239 ppm) Nd concentrations resulting in low ^{147}Sm/^{144}Nd ratios, and all lawsonite fractions were excluded from Sm–Nd isochrons.

Three isochrons can be compared for eclogite sample RB11: garnet–lawsonite–whole rock, lawsonite–whole rock and garnet–whole rock, yielding ages of 487±11 Ma, 506±15 Ma and 489.7±5.5 Ma respectively (Fig. 8c,e,f). One lawsonite fraction was excluded due to a high ^{176}Lu/^{177}Hf ratio (Table 4). The Lu–Hf garnet–whole rock isochron for sample RB12 gave an age of 472.4±1.7 Ma, not within error of the Sm–Nd age (Fig. 8d). One garnet fraction was again excluded due to abnormally high Lu and Hf concentrations, which resulted in a low ^{176}Lu/^{177}Hf ratio.
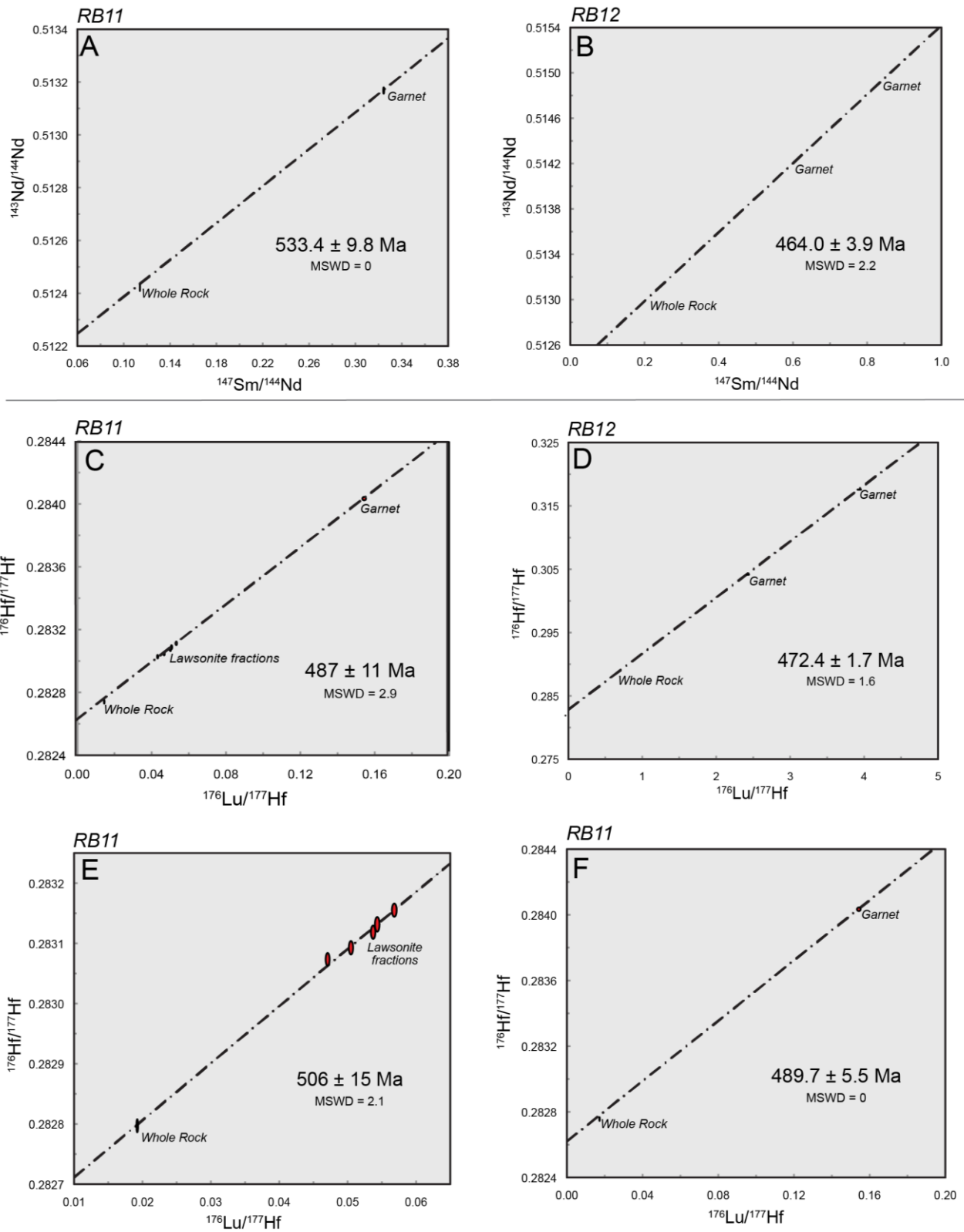
Fig. 8: Lu–Hf and Sm–Nd isochrons for samples RB11 and RB12, errors are depicted as ellipses. Isotopic systems are separated by the grey line. All lawsonite fractions were excluded from Sm–Nd isochrons as lawsonite is not a suitable mineral for Sm–Nd geochronology, due to negligible fractionation of Sm over Nd.

Table 4: Sm–Nd and Lu–Hf isotopic results from eclogite and blueschist at Port Macquarie

Sample	Fraction	Sm [ppm]	2σ	Nd [ppm]	2σ	147Sm/144Nd	2σ	143Nd/144Nd	2σ
RB11	Lawsonite 1-A	24.882	0.054	75.183	0.814	0.20008	0.00221	0.512627	0.000008
	Lawsonite 1-B	26.41	0.068	78.465	0.396	0.203488	0.001152	0.512625	0.000004
	Lawsonite 1-C	24.075	0.053	72.665	0.614	0.200301	0.001747	0.51263	0.000007
	Lawsonite 2-A	30.094	0.074	93.293	1.534	0.195019	0.003241	0.512571	0.000009
	Lawsonite 2-B	28.674	0.114	90.025	1.094	0.192564	0.002461	0.512598	0.000009
	Lawsonite 2-C	31.343	0.102	93.271	0.958	0.203162	0.002188	0.512583	0.000005
	Garnet 1	2.115	0.001	3.934	0.003	0.325075	0.000304	0.513173	0.000009
	Whole Rock	12.428	0.008	64.283	0.02	0.116875	0.000082	0.512445	0.00001
RB12	Garnet 1	2.687	0.001	7.239	0.013	0.224389	0.000417	0.512868	0.000012
	Garnet 2	2.012	0.001	1.449	0.001	0.840118	0.000448	0.514938	0.000013
	Garnet 3	2.019	0	2.013	0	0.606874	0.000191	0.514217	0.000007
	Whole Rock	0.742	0	2.034	0	0.220627	0.000011	0.513051	0.000007

Sample	Fraction	Lu [ppm]	Hf [ppm]	176Lu/177Hf	2σ	176Hf/177Hf	2σ	Weight (mg)
RB11	Garnet 1	2.827	2.583	0.155	0.0008	0.284042	0.000004	73.49
	Lawsonite 1-A	0.731	2.195	0.047	0.0002	0.283073	0.000004	71.32
	Lawsonite 2-A	0.777	1.911	0.058	0.0003	0.283139	0.000004	77.62
	Lawsonite 1-B	0.78	1.943	0.057	0.0003	0.283155	0.000004	76.66
	Lawsonite 2-B	0.707	1.841	0.054	0.0003	0.283132	0.000006	76.88
	Lawsonite 1-C	0.655	1.836	0.05	0.0003	0.283093	0.000005	76.29
	Lawsonite 2-C	0.85	2.238	0.054	0.0003	0.283119	0.000004	78.99
	Whole Rock	1.124	8.264	0.019	0.0001	0.282797	0.000004	100.09
RB12	Garnet 1	3.132	3.898	0.114	0.0006	0.283641	0.000005	69.38
	Garnet 2	1.952	0.07	3.951	0.0198	0.317732	0.000016	75.31
	Garnet 3	1.278	0.074	2.461	0.0123	0.304656	0.000023	60.43
	Whole Rock	0.256	1.896	0.019	0.0001	0.282977	0.000007	99.8

Whole rock Sm–Nd isotopes

Whole rock Sm–Nd results are shown in Table 5. Overall, the Port Macquarie samples are juvenile (isotopic values near depleted mantle), with εNd values from +6.62 to +7.03 at the ages given in Table 5. The exception is the eclogite sample RB11 which has a lower εNd value of +1.23.

Table 5: Whole rock Sm–Nd isotope results

Sample	Rock type	147Sm/144Nd	143Nd/144Nd	2σ	εNd(t)	Age (Ma)
RB05	Blueschist conglomerate	0.1501	0.512357	0.000002	7.03	490
RB06	Blueschist conglomerate	0.1530	0.512349	0.000001	6.88	490
RB07	Blueschist conglomerate	0.1412	0.512343	0.000002	6.74	490
RB11	Garnet-lawsonite eclogite	0.1168	0.512445	0.000010	1.23	489
RB12	Garnet bearing blueschist	0.2206	0.513051	0.000011	6.62	472

Phase equilibria modelling

Pressure–temperature (P–T) pseudosections were calculated in the NCKFMASHO system. Calculations in the full NCKFMASHTO system predict the stable coexistence of rutile–garnet–lawsonite–omphacite–phengite in the modelled bulk compositions, whereas the rocks contains the assemblage titanite–garnet–lawsonite–omphacite–phengite. The presence of titanite in the samples probably reflects the role of Fe^{3+} and Al within the titanite lattice (Table 3), which expands the stability of titanite up pressure (Enami *et al.,* 1993). The currently available activity–composition model for titanite does not incorporate Fe^{3+} and Al. Consequently, phase equilibria calculations do not correctly predict the stability of the Fe^{3+}-Al bearing titanite in the samples. To address

this, modelling was done in the Ti-free system NCKFMASHO. This does not affect the modelled phase relations significantly as titanite accounts for <1% of the assemblage. A calculated amount of Ca and Si was also removed along with Ti from the bulk rock geochemistry to account for the models inability to depict titanite, $CaTiSiO_5$.

For sample RB11 whole rock chemistry (modified for titanite removal) was used to calculate the pseudosection (Appendix 4), as the sample shows limited evidence for retrogression, and potential post-peak compositional change. However this is not applicable to the PB16 eclogite sample, as the relict eclogitic part of the rock is volumetrically minor and the measured bulk rock chemistry reflects that of the retrograde blueschist assemblage, which may imply open system chemical behaviour. To address this, an eclogitic bulk rock chemistry was calculated using the measured microprobe chemistry of the eclogite mineral assemblage (Appendix 2a; Fig. 4e) combined with an estimation of their modal proportions in Table 6.

Aside from limiting the model chemical system to a Ti-free environment, uncertainties in modelling the *P–T* conditions of rocks from bulk rock chemistry are the oxidation state (Fe_2O_3) and water content (H_2O). As these eclogites are interpreted to be hydrous (as suggested by the presence of lawsonite and phengite) and formed in a water-rich subduction environment (e.g. Martin *et al.,* 2014), they are modelled with water in excess, i.e. setting H_2O as a saturating phase in THERMOCALC. A value for FeO (hence O) was determined for sample RB11 by undertaking modelling prior to the *P–T* model, where mineral assemblage stability is determined as a function of oxidation state at fixed temperature. The peak assemblage was located at 5.5% Fe_2O_3 and 94.5% FeO.

Oxidation state for sample PB16 was directly constrained from the microprobe chemical analyses used to calculate the bulk eclogitic chemistry, by assuming perfect mineral stoichiometry in the calculation of cations from raw wt% data (Droop, 1987; Appendix 2a).

RB11

Port Macquarie eclogite RB11 contains an interpreted peak assemblage of phengite + garnet + omphacite + lawsonite + quartz (+ titanite). This assemblage is modelled to occur at ~27 kbar and ~570 °C (Fig. 9), the peak field is bound by the higher pressure appearance of coesite and lower pressure appearance of talc, and by the loss of quartz at lower temperatures and the modal proportion contour of 5% for lawsonite at a higher temperature (Fig. 10, Table 6). The retrograde evolution is defined by the appearance of glaucophane and chlorite, which formed at the expense of omphacite and garnet, respectively. Although the formation of these retrograde minerals reduces the modal proportions of the peak minerals, the retrograde minerals frequently pseudomorph the peak phases, meaning the peak assemblage modes are still evident.

The grey arrow depicts the inferred retrograde trajectory, characterized by the appearance of chlorite and glaucophane and reduced omphacite, lawsonite and phengite modes (Fig. 9). The *P-T* path passes through talc stability, but as talc is not recorded in the mineralogy, the retrograde path probably passed through the low modal proportions part of this field (Fig. 10h).
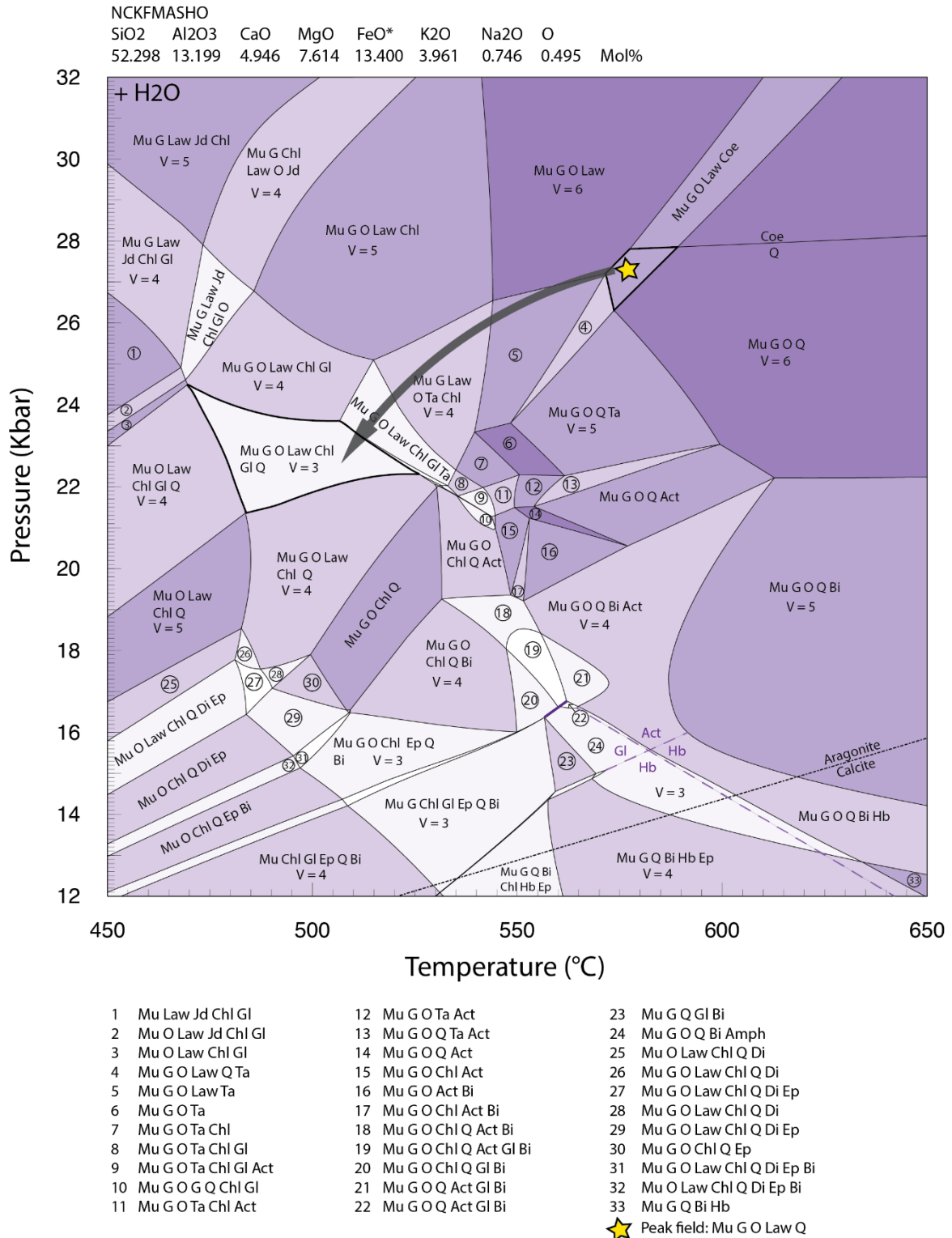
Fig. 9: *P-T* **pseudosection for eclogite RB11. Bold black lines indicate peak fields, and the grey arrow represents the retrograde path. Bold purple line indicates a univariant reaction. Purple dashed lines indicate the trace of a solvus, the stable mineral on each side of the solvus is labelled in purple. Composition used for calculation of the pseudosection is provided in mol% above the diagram. FeO* = FeO + 2 x 'O'. V is Variance, which is equal to components – phases +2, and increases with increased shading in the diagram. Abbreviations: Mu: Muscovite (Phengite); Law: Lawsonite; G: Garnet; O: Omphacite; Q: Quartz; Coe: Coesite; Chl: Chlorite; Jd: Jadeite; Ta: Talc; Gl: Glaucophane; Act: Actinolite; Hb: Hornblende; Bi: Biotite; Di: Diopside; Ep: Epidote: Amph: Amphibole, chemistry dependant on solvi present.**
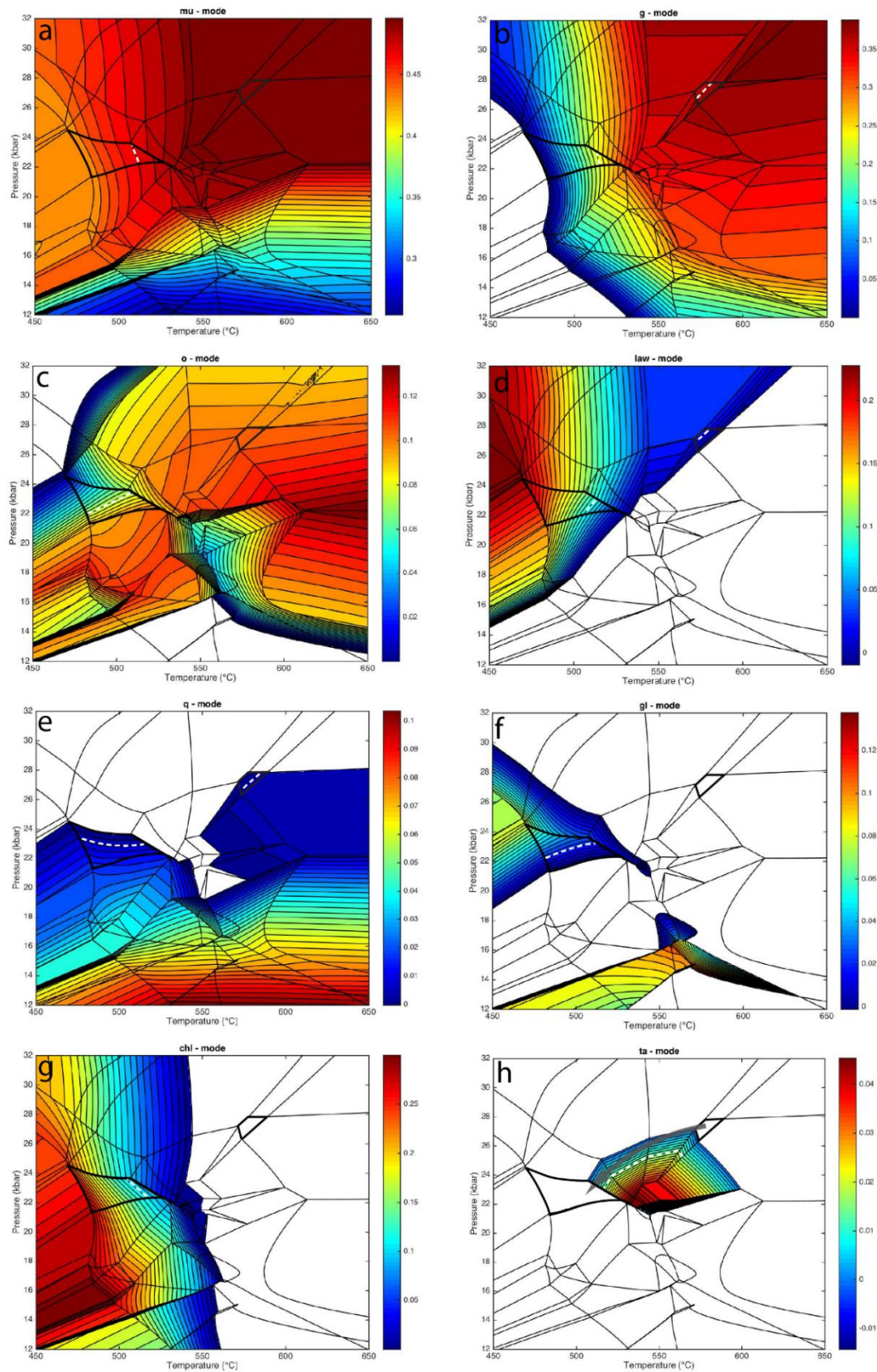
Fig. 10: TCI outputs for RB11 *P-T*, modal proportions are of a) muscovite (phengite), b) garnet, c) omphacite, d) lawsonite, e) quartz, f) glaucophane, g) chlorite and h) talc. While dotted lines indicate contour that correspond to estimated modal abundance of that mineral from thin section, heavy black lines indicate peak field.

PB16

The peak assemblage is defined by garnet–omphacite–lawsonite–phengite, however the proportions of the peak minerals have been modified by retrograde glaucophane–chlorite–epidote ± quartz. Nevertheless, partial psuedomorphic replacement of garnet by chlorite, and omphacite by glaucophane (Fig. 4e), and replacement of lawsonite by feldspars, mica and epidote (Fig. 5d), allows reasonable estimation of the proportion of the peak minerals to be made. Based on these estimated modes in the relict eclogite (Table 6), Pigna Barney eclogite PB16 experienced peak conditions of ~24 kbar and ~560-585 °C (Fig. 11), bound by the appearance of quartz at higher temperatures, biotite at lower temperatures, a modal proportion contour of garnet at higher pressure, and omphacite down pressure (Fig. 12). However, the temperature is poorly constrained. The retrograde path (grey arrow; Fig. 12) is defined by the appearance of glaucophane–chlorite–epidote in the relict eclogite, defining a decreasing pressure *P–T* evolution. Due to currently (Oct 10th 2016) unresolved difficulties calculating the region of *P-T* space at ~14–17 kbar, 550–560 °C, which involves two overlapping amphibole solvi, this portion of the diagram is metastable with respect to the diagram. TCI is unable to fully contour a diagram that contains both stable and metastable assemblages, consequently modal proportion contours for minerals glaucophane, epidote and chlorite were unable to be calculated for the PB16 model.
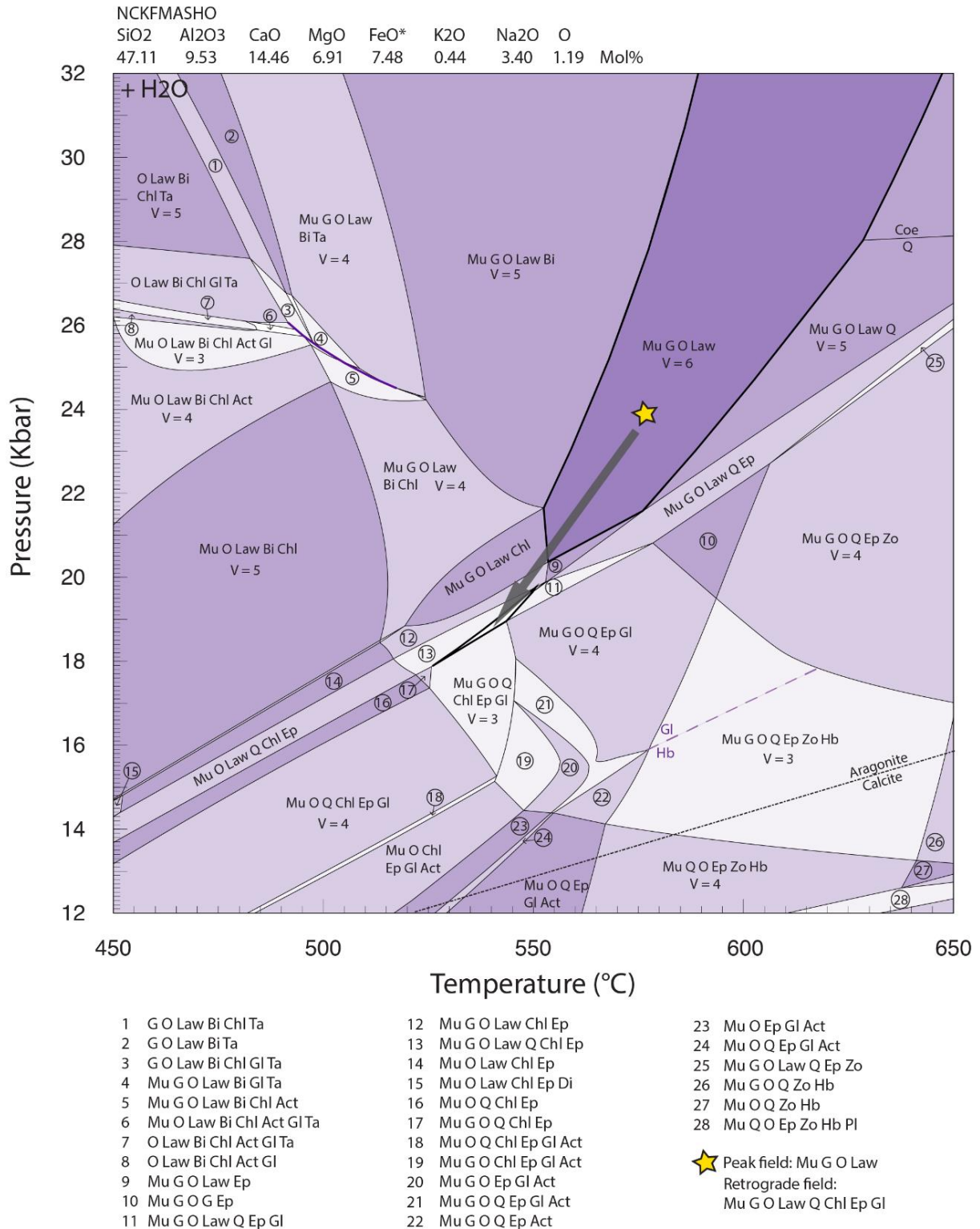
Fig. 11: *P-T* pseudosection for eclogite PB16. Bold black lines indicate peak fields, and the grey arrow represents the retrograde path. Bold purple line indicates a univariant reaction. Purple dashed lines indicate the trace of a solvus, the stable mineral on each side of the solvus is labelled in purple. Composition used for calculation of the pseudosection is provided in mol% above the diagram. FeO* = FeO + 2 x 'O'. V is Variance, which is equal to components – phases + 2, and increases with increased shading in the diagram. Abbreviations: Mu: Muscovite (Phengite); Law: Lawsonite; G: Garnet; O: Omphacite; Q: Quartz; Coe: Coesite; Chl: Chlorite; Jd: Jadeite; Ta: Talc; Gl: Glaucophane; Act: Actinolite; Hb: Hornblende; Bi: Biotite; Di: Diopside; Ep: Epidote: Zo; Zoisite; Pl: Plagiocalse; Amph: Amphibole, chemistry dependant on solvi present.
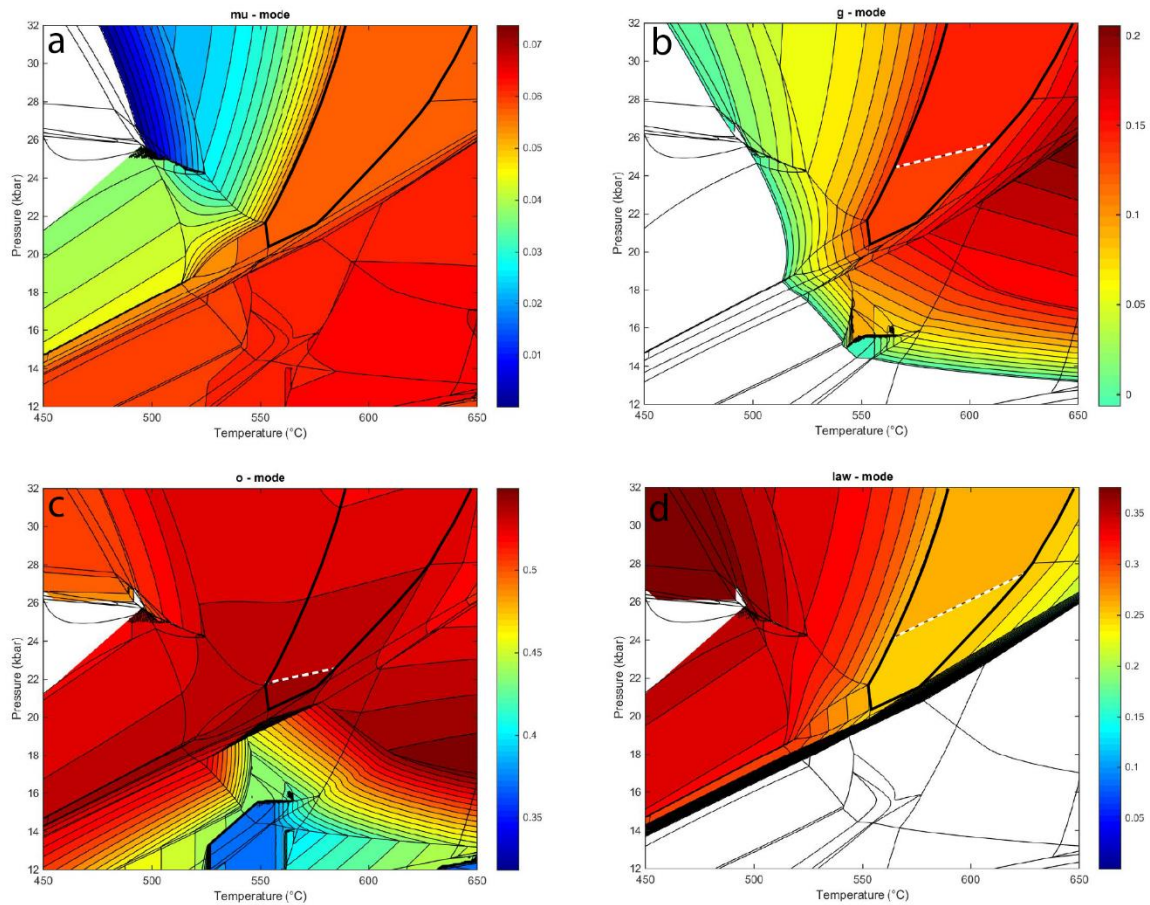
Fig. 12: TCI outputs for PB16 *P-T*, showing modal proportions of a) muscovite (phengite), b) garnet, c) omphacite and d) lawsonite. White dotted line indicates contour that corresponds to estimated modal proportion of that mineral from thin section, heavy black line indicates peak fields. Retrograde minerals are not shown due to difficulties encountered with multiple solvi and an unstable area of the pseudosection, see main text for detail.

Table 6: Estimated modal proportions of minerals in eclogite samples RB11 and PB16 from thin section. Retrograde mineral modal proportions for PB16 are representative of retrogression in the region of relict eclogite, and do not reflect that of the blueschist assemblage. Titanite is presented however was not calculated in the pseudosections, hence is not presented in the TCI outputs.

	RB11		PB16	
	Peak	Retrograde	Peak	Retrograde
Garnet	35%	22%	14%	13%
Lawsonite	5%	6%	25%	5%
Omphacite	10%	8%	54%	46%
Phengite	50%	44%	5%	6%
Quartz	<1%	<1%	<1%	<1%
Glaucophane		4%		20%
Chlorite		14%		7%
Epidote				2%
Titanite	<1%	<1%	<1%	<1%

DISCUSSION

Timing of high pressure metamorphism in the SNEFB

The U–Pb zircon age of 489±10 Ma for RB11 (Fig. 7) is interpreted to date the age of peak eclogite metamorphism, as the analysed zircons are located predominately in the rims of prograde zoned garnets and in the immediately surrounding matrix (Fig. 6c-e). The zircons are commonly euhedral, occur in trails or clusters, and are in close spatial association with metamorphic titanite (Fig. 6c-e), eliminating the possibility that they could be relict zircons from the mafic igneous protolith. The exact reaction that formed zircon in unclear. Rubatto *et al.* (2008) documented identical zircon textures to those seen in RB11 in eclogite-facies rocks, attributing it to complete dissolution-precipitation of magmatic zircon by locally derived fluids during metamorphism.

Garnets from eclogite sample RB11 have Lu enrichment in their cores whereas Sm is unzoned (Fig. 6), however the Sm–Nd age of 533.4±9.8 Ma is much older than the ca. 490 Ma Lu–Hf ages (Fig. 8). The presence of Nd-rich inclusions potentially effects the Sm–Nd age (Scherer *et al.,* 2000; Anczkiewicz *et al.*, 2004). Although great effort was taken to obtain pure mineral seperates, fine-grained inclusions such as titanite contain high concentrations of non-radiogenic Nd as evident in LA-ICP-MS maps (Fig. 6a), and are difficult to remove completely during mineral separation. Their effect on isochron ages is potentially twofold: i) if the inclusion assemblage is old, then the derived age may reflect the age of the inclusions rather than the host garnet, or; ii) the initial isotopic ratio of the inclusions may not be in equilibrium with the initial isotopic ratio of the

whole rock, meaning the t=0 isochron would have a non-zero slope, and the recorded age would be older or younger than the true age (e.g. Mawby *et al.,* 1999; Scherer *et al.,* 2000). Fig. 5 shows Sm and Nd traverses across a representative garnet in RB11. The presence of Nd- and Sm-rich inclusions is evident as pronounced concentration spikes. However, the garnet host has approximately flat Nd and Sm profiles, averaged across the profile at ~4 ppm Nd and ~2 ppm Sm. These values are similar to the concentrations determined by TIMS (Table 4), suggesting the garnet mineral separate was largely free of Sm–Nd rich inclusions, meaning the Sm–Nd age should be reliable.

An assumption in isochron geochronology is that all minerals were initially in isotopic equilibrium at t=0, however this may not always be the case. Therefore, the significantly older Sm–Nd age for RB11 could be attributed to slightly different initial ratios between garnet and whole rock, potentially as a consequence of alteration of Sm–Nd in the whole rock post-peak (e.g. Blichert-Toft and Frei, 2001; Thöni, 2002). This could have occurred via the infiltration of isotopically evolved fluids infiltrating the eclogite matrix after garnet growth, and altering the effective bulk rock Sm–Nd ratio, creating isotopic disequilibrium between garnet and matrix minerals (e.g. Blichert-Toft and Frei, 2001). The effect of this is demonstrated in Fig. 13, where the whole rock point has a lower $^{143}Nd/^{144}Nd$ ratio after infiltration of evolved fluid, resulting in a positive slope early-age isochron, which produces ages that are too old.

In contrast to the Sm–Nd system, the Lu–Hf system is less mobile and less susceptable to disturbance (Becker *et al.*, 2000; John *et al.*, 2008; Martin *et al.*, 2009). Using the

Lu–Hf system, whole rock and 4 lawsonite fractions give an age of 506±15 Ma and the

garnet–whole rock gives 489.7±5.5 Ma (Fig. 8).
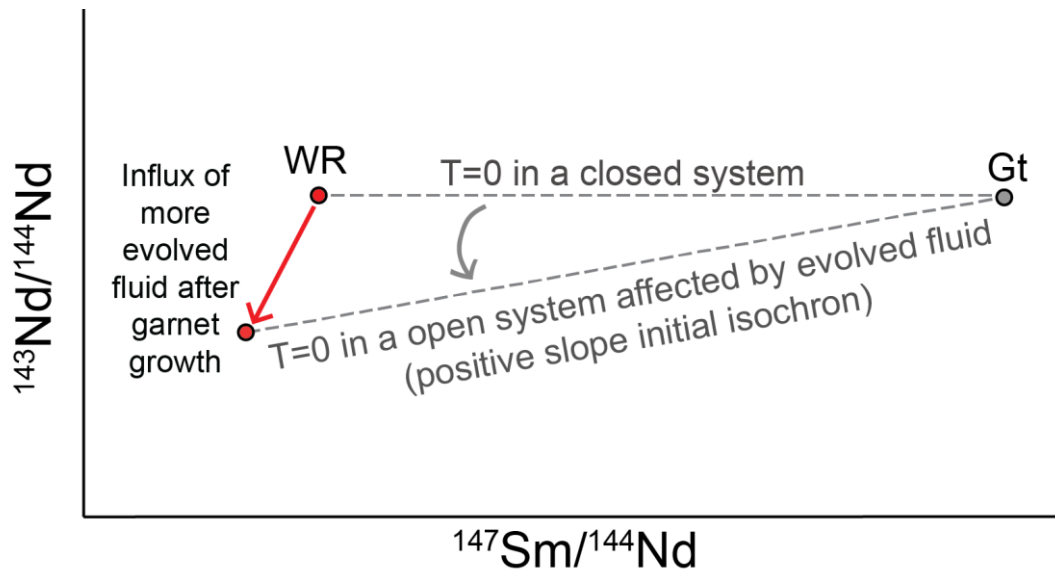
Fig. 13: Schematic diagram illustrating the effect of open-system whole rock interaction with an evolved fluid on isochron ages. Red arrow indicates the movement of the whole rock (WR) point, whereas the grey arrow indicates the movement (rotation) of the t = 0 isochron. The garnet (Gt) point remains fixed at T=0 as it is out of chemical (isotopic) communication with the bulk rock, hence is not affected by the fluid influx. This is the mechanism that is interpreted to affect sample RB11, giving it an Sm-Nd age that is "too old". The Lu-Hf system is less susceptible to this effect, as Lu and Hf are considerably less mobile in fluid than Sm and Nd.

Although these are within error of each other, lawsonite texturally predates garnet in the

metamorphic history of the eclogite. This is evidenced by lawsonite inclusions in

garnet, but not vice versa, and the stability of lawsonite before garnet in the *P–T*

pseudosection (Fig. 9). The larger error on the lawsonite-whole rock isochron is due to

low $^{176}Lu/^{177}Hf$ ratios of the lawsonite fractions (Table 4). The garnet–lawsonite–whole

rock isochron gives an age of 487±11 Ma (Fig. 8c). However, this is controlled by the

garnet–whole rock points, and hence is a similar age to the garnet–whole rock isochron

(489.7±5.5 Ma). The garnet–whole rock Lu–Hf age is interpreted to record garnet

growth, based on the preservation of prograde-zoned Lu in garnet from RB11 (Fig. 6a).

This age is within error of the zircon U–Pb age.

Garnet-bearing blueschist from Port Macqaurie gives an Sm–Nd age of 464±3.9 Ma (Fig. 8b) and a Lu–Hf age of 472.4±1.7 (Fig. 8d) from garnet-whole rock isochrons. The two ages are not in error of each other. The Lu–Hf closure temperature is thought to be higher than that of the Sm–Nd system (Sm–Nd: ~700°C, Lu–Hf: ~750°C; e.g. Scherer *et al.,* 2000; Ganguly *et al.,* 1988). However, blueschist facies metamorphism at Port Macquarie occurred at temperatures below closure temperatures for both these systems (Och *et al.,* 2003). Hence the difference in ages cannot be attributed to differences in closure systematics. Alternatively, it could reflect a non-zero t=0 slope Sm–Nd isochron. The difference in ages may otherwise reflect internal zonation patterns of isotopes targeted, revealed by laser mapping of garnet from this sample (Fig. 6b). RB12 garnets show strong enrichment of Lu (100 ppm) in the core of the garnet, consistent with Rayleigh fractionation during growth (Otamendi *et al.,* 2004). However there is no disernable internal zonation of Sm. This prograde Lu zoning in RB12 suggests that the Lu–Hf and Sm–Nd ages approximate average growth age, as the Lu–Hf date is slightly biased towards the early stages of garnet growth (e.g. Lapen *et al.,* 2003; Skora *et al.,* 2006).

The agreement between the zircon U–Pb age and Lu–Hf ages from the garnet–lawsonite–whole rock isochron from RB11 suggest that ca. 489 Ma is most likely the age of peak eclogite metamorphism of the lawsonite–garnet bearing eclogite at Port Macquarie. Prograde metamorphism potentially started as early as ca. 506 Ma, although the large error on the lawsonite–whole rock age precludes a definitive prograde age. Lu–Hf and Sm–Nd ages from garnet–bearing blueschist RB12 indicate that prograde

metamorphism occurred from ca. 474–464 Ma. This implies that the ca. 251 Ma

maximum age for eclogite metamorphism at Port Macqaurie suggested by Nutman *et al.*

(2013) is incorrect. It was argued by Nutman *et al*. (2013) that the abraded nature of the

zircons analysed points to a detrital origin. However, the similarity between the ages

obtained by Nutman *et al.* (2013), and the ages obtained from zircons from modern

beach sand at Port Macquarie and beaches further north (J. Payne pers comm, March

2016; Appendix 6; Sircombe, 1999) indicates the sample analysed by Nutman *et al*.

(2013) was contaminated with modern beach sand.

Pressure-temperature conditions during metamorphism

The *P-T* conditions calculated from mineral equilibria forward modelling indicate that

very cool thermal gradients were experienced by eclogite samples from Port Macquarie

and Pigna Barney, consistent with subduction-zone conditions. Eclogite RB11

experienced peak conditions of ~27 kbar and 570 °C; a thermal gradient of ~210 °C/

GPa. The retrograde evolution passed through ~22 kbar and 500 °C, indicative of a cold

high-pressure retrograde path, which is supported by the existence of aragonite in late-

stage veins (Fig. 4c; e.g. Proyer *et al.*, 2013). As such, this retrograde path is not

interpreted as exhumation dominated, but instead reflects deep residence in the

subduction channel. The almost pristine preservation of lawsonite further supports this,

as lawsonite is readily replaced during isothermal decompresson (Martin *et al.,* 2014;

Wei and Clarke, 2011; Mulcahy *et al.,* 2009). Thus, the rock had to remain in the

lawsonite stability field on the retrograde path (Fig. 9).

Eclogite at Pigna Barney experienced peak $P–T$ conditions of ~24 kbar, between 560–585 °C, corresponding to a thermal gradient of 230 °C/GPa, similar to that at Port Macquarie. The retrograde evolution could not be directly constrained on the pseudosection (Fig. 11), as the modelled bulk composition specifically targeted the relict peak eclogite assemblage. To determine the retrograde P–T evolution, it would be necessary to model the bulk composition of the blueschist domain of the rock; however because of time considerations, it has not been possible to undertake this during the project. Nonetheless, the appearance of retrograde minerals present at Pigna Barney in the pseudosection (Fig. 11; namely glaucophane, epidote and chlorite within the domain of relict eclogite) allow an interpretation of the general direction the retrograde path may have taken (grey arrow, Fig. 11). This path shows a decrease in pressure along with temperature which characterizes the transition from eclogite facies to blueschist-facies. Phillips *et al.* (2015) calculated $P–T$ conditions for blueschist facies metamorphism at Pigna Barney using conventional thermobarometry, and estimated and 7.5 kbar and 300-350 °C, in line with the estimated trajectory of the retrograde path.

Duration of physical conditions

The age constraints obtained in this study are in general agreement with previous ca. 470 Ma K–Ar ages from the melange at Port Macquarie, which is interpreted to date exhumation and cooling through the closure temperature of these systems (~350 °C; Hyodo, 2008; Offler, 1999; Fukui *et al.,* 1995). However, the K–Ar ages potentially contain undetected excess argon, producing an older than true age. More recently,

unpublished Ar–Ar data from step-heating of phengite from eclogite at Port Macquarie

gives ages of 458.4±3.7 Ma and 462.6±3.6 Ma (G Phillips pers. comm., May 2016; Fig.

14). These ages from Port Macquarie also align with K–Ar and Ar–Ar ages of ca. 470–

482 Ma from Pigna Barney and Glenrock (Fig. 2; Fukui *et al.,* 1995; Sano *et al.,* 2004;

Phillips *et al.,* 2015). This collection of geochronology in combination with the

estimates of the ages of peak metamorphism at Port Macquarie now allows the

interpretation that high-P metamorphism may have been continuous in the subduction

channel for upwards of 40 Ma. This is further supported by the mineral equilibria

modelling, both eclogite samples demonstrate refrigerated retrograde paths. The

coupled geochronological and metamorphic data from Port Macquaire points to a

dynamic system that most likely involved ongoing burial and exhumation. Peak eclogite

metamorphism occured at ca. 490 Ma, requiring burial to depths of >100 km. However,

prograde garnet Lu–Hf and Sm–Nd ages from blueschist record ages from 464–472 Ma.

This indicates that the melange at Port Macquarie continued to accumulate ongoing

subduction products for at least 20 Ma after peak eclogite metamorphism. Furthermore,
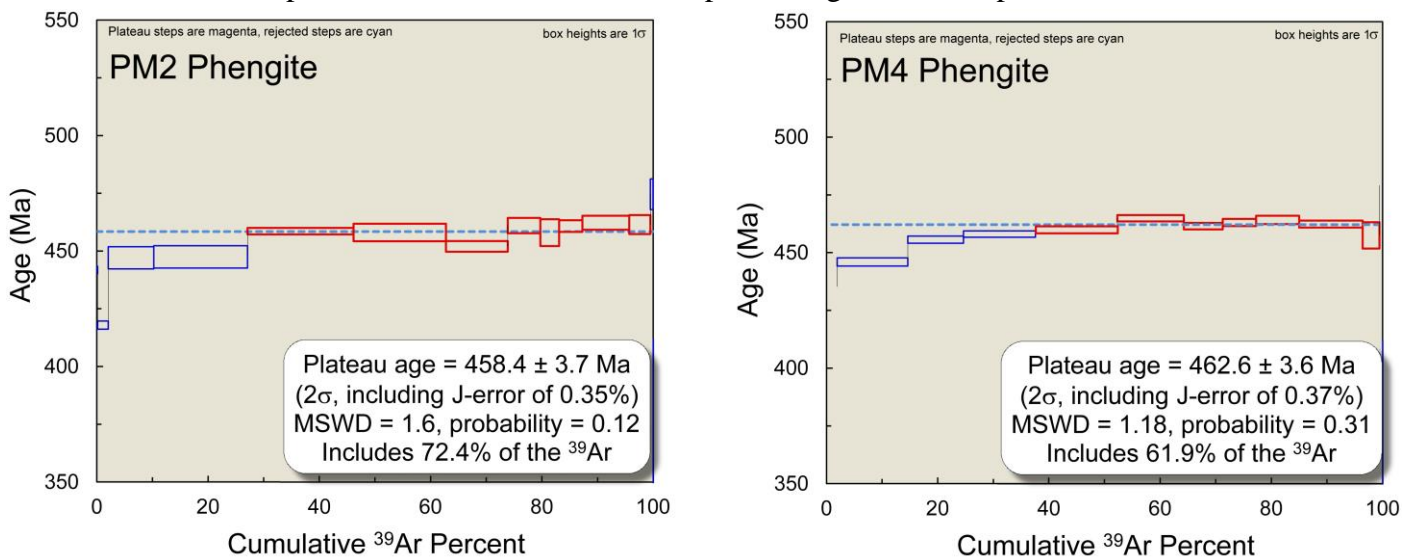
Fig. 14: Ar–Ar plateau ages on late-stage mica from eclogite at Port Macquarie, dating partial exhumation within the subduction channel and associated cooling. Data collected and provided by G. Phillips (pers comm, May 2016).

the Ar–Ar ages of ca. 460 Ma (Fig. 14) indicate that cooling below 300 °C took another 10 Ma. Plausibly, cooling was associated with exhumation within the subduction channel. This is supported by the initial retrograde path of the eclogite remaining at high pressure, the subduction and accumulation of high-P rocks over time, and the presence of retrograde aragonite, which requires very low-T/high-P conditions consistent with a subduction setting.

Long-lived eclogite–blueschist metamorphism has been studied by Agard *et al.* (2009), who demonstrated that late-stage exhumation type subduction zones (akin to this study) can record subduction for up to 70 Ma (e.g. Cuba, New Caledonia, Western Alps). The ability to retain high-P rocks in subduction zones for such time frames has been numerically modelled by Gerya et al. (2002), who showed that deeply-subducted particles can be retained in the subduction channel for more than 25 Ma (Fig. 15). This model has been successfully applied to high-P melange in the Dominican Republic, where subduction was active for almost 70 Ma (Krebs *et al.,* 2008), resulting in the formation of high-P exotic blocks in serpentinite melange, similar to that at Port Macquarie, where high-P rocks with differing *P–T–t* histories are intermingled and exhumed together. In the models, transport of particles to ~20 kbar depths occurs within the first ~7 Ma (Fig 15a), where they may reside for significant timeframes (~10–15 Ma) and experience cooling as the subduction zone matures, similar to the *P–T* path calculated for eclogite RB11a (Fig. 9; Fig. 11). These models predict that partial exhumation in the channel occurs in a late "mature" stage of subduction, where intense hydration of the mantle wedge triggers return flow from greater depths (Gerya *et al.,* 2002; Krebs *et al.,* 2008; Fig. 15c-d).
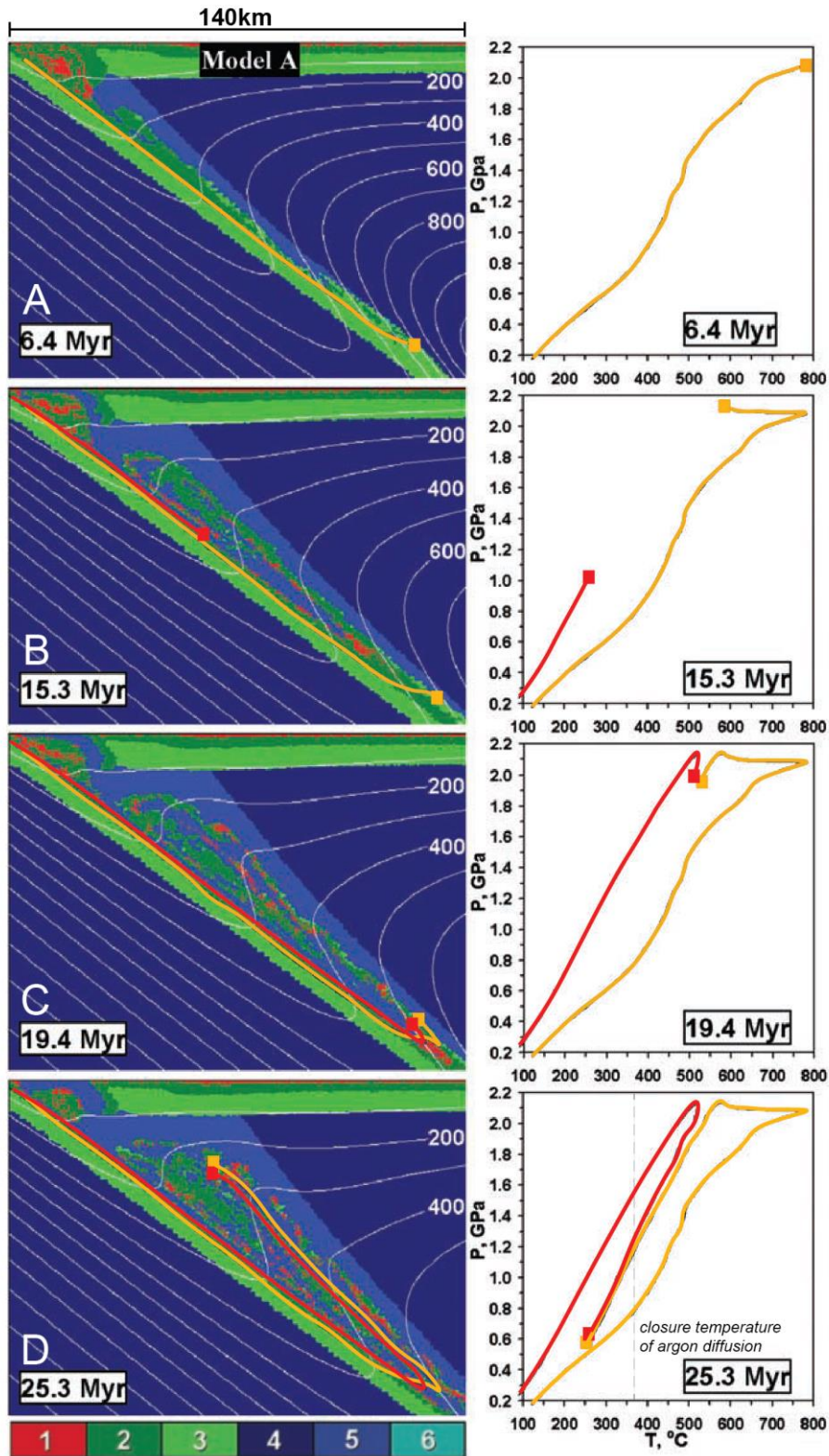
Fig. 15: Numerical model of subduction-channel dynamics, modified from Gerya et al. (2002). The left column shows the numerical model, as a wedge-shaped pattern of material is circulated during ongoing subduction, and in the right panel the movement of subducted particles in P-T space. White lines indicate isotherms, and the colour code corresponds to: 1: Sedimentary rocks; 2: Basaltic upper oceanic crust; 3: Gabbroic lower oceanic crust; 4: Unhydrated mantle; 5: Serpentinized mantle; 6: hydrated mantle beyond the stability field of antigorite.

47

This provides a means for 24–27 kbar eclogites of this study to be returned to shallower depths in the subduction channel while new material is being introduced, leading to the accumlation of high-P rocks with differing metamorphic histories. This provides an explanation for the age difference of eclogite and prograde blueschist at Port Macquarie. Baitsch-Ghirardello *et al.* (2014) demonstrated through numerical modeling that during slab-rollback, the active arc region remains coupled with the lower plate. This means that rocks trapped in the subduction channel, or underplated to the forearc, can migrate along with the retreating subduction zone during slab rollback. This provides a geodynamic mechanism for translocation of high-P rocks to a retreated position (Baitsch-Ghirardello *et al.,* 2014).

εNd and protoliths to the high-P rocks

Nd isotopic results indicate juvenile to very juvenile protoliths for the high-P rocks at Port Macquarie (Fig. 16). Eclogite sample RB11 has a comparatively evolved signature, suggesting that it may have had some crustal input, potentially ocean-floor sediments that were incorporated into the downgoing slab (cf. Yogodzinski *et al.,* 2010). This is supported by major element geochemistry, which shows that RB11 has the greatest departure from MORB-like chemistry of the samples from Port Macquarie (Appendix 5). Blueschist sample RB12 is more juvenile than RB11, indicating less sedimentary input, and more closely resembles MORB-type crust (Fig. 16, Appendix 5; Phillips and Offler, 2010).

Samples RB05, RB06 and RB07 are deformed conglomerates from Port Macquarie, metamorphosed to blueschist facies. They are interpreted to be metavolcanic/igneous rocks, as the clasts comprise relict phenocrystic rocks (now replaced by lawsonite, amphiboles and chlorite) consistent with mafic to intermediate volcanic protoliths (see Petrography; Fig. 4c). In support of this, their geochemistry suggests that they have calc-alkaline affinity (Appendix 5), which indicates that they may be derived from an arc-related source. These samples are also the most juvenile, and plot very close to depleted mantle (Fig. 16), suggesting that they most likely formed in an oceanic arc setting. Phillips *et al.* (2015) reported rocks of similar chemistry at Glenrock, north in the PMFS (Fig. 2).

Fig. 16 compiles Port Macquarie samples plotted against εNd values of igneous rocks from the Koonenberry Belt (Greenfield *et al.,* 2012), early Macquarie Arc (Crawford *et al.,* 2007), and the Lachlan and Delamerian orogens (Fig. 1 and 2; Kemp *et al.,* 2009). An assumption is made in this diagram that blueschist-facies metamorphism of samples RB05-07 occurred alongside other high-P metamorphism at Port Macquarie (ca. 490–470 Ma) prior to slab rollback and relocation to their current position in the SNEFB. These are isotopically similar to those of the Koonenberry Belt and the earliest mafic rocks of the Macquarie Arc (Crawford *et al.,* 2007, Glen *et al.,* 2011). However, only very few rocks of the Macquarie Arc were formed in this timeframe (Crawford *et al.*, 2007), whereas the Koonenberry Belt was potentially a source prior to and during high-P metamorphism sampled at Port Macqaurie.
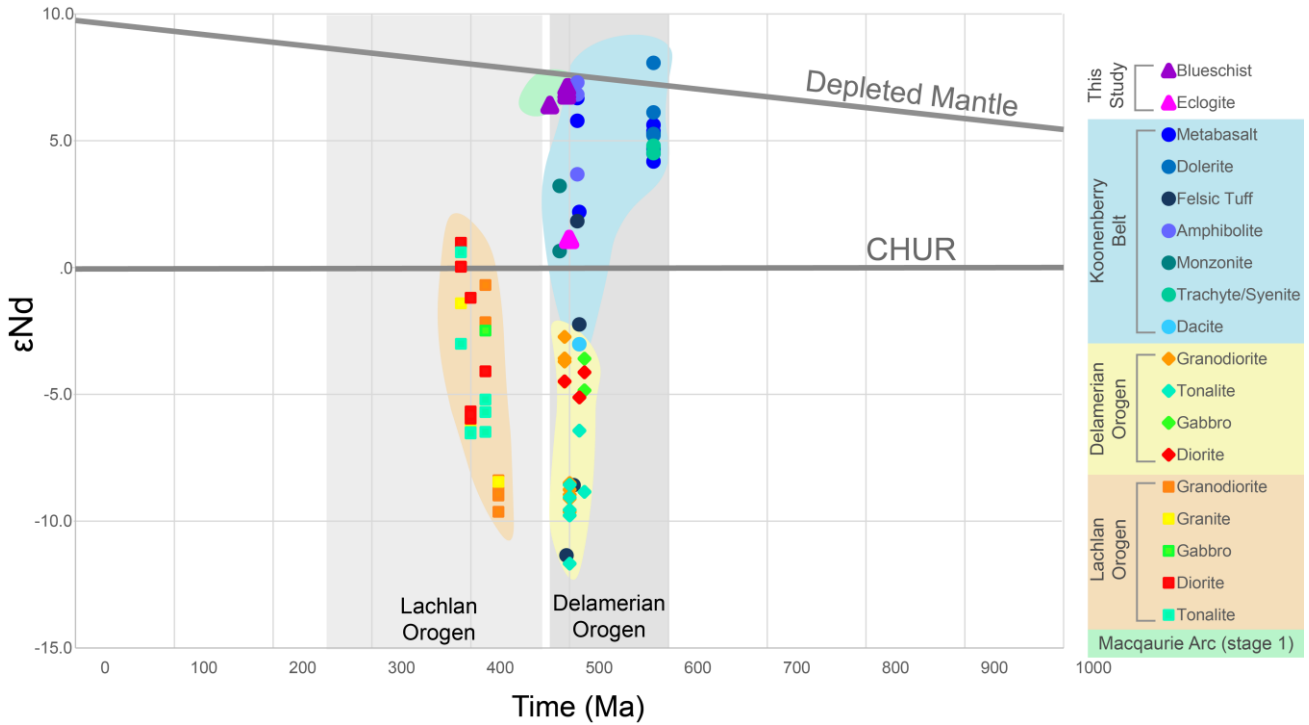
Fig. 16: εNd values for the Port Macquarie samples compiled with magmatic data from the Koonenberry Belt (Greenfield _et al.,_ 2011), the earliest stage of Macquarie Arc magmatism (stage 1; Crawford _et al.,_ 2007) and magmatism from the Delamerian and Lachlan orogens (Kemp _et al.,_ 2009, and references within). Magmatism mixing with cratonised continent (i.e. the Delamerian) or sediments in a backarc basin (i.e. the Lachlan) tend to be more evolved, as they contain a crustal component. Magmatism associated with arc activity in an oceanic or suprasubduction setting is more juvenile (i.e. the Koonenberry and Macquarie arc). It can be seen that early mafic rocks of the Macquarie Arc formed slightly later than high-P metamorphism at Port Macquarie, whilst the Koonenberry magmatism was ongoing prior to and during high-P metamorphism. εNd trends are also summarized in Fig. 19.

Tectonic implications and development of the southern Tasminides

The models for the formation of the southern Tasminides range from complex, involving multiple subduction zones, collisions, and subduction flips (Aitchison and Buckman, 2012; Glen, 2013) to one simple, west-dipping subduction zone that rolled back throughout the Paleozoic, transferring one orogenic stage to the next (Collins, 2002; Phillips and Offler, 2011; Phillips _et al.,_ 2015). The tectonic mechanics of these models primarily determine how significant crustal growth was achieved on the

Gondwanan eastern margin in this time, but also provide differing scenarios for the existence of Cambro–Ordovician eclogite and blueschist in the SNEFB.

When subduction is punctuated, models suggest that crust is formed through the collision and forward accretion of arcs, forearc prisms and exotic terranes (Aitchison and Buckman, 2012; Glen, 2013). This implies that the Tasminade high-P rocks formed in a subduction system outboard of the early Tasman orogenic system, that was later accreted as part of an exotic island arc during the Hunter–Bowen Orogeny (250–270 Ma), or even later (Collins, 2007; Nutman *et al.,* 2013; Buckman *et al.,* 2015).

In a single, long-lived, west-dipping subduction scenario, coupled with oceanward rollback (e.g. Baitsch-Ghirardello *et al.,* 2014), new continental crust is built in an extensive upper-plate back arc basin system predominantly via sedimentation, and thickened in sporadic episodes of short-lived contraction (Collins, 2002; Kemp *et al.,* 2009). In this model, transference to the next younger stage of upper-plate basin development is caused by slab rollback. Interspersed compressional events occur when the trench transiently advances, or asperities such as seamount chains are subducted (Collins, 2002). The geodynamic evolution of this model from the Delamerian to Lachlan orogenic stages is presented in Fig. 17. Firstly, it explains how long-lived subduction, hence refrigerated metamorphism, occurred for upwards of 40 Ma, as recorded at Port Macquarie. Secondly, it provides a mechanism for translocation of high-P rocks now located in the PMFS from their initial development on the margin of cratonic Australia during the Delamerian Orogeny, to their current position in the SNEFB, ~2000 km eastwards. Lastly, it provides a possible protolith source — the

Koonenberry Belt — for the blueschist facies meta-volcanics at Port Macquarie. The migration of early-formed eclogites and the incorporation of younger blueschist is termed here forearc entrapment.

Timing of eclogite metamorphism in the SNEFB coincides with the duration of the Delamerian Orogeny from 514–490 Ma (Fig. 17a and 18; Phillips and Offler, 2010; Phillips et al., 2015; this work). Calc-alkaline magmatism in the Koonenberry Belt was active from ca. 517 Ma (Fig. 17a; Kemp et al., 2009; Greenfield et al., 2012; Johnson et al., 2016), while erosion and subduction of this arc detritus now present Port Macquarie took place. The protolith of the now dismembered Peel-Manning serpentinite belt formed in a supra subduction setting, while the Koonenberry Belt evolved to a back-arc setting (Fig. 17a; Phillips et al., 2015; Johnson et al., 2016). During continual rollback, extensive upper plate sedimentation began to accumulate the protoliths to the Lachlan Orogen, as well as the inception of the Macquarie Arc (Fig. 17b-c; Crawford et al., 2007; Glen et al., 2011). This period of rollback was synchronous with blueschist-facies metamorphism in the subduction channel, recording both: i) metamorphism of new MORB-material being subducted ca. 472 Ma (Port Macquarie blueschist) and ii) retrogression of eclogite as hydration of the mantle wedge facilitated return flow of eclogite to blueschist-facies conditions (Port Macquarie and Pigna Barney blueschist; Fig. 17b; Gerya et al., 2002). Rollback of the slab continued, remaining in an oceanic setting (Fig. 17d), throughout development of the Lachlan to the New England orogens, where the high-P rocks were exhumed from shallower levels in the channel within the hydrated basal harzburgite of the Peel-Manning ophiolite to their current location in the west-dipping PMFS (Fig. 17e-f; Phillips et al., 2015).
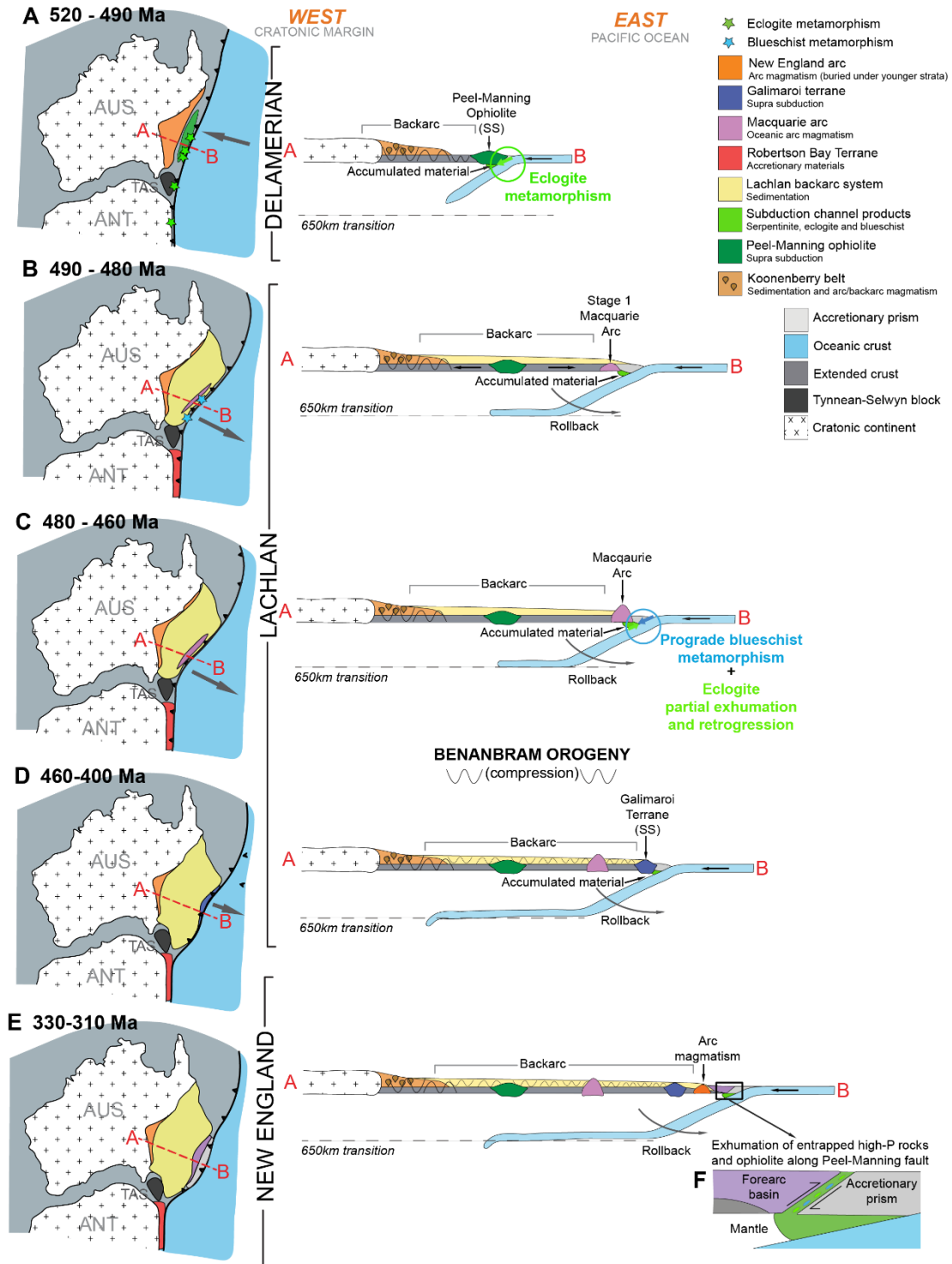
Fig. 17: Suggested illustration of the geodynamics of the southern Tasminides. A) Supra subduction (SS) creates the Peel-Manning ophiolite, which is underplated. Subduction during the Delamerian facilitates eclogite-facies metamorphism on the eastern Australian margin, whilst the Koonenberry is in a backarc setting. B) Blueschist metamorphism occurs as rollback of the slab transfers the high-P rocks outboard in eastern Australia, but not in Tasmania or Antarctica. Deposition of the large Lachlan backarc basin is active as well as early (stage 1) Macquarie Arc magmatism. C) Macquarie Arc magmatism continues, as does backarc extension and sedimentation. The contractional Benambran Orogeny shortens this basin. D) The Galimaroi Terrane is formed in a supra subduction setting, backarc sedimentation continues. E) Rollback continues, transferring the high-P rocks further east to the New England orogen. Arc magmatism is active however it is currently buried by younger sedimentation. F) The entrapped high-P rocks and Peel-Manning ophiolite/serpentinite are exhumed through the west-dipping Peel-Manning fault system.

The geology of the southern Tasminides supports this model, in that there are eastwards-younging arcs left relict as the subduction zone rolled back eastwards (Crawford *et al.,* 2007; Kemp *et al.,* 2009; Glen *et al.,* 2011; Greenfield *et al.,* 2012), the development of multiple upper-plate extensional basins (Collins, 2002; Glen, 2005; Fergusson, 2010; Johnson *et al.,* 2016), and rift-related back-arc magmatism in the Lachlan Orogen (Collins, 2002; Squire *et al.,* 2006; Dadd, 2011). Importantly, the trends in Nd and Hf isotopes in magmatic rocks become progressively more juvenile as the subduction zone migrates eastwards away from the evolved cratonic margin (Kemp
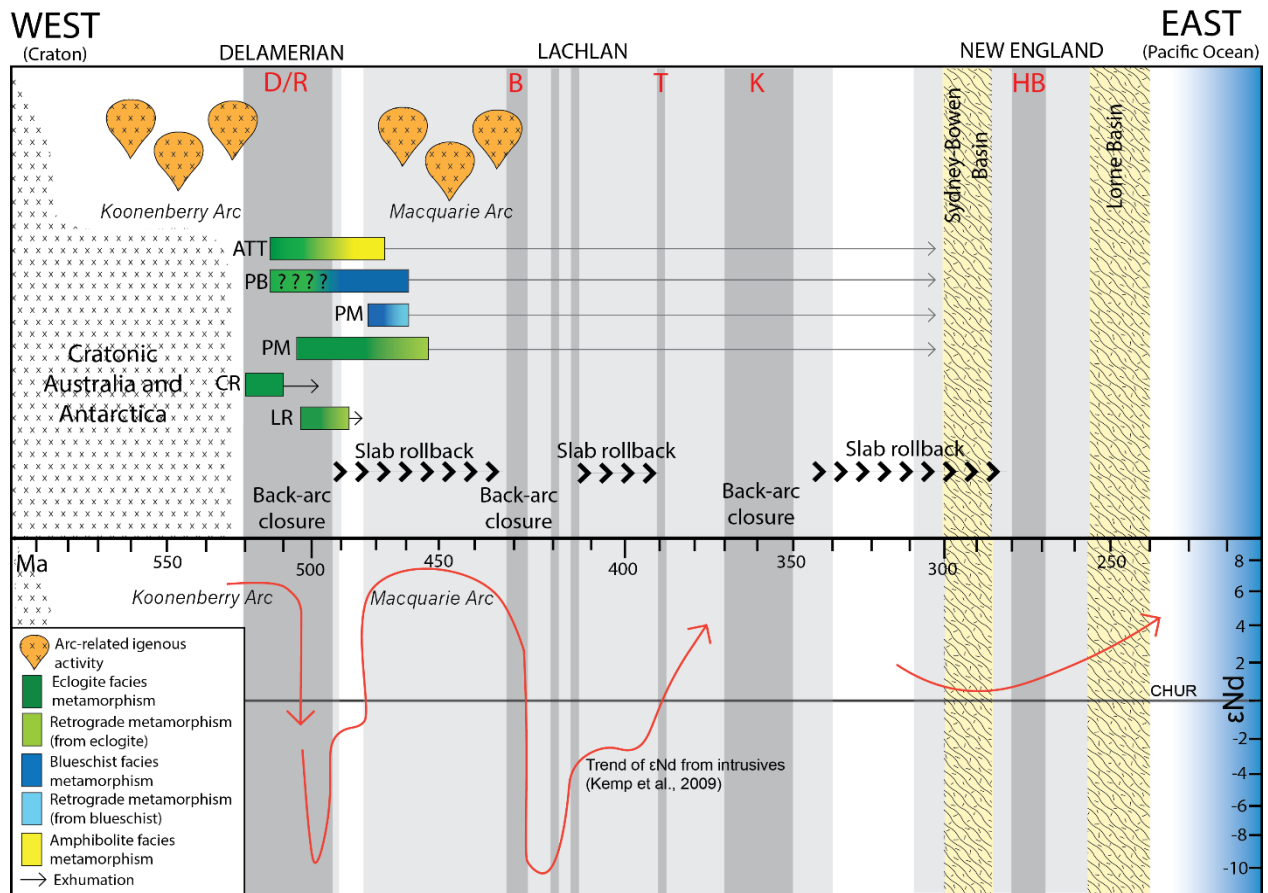
Fig. 18: Simplified time-space plot of the evolution of the Southern Tasminides, taken from cross-section A-B in Fig. 17. Darker grey bands indicate compressional events, lighter grey bands indicate orogenic stages, and pale yellow indicates sedimentary basins of importance. The state of subduction is indicated, whether the slab is in a period of rollback and hence upper-plate extension, or back-arc closure and hence compression. Duration of eclogite, blueschist and amphibolite facies metamorphism from eastern Australia, Tasmania and Antarctica are indicated as colour (green, blue, yellow) shaded bars. The trend of εNd from magmatic rocks is indicated in red, sourced from Crawford *et al.* (2011), Kemp *et al.* (2009) and references therein, and Greenfield *et al.* (2011). D/R Delamerian/Ross Orogeny, B: Benambran Orogeny, T: Tabbarabberan Orogeny, K: Kanimblan Orogeny, HB: Hunter-Bowen Orogeny. ATT: Attunga, PB: Pigna Barney, PM: Port Macquarie, CR: Collingwood River (Franklin Metamorphic Complx, Tasmania), LR: Lanterman Range (North Victoria Land, Antarctica).

et al., 2009). This is illustrated in Fig. 18, which shows the general isotopic trend of εNd values against geodynamic events of the southern Tasminides.

Episodic rollback and back-arc closure spanned a ca. 300 Ma history, reflected in evolved εNd values of magmas that interacted with sedimentary rocks of the back-arc system during contraction, and juvenile signatures reflecting oceanic-arc magmatism during rollback (Kemp *et al.,* 2009).

Differing styles of high-pressure metamorphism on the eastern Gondwanan margin

As previously indicated, eclogite metamorphism took place on the southern segment of the eastern Gondwanan margin, in the Franklin Metamorphic Complex in Tasmania, from ca. 510-505 Ma, and Lantermann Range in Antarctica ca. 500 Ma (Fig. 18; Di Vincenzo *et al.,* 1997; Berry *et al.,* 2007), simultaneous with eclogite metamorpism in the SNEFB. In Tasmania, the high-P rocks are unconformably overlain by Early Ordovician sedimentary rocks ca. 498 Ma in age (Berry *et al.,* 2007). Ar–Ar geochronology from Antarctica indicates that eclogite had largely exhumed by ca. 498–490 Ma (Di Vincenzo and Palmeri, 2001). These rapidly buried and exhumed high-P rocks contrast with the similar aged, but slowly exhumed, eclogites in the SNEFB. The high-P rocks in Tasmania and Antarctica are encased in bouyant continental rocks (Berry *et al.,* 2007; Palmeri *et al.,* 2009), which presumably facilited their rapid exhumation during slab breakoff faciliated by the difficulty of subucting bouyant crust. Subduction dynamics were further complicated in Tasmania and Antarctica, with the arrival of continental ribbons and the possibility of east-dipping and west-dipping subduction on the margin (Palmeri *et al.,* 2009; Mulder *et al.,* 2015). These contrasting

records of burial and exhumation of eclogites on the east Gondwanan margin likely reflects the tectonic nature of the hosts of the eclogite protolith. Forearc entrapment and long-distance translocation of high-P rocks in the SNEFB was governed by a long-term oceanic setting, whereas further south on the margin accretion and unsucessful subduction of continental ribbons facilitated rapid exhumation of eclogitic rocks.

CONCLUSION

Serpentinite-hosted eclogite and blueschist facies metamorphism at Port Macquarie in the SNEFB occurred at ca. 490 Ma and ca. 470 Ma respectively, followed by cooling associated with their exhumation within the subduction channel at ca. 460 Ma. The *P–T* evolution of the Port Macquarie eclogite suggests exhumation from ~27 kbar within the subduction channel along an extremely refrigerated retrograde path that remained at high pressures. The *P–T–t* evolution of newly discovered eclogite at Pigna Barney demonstrates that partial exhumation of eclogite from ~24 kbar returned it to blueschist facies conditions within the channel before ca. 480 Ma. This points to a dynamic setting of ongoing subduction that accumulated rocks in cold, high-pressure conditions within the subduction channel for at least 30 Ma. Additionally, blueschist-facies conglomerates from Port Macquarie have Nd isotopic values which suggests their derivation from oceanic-arc material nearby the cratonic margin (the Koonenberry Belt). The high-P rocks span a temporal and spatial history, beginning at eclogite facies metamorphism on the Australian cratonic margin during the Delamerian Orogeny. The long-lived accumulation of subduction products is consistent with subduction rollback during the

interval 490–460 Ma, leading to the development of the protoliths to the Lachlan

Orogen in a large backarc system on the extended upper plate. Rollback ultimately

transferred the high-P rocks ~2000 km east, prior to their eventual exhumation during

the development of the New England Orogen. This model of continuous rollback of a

west-dipping subduction zone provides a simple geodynamic scenario for continental

crustal growth in the Tasminides, through upper-plate sedimentation and magmatism

cratonised through punctuated compression. It also reveals the ability of subduction

channels to continuously accumulate and cycle high-P rocks at eclogite and blueschist

facies conditions for significant periods of time, with the potential to relocate them

thousands of kilometers through rollback.

ACKNOWLEDGEMENTS

REFERENCES

AGARD, P., YAMATO, P., JOLIVET, L., & BUROV, E. (2009). Exhumation of oceanic blueschists and eclogites in subduction zones: Timing and mechanisms. *Earth-Science Reviews, 92*(1-2), 53-79. doi:10.1016/j.earscirev.2008.11.002

AITCHISON, J., & BUCKMAN, S. (2012). Accordian vs. quantum tectonics: Insights into continental growth processes from the Paleozoic of eastern Gondwana. *Gondwana Research, 22*, 674-680. doi:10.1016/j.gr.2012.05.013

AITCHISON, J. C., & IRELAND, T. R. (1995). Age profile of ophiolitic rocks across the Late Palaeozoic New England Orogen, New South Wales: Implications for tectonic models. *Australian Journal of Earth Sciences, 42*(1), 11-23. doi:10.1080/08120099508728175

ALLAN, A. D., & LEITCH, E. C. (1992). The nature and origin of eclogite blocks in serpentinite from the Tamworth Belt, New England Fold Belt, eastern Australia. *Australian Journal of Earth Sciences, 39*(1), 29-35. doi:10.1080/08120099208727998

ANCZKIEWICZ, R., PLATT, J. P., THIRLWALL, M. F., & WAKABAYASHI, J. (2004). Franciscan subduction off to a slow start: evidence from high-precision Lu–Hf garnet ages on high grade-blocks. *Earth and Planetary Science Letters, 225*(1-2), 147-161. doi:10.1016/j.epsl.2004.06.003

ANCZKIEWICZ, R., & THIRLWALL, M. F. (2003). Improving precision of Sm-Nd garnet dating by H_2SO_4 leaching: A simple solution to the phosphate inclusion problem. *Geological Society Special Publication*(220), 83-91.

BAITSCH-GHIRARDELLO, B., GERYA, T. V., & BURG, J.-P. (2014). Geodynamic regimes of intra-oceanic subduction: Implications for arc extension vs. shortening processes. *Gondwana Research, 25*(2), 546-560. doi:10.1016/j.gr.2012.11.003

BECKER, H., JOCHUM, K. P., & CARLSON, R. W. (2000). Trace element fractionation during dehydration of eclogites from high-pressure terranes and the implications for element fluxes in subduction zones. *Chemical Geology, 163*(1-4), 65-99. doi:10.1016/s0009-2541(99)00071-6

BERRY, R. F., CHMIELOWSKI, R. M., STEELE, D. A., & MEFFRE, S. (2007). Chemical U – Th – Pb monazite dating of the Cambrian Tyennan Orogeny, Tasmania. *Australian Journal of Earth Sciences, 54*(5), 757-771. doi:10.1080/08120090701305269

BLICHERT-TOFT, J., & FREI, R. (2001). Complex Sm-Nd and Lu-Hf isotope systematics in metamorphic garnets from the Isua supercrustal belt, West Greenland. *Geochemica et Cosmochimica Acta, 65*(18), 3177-3187.

BUCKMAN, S., NUTMAN, A. P., AITCHISON, J. C., PARKER, J., BEMBRICK, S., LINE, T., KAMIICHI, T. (2015). The Watonga Formation and Tacking Point Gabbro, Port Macquarie, Australia: Insights into crustal growth mechanisms on the eastern margin of Gondwana. *Gondwana Research, 28*(1), 133-151. doi:10.1016/j.gr.2014.02.013

CAWOOD, P. A., LEITCH, E. C., MERLE, R. E., & NEMCHIN, A. A. (2011). Orogenesis without collision: Stabilizing the Terra Australis accretionary orogen, eastern Australia. *Geological Society of America Bulletin, 123*(11-12), 2240-2255. doi:10.1130/b30415.1

COLLINS, W. J. (2002). Nature of extensional accretionary orogens. *Tectonics, 21*(4), 6-1-6-12. doi:10.1029/2000tc001272

COLLINS, W. J. (2007). A reassessment of the 'Hunter-Bowen Orogeny': Tectonic implications for the southern New England fold belt. *Australian Journal of Earth Sciences, 38*(4), 409-423. doi:10.1080/08120099108727981

CONNOLLY, J. A. D. (2002). An automated strategy for calculation of phase diagram sections and retrieval of rock properties as a function of physical conditions. *Journal of Metamorphic Geology, 20*, 697-708.

CONNOLLY, J. A. D. (2005). Computation of phase equilibria by linear programming: A tool for geodynamic modeling and its application to subduction zone decarbonation. *Earth and Planetary Science Letters, 236*(1-2), 524-541. doi:10.1016/j.epsl.2005.04.033

CRAWFORD, A. J., MEFFRE, S., SQUIRE, R. J., BARRON, L. M., & FALLOON, T. J. (2007). Middle and Late Ordovician magmatic evolution of the Macquarie Arc, Lachlan Orogen, New South Wales. *Australian Journal of Earth Sciences, 54*(2-3), 181-214. doi:10.1080/08120090701227471

CROSS, K. (1983). *The Pigna Barney ophiolitic complex and associated basaltic rocks, northeastern New South Wales, Australia.* (Doctor of Philosophy), University of New England, Armidale, NSW.

DADD, K. A. (2011). Extension-related volcanism in the Middle to Late Devonian of the Lachlan Orogen: geochemistry of mafic rocks in the Comerong Volcanics. *Australian Journal of Earth Sciences, 58*(2), 209-222. doi:10.1080/08120099.2011.535563

DE CAPITANI, C., & BROWN, T. H. (1987). The computation of chemical equilibrium in complex systems containing non-deal solutions. *Geochemica et Cosmochimica Acta, 51*, 2639-2652.

DI VINCENZO, G., GRANDE, A., & ROSSETTI, F. (2014). Paleozoic siliciclastic rocks from northern Victoria Land (Antarctica): Provenance, timing of deformation, and implications for the Antarctica-Australia connection. *GSA Bulletin, 126*(11/12), 1416-1438. doi:10.1130/B31034.1

DI VINCENZO, G., & PALMERI, R. (2001). An Ar-Ar investigation of high-pressure metamorphism and the retrogressive history of mafic eclogites from the Lanterman Range (Antarctica): evidence against a single temperature control of argon transport in amphibole. *Contributions to Mineralogy and Petrology, 141*, 15-35. doi:10.1007/s004100000226

DI VINCENZO, G., PALMERI, R., TALARICO, F., ANDRIESSEN, P., & RICCI, C. A. (1997). Petrology and Geochronology of Eclogites from the Lanterman Range, Antarctica. *Journal of Petrology, 38*(10), 1391-1417.

DIENER, J. F. A., & POWELL, R. (2012). Revised activity-composition models for clinopyroxene and amphibole. *Journal of Metamorphic Geology, 30*(2), 131-142. doi:10.1111/j.1525-1314.2011.00959.x

DROOP, G. (1987). A general equation for estimating Fe^{3+} concentrations in ferromagnesian silicates and oxides from microprobe analyses, using stoichiometric criteria. *The Mineralogical Society, 51*, 431-435.

ENAMI, M., SUZUKI, K., LIOU, J., & BIRD, D. (1993). Al-Fe^{3+} and F-OH substitutions in titanite and contraints on their P-T dependance. *European Journal of Mineralogy, 5*, 219-231.

FERGUSSON, C. L. (2010). Plate-driven extension and convergence along the East Gondwana active margin: Late Silurian–Middle Devonian tectonics of the Lachlan Fold Belt, southeastern Australia. *Australian Journal of Earth Sciences, 57*(5), 627-649. doi:10.1080/08120099.2010.494767

FODEN, J., ELBURG, M., DOUGHERTYPAGE, J., & BURTT, A. (2006). The Timing and Duration of the Delamerian Orogeny: Correlation with the Ross Orogen and Implications for Gondwana Assembly. *The Journal of Geology, 114*(2), 189-210. doi:10.1086/499570

FUKUI, S., WATANABE, T., ITAYA, T., & LEITCH, E. C. (1995). Middle Ordovician high PT metamorphic rocks in eastern Australia: evidence from K-Ar ages. *Tectonics, 14*(4), 1014-1020.

G, C. R., & E, L. D. (1962). Metamorphic aragonite in the glaucophane schists of Cazadero, California. *American Journal of Science, 260*, 577-595.

GANGULY, J., TIRONE, M., & HERVIG, R. (1998). Diffusion Kinetics of Samarium and Neodymium in Garnet, and a Method for Determining Cooling Rates of Rocks. *Science, 281*, 805-807.

GERYA, T. V., STÖCKHERT, B., & PERCHUK, A. L. (2002). Exhumation of high-pressure metamorphic rocks in a subduction channel: A numerical simulation. *Tectonics, 21*(6), 6-1-6-19. doi:10.1029/2002tc001406

GLEN, R. A. (2005). The Tasmanides of eastern Australia. *Geological Society Special Publication, 246*, 23-96. doi:10.1144/GSL.SP.2005.246.01.02

GLEN, R. A. (2013). Refining accretionary orogen models for the Tasmanides of eastern Australia. *An International Geoscience Journal of the Geological Society of Australia, 60*(3), 315-370. doi:10.1080/08120099.2013.772537

GLEN, R. A., SAEED, A., QUINN, C. D., & GRIFFIN, W. L. (2011). U–Pb and Hf isotope data from zircons in the Macquarie Arc, Lachlan Orogen: Implications for arc evolution and Ordovician palaeogeography along part of the east Gondwana margin. *Gondwana Research, 19*(3), 670-685. doi:10.1016/j.gr.2010.11.011

GREEN, E., HOLLAND, T., & POWELL, R. (2007). An order-disorder model for omphacitic pyroxenes in the system jadeite-diopside-hedenbergite-acmite, with applications to eclogitic rocks. *American Mineralogist, 92*(7), 1181-1189. doi:10.2138/am.2007.2401

GREENFIELD, J. E., MUSGRAVE, R. J., BRUCE, M. C., GILMORE, P. J., & MILLS, K. J. (2011). The Mount Wright Arc: A Cambrian subduction system developed on the continental margin of East Gondwana, Koonenberry Belt, eastern Australia. *Gondwana Research, 19*(3), 650-669. doi:10.1016/j.gr.2010.11.017

HOLLAND, T., BAKER, J., & POWELL, R. (1998). Mixing properties and activity-composition relationships of chlorites in the system MgO-FeO-Al_2O_3-SiO_2-H_2O. *European Journal of Mineralogy, 10*, 395-406.

HOLLAND, T., & POWELL, R. (2003). Activity-composition relations for phases in petrological calculations: an asymmetric multicomponent formulation. *Contributions to Mineralogy and Petrology, 145*, 492-501.

HOLLAND, T. J. B., & POWELL, R. (2011). An improved and extended internally consistent thermodynamic dataset for phases of petrological interest, involving a new equation of state for solids. *Journal of Metamorphic Geology, 29*(3), 333-383. doi:10.1111/j.1525-1314.2010.00923.x

HOWARD, K. E., HAND, M., BAROVICH, K. M., PAYNE, J. L., CUTTS, K. A., & BELOUSOVA, E. A. (2011). U–Pb zircon, zircon Hf and whole-rock Sm–Nd isotopic constraints on the evolution of Paleoproterozoic rocks in the northern Gawler Craton. *Australian Journal of Earth Sciences, 58*(6), 615-638. doi:10.1080/08120099.2011.594905

HYODO, H. (2008). Laser probe 40Ar/39Ar dating: History and development from a technical perspective. *Gondwana Research, 14*(4), 609-616. doi:10.1016/j.gr.2008.01.008

JENKINS, R., LANDENBERGER, B., & COLLINS, W. J. (2002). Late Palaeozoic retreating and advancing subduction boundary in the New England Fold Belt. *Australian Journal of Earth Sciences, 49*, 467-489.

JOHN, T., KLEMD, R., GAO, J., & GARBE-SCHÖNBERG, C.-D. (2008). Trace-element mobilization in slabs due to non steady-state fluid–rock interaction: Constraints from an eclogite-facies transport vein in blueschist (Tianshan, China). *LITHOS, 103*(1-2), 1-24. doi:10.1016/j.lithos.2007.09.005

JOHNSON, E. L., PHILLIPS, G., & ALLEN, C. M. (2016). Ediacaran–Cambrian basin evolution in the Koonenberry Belt (eastern Australia): Implications for the geodynamics of the Delamerian Orogen. *Gondwana Research, 37*, 266-284. doi:10.1016/j.gr.2016.04.010

KEMP, A. I. S., HAWKESWORTH, C. J., COLLINS, W. J., GRAY, C. M., & BLEVIN, P. L. (2009). Isotopic evidence for rapid continental growth in an extensional accretionary orogen: The Tasmanides, eastern Australia. *Earth and Planetary Science Letters, 284*(3-4), 455-466. doi:10.1016/j.epsl.2009.05.011

KREBS, M., MARESCH, W. V., SCHERTL, H. P., MÜNKER, C., BAUMANN, A., DRAPER, G., . . . TRAPP, E. (2008). The dynamics of intra-oceanic subduction zones: A direct comparison between fossil petrological evidence (Rio San Juan Complex, Dominican Republic) and numerical simulation. *LITHOS, 103*(1-2), 106-137. doi:10.1016/j.lithos.2007.09.003

LANARI, P., VIDAL, O., DE ANDRADE, V., DUBACQ, B., LEWIN, E., GROSCH, E. G., & SCHWARTZ, S. (2014). XMapTools: A MATLAB©-based program for electron microprobe X-ray image processing and geothermobarometry. *Computers & Geosciences, 62*, 227-240. doi:10.1016/j.cageo.2013.08.010

LAPEN, T. J., JOHNSON, C. M., BAUMGARTNER, L. P., MAHLEN, N. J., BEARD, B. L., & AMATO, J. M. (2003). Burial rates during prograde metamorphism of an ultra-high-pressure terrane: an example from Lago di Cignana, western Alps, Italy. *Earth and Planetary Science Letters, 215*(1-2), 57-72. doi:10.1016/s0012-821x(03)00455-2

LEITCH, E. C. (1974). The geological development of the southern part of the New England Fold Belt. *Journal of the Geological Society of Australia, 21*(2), 133-156. doi:10.1080/00167617408728840

LEITCH, E. C. (1994). Paleozoic ophiolitic assemblages within the southern New England orogen of eastern Australia: Implications for growth of the Gondwana margin. *Tectonics, 13*(5), 1135-1149. doi:10.1029/93TC03550

LI, P. F., ROSENBAUM, G., & RUBATTO, D. (2012). Triassic asymmetric subduction rollback in the southern New England Orogen (eastern Australia): the end of the Hunter-Bowen Orogeny. *Australian Journal of Earth Sciences, 59*(6), 965-981. doi:10.1080/08120099.2012.696556

LI, P. F., ROSENBAUM, G., YANG, J.-H., & HOY, D. (2015). Australian-derived detrital zircons in the Permian-Triassic Gympie terrane (Eastern Australia): Evidence for an autochthonous orogin. *Tectonics, 34*, 858-874. doi:10.1002/2015TC003829

MARTIN, C., DUCHÊNE, S., LUAIS, B., GONCALVES, P., DELOULE, E., & FOURNIER, C. (2009). Behavior of trace elements in relation to Lu–Hf and Sm–Nd geochronometers during metamorphic dehydration–hydration in the HP domain of Vårdalsneset, Western Gneiss Region, Norway. *Contributions to Mineralogy and Petrology, 159*(4), 437-458. doi:10.1007/s00410-009-0434-1

MARTIN, L. A. J., HERMANN, J., GAUTHIEZ-PUTALLAZ, L., WHITNEY, D. L., VITALE BROVARONE, A., FORNASH, K. F., & EVANS, N. J. (2014). Lawsonite geochronology and stability - implication for trace element and water cycles in subduciton zones. *Journal of Metamorphic Geology, 32*, 455-478. doi:10.1111/jmg.12093

MAWBY, J., HAND, M., & FODEN, J. (1999). Sm-Nd evidence for high-grade Ordovician metamorphism in the Arunta Block, central Australia. *Journal of Metamorphic Geology, 17*, 653-668.

MORRISSEY, L., PAYNE, J. L., KELSEY, D. E., & HAND, M. (2011). Grenvillian-aged reworking in the North Australian Craton, central Australia: Constraints from geochronology and modelled phase equilibria. *Precambrian Research, 191*(3-4), 141-165. doi:10.1016/j.precamres.2011.09.010

MULCAHY, S. R., VERVOORT, J. D., & RENNE, P. R. (2014). Dating subduction-zone metamorphism with combined garnet and lawsonite Lu-Hf geochronology. *Journal of Metamorphic Geology, 32*, 515-533. doi:10.1111/jmg.12092

MULDER, J. A., BERRY, R. F., MEFFRE, S., & HALPIN, J. A. (2016). The metamorphic sole of the western Tasmanian ophiolite: new insights into the Cambrian tectonic setting of the Gondwana pacific margin. *Gondwana Research, 38*, 351-369. doi:10.1016/j.gr.2015.12.010

NUTMAN, A. P., BUCKMAN, S., HIDAKA, H., KAMIICHI, T., BELOUSOVA, E., & AITCHISON, J. (2013). Middle Carboniferous-Early Triassic eclogite–blueschist blocks within a serpentinite mélange at Port Macquarie, eastern Australia: Implications for the evolution of Gondwana's eastern margin. *Gondwana Research, 24*(3-4), 1038-1050. doi:10.1016/j.gr.2013.01.009

OCH, D. J., LEITCH, E. C., CAPRARELLI, G., & WATANABE, T. (2003). Blueschist and eclogite in tectonic melange, Port Macquarie, New South Wales, Australia. *Mineralogical Magazine, 67*(4), 609-624. doi:10.1180/0026461036740121

OFFLER, R. (1999). *Origin and significance of blueschist "knockers", Glenrock Station, NSW*. Paper presented at the New England Orogen, Armidale.

OTAMENDI, J., DE LA ROSA, J., PATINO DOUCE, A., & CASTRO, A. (2002). Rayleigh fractionation of heavy rare earths and yttrium during metamorphic garnet growth. *Geological Society of America Bulletin, 30*(2), 159-162.

PALMERI, R., CHMIELOWSKI, R., SANDRONI, S., TALARICO, F., & RICCI, C. A. (2009). Petrology of the eclogites from western Tasmania: Insights into the Cambro-Ordovician evolution of the paleo-Pacific margin of Gondwana. *LITHOS, 109*(3-4), 223-239. doi:10.1016/j.lithos.2008.06.016

PALMERI, R., TALARICO, F. M., & RICCI, C. A. (2011). Ultrahigh-pressure metamorphism at the Lanterman Range (northern Victoria Land, Antarctica). *Geological Journal, 46*(2-3), 126-136. doi:10.1002/gj.1243

PAYNE, J. L., HAND, M., BAROVICH, K. M., & WADE, B. P. (2008). Temporal constraints on the timing of high-grade metamorphism in the northern Gawler Craton: implications for assembly of the Australian Proterozoic. *Australian Journal of Earth Sciences, 55*(5), 623-640. doi:10.1080/08120090801982595

PEARCE, M. A., WHITE, A. J. R., & GAZLEY, M. F. (2015). TCInvestigator: automated calculation of mineral mode and composition contours forthermocalcpseudosections. *Journal of Metamorphic Geology, 33*(4), 413-425. doi:10.1111/jmg.12126

PHILLIPS, G., HAND, M., & OFFLER, R. (2008). P-T-t deformation framework of an accretionary prism, southern New England Orogen, eastern Australia: Implications for blueschist exhumation and metamorphic switching. *Tectonics, 27*(6), n/a-n/a. doi:10.1029/2008tc002323

PHILLIPS, G., HAND, M., & OFFLER, R. (2010). P-T-X controls on phase stability and composition in LTMP metabasite rocks - a thermodynamic evaluation. *Journal of Metamorphic Geology, 28*(5), 459-476. doi:10.1111/j.1525-1314.2010.00874.x

PHILLIPS, G., & OFFLER, R. (2011). Contrasting modes of eclogite and blueschist exhumation in a retreating subduction system: The Tasmanides, Australia. *Gondwana Research, 19*(3), 800-811. doi:10.1016/j.gr.2010.07.009

PHILLIPS, G., OFFLER, R., RUBATTO, D., & PHILLIPS, D. (2015). High-pressure metamorphism in the southern New England Orogen: Implications for long-lived accretionary orogenesis in eastern Australia. *Tectonics, 34*(9), 1979-2010. doi:10.1002/2015tc003920

POWELL, R., & HOLLAND, T. (1988). An internally consistent datasetwith uncertainties and correlations: 3. Applications to geobarometry, worked examples and a computer program. *Journal of Metamorphic Geology, 6*, 173-204.

PROYER, A., ROLFO, F., ZHU, Y. F., CASTELLI, D., & COMPAGNONI, R. (2013). Ultrahigh-pressure metamorphism in the magnesite + aragonite stability field: evidence from two impure marbles from the Dabie-Sulu UHPM belt. *Journal of Metamorphic Geology, 31*, 35-48. doi:10.1111/jmg.12005

ROSENBAUM, G., LI, P., & RUBATTO, D. (2012). The contorted New England Orogen (eastern Australia): New evidence from U-Pb geochronology of early Permian granitoids. *Tectonics, 31*(1), n/a-n/a. doi:10.1029/2011tc002960

RUBATTO, D., MUNTENER, O., BARNHOORN, A., & GREGORY, C. (2008). Dissolution-reprecipitation of zircon at low-temperature, high-pressure conditions (Lanzo Massif, Italy). *American Mineralogist, 93*(10), 1519-1529. doi:10.2138/am.2008.2874

SANDIFORD, M., FODEN, J., ZHOU, S. H., & TURNER, S. (1992). GRANITE GENESIS AND THE MECHANICS OF CONVERGENT OROGENIC BELTS WITH APPLICATION TO THE SOUTHERN ADELAIDE FOLD BELT. *Transactions of the Royal Society of Edinburgh-Earth Sciences, 83*, 83-93.

SANO, S., OFFLER, R., HYODO, H., & WATANABE, T. (2004). Geochemistry and Chronology of Tectonic Blocks in Serpentinite Mélange of the Southern New England Fold Belt, NSW, Australia. *Gondwana Research, 7*(3), 817-831. doi:10.1016/s1342-937x(05)71066-2

SCHERER, E. E., CAMERON, K. L., & BLICHERT-TOFT, J. (2000). Lu-Hf garnet geochronology: Closure temperature relative to the Sm-Nd system and the effects of trace mineral inclusions. *Geochemica et Cosmochimica Acta, 64*(19), 3413-3432.

SHAW, S. E., & FLOOD, R. H. (1974). Eclogite from serpentinite near Attunga, New South Wales. *Journal of the Geological Society of Australia, 21*(4), 377-385. doi:10.1080/00167617408728859

SIRCOMBE, K. N. (1999). Tracing provenance through the isotope ages of littoral and sedimentary detrital zircon, eastern Australia. *Sedimentary Geology*(124), 47-67.

SKORA, S., BAUMGARTNER, L. P., MAHLEN, N. J., JOHNSON, C. M., PILET, S., & HELLEBRAND, E. (2006). Diffusion-limited REE uptake by eclogite garnets and its consequences for Lu–Hf and Sm–Nd geochronology. *Contributions to Mineralogy and Petrology, 152*(6), 703-720. doi:10.1007/s00410-006-0128-x

SMIT, M. A., SCHERER, E. E., & MEZGER, K. (2013). Lu–Hf and Sm–Nd garnet geochronology: Chronometric closure and implications for dating petrological processes. *Earth and Planetary Science Letters, 381*, 222-233. doi:10.1016/j.epsl.2013.08.046

SQUIRE, R. J., WILSON, C. J. L., DUGDALE, L. J., JUPP, B. J., & KAUFMAN, A. L. (2006). Cambrian backarc-basin basalt in western Victoria related to evolution of a continent-dipping subduction zone. *Australian Journal of Earth Sciences, 53*(5), 707-719. doi:10.1080/08120090600827405

THIRLWALL, M. F., & ANCZKIEWICZ, R. (2004). Multidynamic isotope ratio analysis using MC–ICP–MS and the causes of secular drift in Hf, Nd and Pb isotope ratios. *International Journal of Mass Spectrometry, 235*(1), 59-81. doi:10.1016/j.ijms.2004.04.002

THÖNI, M. (2002). Sm–Nd isotope systematics in garnet from different lithologies (Eastern Alps): age results, and an evaluation of potential problems for garnet Sm–Nd chronometry. *Chemical Geology, 185*(3-4), 255-281. doi:10.1016/s0009-2541(01)00410-7

WATANABE, T., FANNING, C. M., LEITCH, E., & MORITA, T. (1999). Neoproterozoic Attunga Eclogite in Eastern Australia Margin. *Gondwana Research, 2*(4), 616. doi:10.1016/s1342-937x(05)70221-5

WEI, C. J., & CLARKE, G. L. (2011). Calculated phase equilibria for MORB compositions: a reappraisal of the metamorphic evolution of lawsonite eclogite. *Journal of Metamorphic Geology, 29*(9), 939-952. doi:10.1111/j.1525-1314.2011.00948.x

WHITE, R. W., POWELL, R., & HOLLAND, T. J. B. (2007). Progress relating to calculation of partial melting equilibria for metapelites. *Journal of Metamorphic Geology, 25*(5), 511-527. doi:10.1111/j.1525-1314.2007.00711.x

YOGODZINSKI, G. M., VERVOORT, J. D., BROWN, S. T., & GERSENY, M. (2010). Subduction controls of Hf and Nd isotopes in lavas of the Aleutian island arc. *Earth and Planetary Science Letters, 300*(3-4), 226-238. doi:10.1016/j.epsl.2010.09.035

ZACK, T., & JOHN, T. (2007). An evaluation of reactive fluid flow and trace element mobility in subducting slabs. *Chemical Geology, 239*(3-4), 199-216. doi:10.1016/j.chemgeo.2006.10.020

APPENDIX 1A: EXTENDED GEOCHRONOLOGY ANALYTICAL METHODS

Rock blocks were mounted into epoxy resin disks, and the surface polished. These were imaged using a Quanta 600 Scanning Electron Microscope (SEM) at Adelaide Microscopy. Images were produced in back-scattered electron imaging with the locations of zircon grains identified using X-ray spectra. Isotopic compositions of ^{204}Pb, ^{206}Pb, ^{207}Pb, ^{208}U, ^{232}Th and ^{238}U were measured using a New Wave 213nm Nd–YAG laser, coupled with an Agilent 7500cs/7500s ICP–MS at Adelaide Microscopy, following the methods of Payne *et al.* (2008). Given the small size of the zircons, a spot size of 10 μm was utilized, with 5 Hz frequency and a total acquisition time of 60 seconds, including 30 seconds of background measurement and 30 seconds of ablation. Data analyses and correction for mass bias and elemental fractionation were following Howard *et al.* (2011) utilizing the program Glitter, and the primary zircon standard GJ. Instrument drift was accounted for using a linear correction and standard bracketing every 5 zircon analyses.

APPENDIX 1B: EXTENDED ELECTRON PROBE MICRO ANALYSES METHODS

Spot analyses were untaken using a beam current of 20 nA and an accelerating voltage of 15 kV, with an andradite crystal analysed prior for calibration. Wavelength Dispersive Spectrometers (WDS) were used for the analysis of SiO_2, ZrO_2, TiO_2, ZnO, Al_2O_3, FeO, MnO, MgO, CaO, Ce, P_2O_5, Na_2O, K_2O and Cl. Element maps used a 200 nA beam current and an accelerating voltage of 15 kV, and Ca, Fe, Mn and Mg were mapped using WDS, whereas Al, Si, Ti, K, Na, Zr, Ce, Cl and F were mapped using Energy Dispersive Spectrometers (EDS).

APPENDIX 1C: EXTENDED PHASE EQUILIBRIA FORAWRD MODELLING METHODS

Calculations in THERMOCALC are based on the user identifying the stable mineral in a sample assemblage and calculating the mineral equilibria relationships reactions boundary by boundary (i.e. field boundaries), point by point (intersection of field boundaries), where lines signify the zero abundance of a phase and points signify the zero abundance of two phases. This method is very different to automated approaches, exemplified by methods such as Perple_X (Connolly and Petrini, 2002; Connolly, 2005) and Theriac (di Capitani and Petrakakis, 2010). The initial stable assemblage can be determined in THERMOCALC by performing a Gibbs energy minimisation calculation at a fixed P–T condition. The diagram is then built up and involves many trial and error calculations in order to determine which phases appear or disappear as a function of pressure, temperature and/or rock composition. In addition, 'starting guesses' (values for compositional variables for phases with which THERMOCALC commences its iterative least-squares calculation for a line or point) involve constant updating as the pseudosection is calculated in differing parts of P–T–X space (X: composition). The user must also understand these starting guesses, as in mafic rocks multiple amphiboles and pyroxenes have the ability to jump solvi and approach similar compositions. A single model comprises >150–300 line and point calculations, and the user intellectually, rather than passively, calculates every part of the diagram (this amounts to up to several months or more per model). The most uncertain compositional variables are H_2O and Fe_2O_3, usually requiring that these be constrained with P–M type calculations (where M refers to amount of an oxide component), preceding the calculation of the pressure–temperature (P–T) pseudosection.

APPENDIX 2A: EXTENDED ELECTRON PROBE MICRO ANALYSES

RB11	Garnet Rim	Garnet Core	Omphacite	Lawsonite	Titanite	Chlorite	Phengite	Glaucophane	Stilpnomelane
SiO_2	36.97	36.48	55.59	37.14	30.32	25.79	52.18	55.53	44.60
TiO_2	0.15	0.26	0.04	0.00	37.96	0.00	0.09	0.06	0.00
Al_2O_3	21.51	20.90	9.62	32.38	1.36	18.03	22.34	9.11	6.58
Cr_2O_3	0.00	0.00	0.00	0.00	0.00	0.00	0.00	0.01	0.00
FeO	29.00	21.13	6.16	0.25	0.18	30.65	4.25	17.25	25.03
MnO	0.79	11.43	0.01	0.00	0.00	1.09	0.02	0.17	1.61
MgO	1.03	0.17	7.89	0.00	0.00	10.56	3.98	6.44	6.70
ZnO	0.01	0.00	0.01	0.00	0.00	0.02	0.00	0.00	0.00
CaO	10.26	9.16	13.67	17.54	28.12	0.03	0.00	0.29	0.06
Na_2O	0.02	0.01	6.77	0.00	0.02	0.02	0.04	7.17	0.63
K_2O	0.01	0.00	0.00	0.00	0.06	0.01	11.04	0.06	1.44
Cl	0.00	0.00	0.01	0.00	0.00	0.00	0.00	0.01	0.00
F	0.05	0.08	0.00	0.00	0.06	0.06	0.00	0.00	0.01
Total	99.76	99.61	99.78	87.32	98.05	86.24	93.95	96.08	86.65
Cations									
Si	2.96	2.96	1.99	1.97	1.01	2.87	3.57	8.05	7.88
Ti	0.01	0.02	0.00	0.00	0.95	0.00	0.00	0.01	0.00
Al	2.03	2.00	0.41	2.03	0.05	2.36	1.80	1.56	1.37
Cr	0.00	0.00	0.00	0.00	0.00	0.00	0.00	0.00	0.00
Fe^{3+}	0.02	0.04	0.08	0.01	0.00	0.00	0.00	0.00	0.91
Fe^{2+}	1.92	1.39	0.11	0.00	0.00	2.85	0.24	2.09	2.79
Mn^{2+}	0.05	0.78	0.00	0.00	0.00	0.10	0.00	0.02	0.24
Mg	0.12	0.02	0.42	0.00	0.00	1.75	0.41	1.39	1.76
Zn	0.00	0.00	0.00	1.00	0.00	0.00	0.00	0.00	0.00
Ca	0.88	0.80	0.52	0.00	1.00	0.00	0.00	0.04	0.01
Na	0.00	0.00	0.47	0.00	0.00	0.00	0.01	2.01	0.21
K	0.00	0.00	0.00			0.00	0.00	0.97	0.01	0.32
Total cations (S)	8.00	8.00	4.00	5.01	3.02	9.94	7.00	15.18	15.50

RB12	Garnet Rim	Garnet Core	Chlorite	Glaucophane	Titanite	Rutile
SiO2	36.20	36.33	26.36	57.00	30.31	0.00
TiO2	0.30	0.76	0.00	0.00	39.03	96.51
Al2O3	21.39	20.99	17.89	11.04	0.73	0.06
Cr2O3	0.01	0.02	0.02	0.02	0.00	0.02
FeO	25.02	23.97	28.59	10.95	0.15	0.42
MnO	3.14	4.17	0.85	0.02	0.01	0.00
MgO	1.31	1.17	13.06	9.50	0.00	0.00
ZnO	0.00	0.01	0.00	0.04	0.00	0.00
CaO	11.05	11.08	0.01	0.51	28.27	0.08
Na2O	0.12	0.15	0.00	7.36	0.00	0.00
K2O	0.00	0.00	0.00	0.01	0.01	0.00
Cl	0.01	0.00	0.01	0.00	0.00	0.01
F	0.04	0.02	0.03	0.00	0.06	0.04
Total	98.57	98.67	86.81	96.44	98.55	97.12
Cations						
Si	2.92	2.93	2.87	7.97	1.00	0.00
Ti	0.02	0.05	0.00	0.00	0.97	1.00
Al	2.03	2.00	2.30	1.82	0.03	0.00
Cr	0.00	0.00	0.00	0.00	0.00	0.00
Fe3+	0.11	0.07	0.00	0.00	0.00	0.00
Fe2+	1.58	1.55	2.60	1.28	0.00	0.00
Mn2+	0.21	0.29	0.08	0.00	0.00	0.00
Mg	0.16	0.14	2.12	1.98	0.00	0.00
Zn	0.00	0.00	0.00	0.00	0.00	0.00
Ca	0.95	0.96	0.00	0.08	1.00	0.00
Na	0.02	0.02	0.00	1.99	0.00	0.00
K	0.00	0.00	0.00	0.00	0.00	0.00
Total cations	8.00	8.00	9.97	15.12	3.01	1.00

PB16	Garnet Rim	Garnet Core	Epidote	Omphacite	Titanite	Glaucophane	Chlorite
SiO2	36.20	36.33	36.58	53.59	29.67	53.86	25.93
TiO2	0.30	0.76	0.16	0.04	38.18	0.07	2.39
Al2O3	21.39	20.99	28.03	8.25	1.21	10.20	16.84
Cr2O3	0.01	0.02	0.00	0.02	0.00	0.00	0.00
FeO	25.02	23.97	6.62	7.82	0.16	14.96	27.31
MnO	3.14	4.17	0.95	0.13	0.02	0.08	0.45
MgO	1.31	1.17	0.23	7.25	0.00	7.56	11.75
ZnO	0.00	0.01	0.05	0.00	0.00	0.00	0.00
CaO	11.05	11.08	22.71	13.77	27.90	1.54	1.78
Na2O	0.12	0.15	0.00	6.36	0.01	6.45	0.00
K2O	0.00	0.00	0.03	0.02	0.01	0.06	0.00
Cl	0.01	0.00	0.00	0.01	0.00	0.00	0.00
F	0.04	0.02	0.00	0.00	0.02	0.00	0.06
Total	98.57	98.67	95.37	97.25	97.18	94.77	86.48
Cations							
Si	2.92	2.93	5.80	1.99	1.00	7.86	2.84
Ti	0.02	0.05	0.02	0.00	0.96	0.01	0.20
Al	2.03	2.00	5.24	0.36	0.05	1.75	2.17
Cr	0.00	0.00	0.00	0.00	0.00	0.00	0.00
Fe3+	0.11	0.07	0.00	0.12	0.00	0.00	0.00
Fe2+	1.58	1.55	0.88	0.12	0.00	1.83	2.50
Mn2+	0.21	0.29	0.13	0.00	0.00	0.01	0.04
Mg	0.16	0.14	0.06	0.40	0.00	1.65	1.92
Zn	0.00	0.00	0.01	0.00	0.00	0.00	0.00
Ca	0.95	0.96	3.86	0.55	1.00	0.24	0.21
Na	0.02	0.02	0.00	0.46	0.00	1.82	0.00
K	0.00	0.00	0.01	0.00	0.00	0.01	0.00
Total cations	8.00	8.00	16.00	4.00	3.02	15.17	9.87

APPENDIX 2B: EXTENDED ELECTRON PROBE ELEMENTAL MAPS
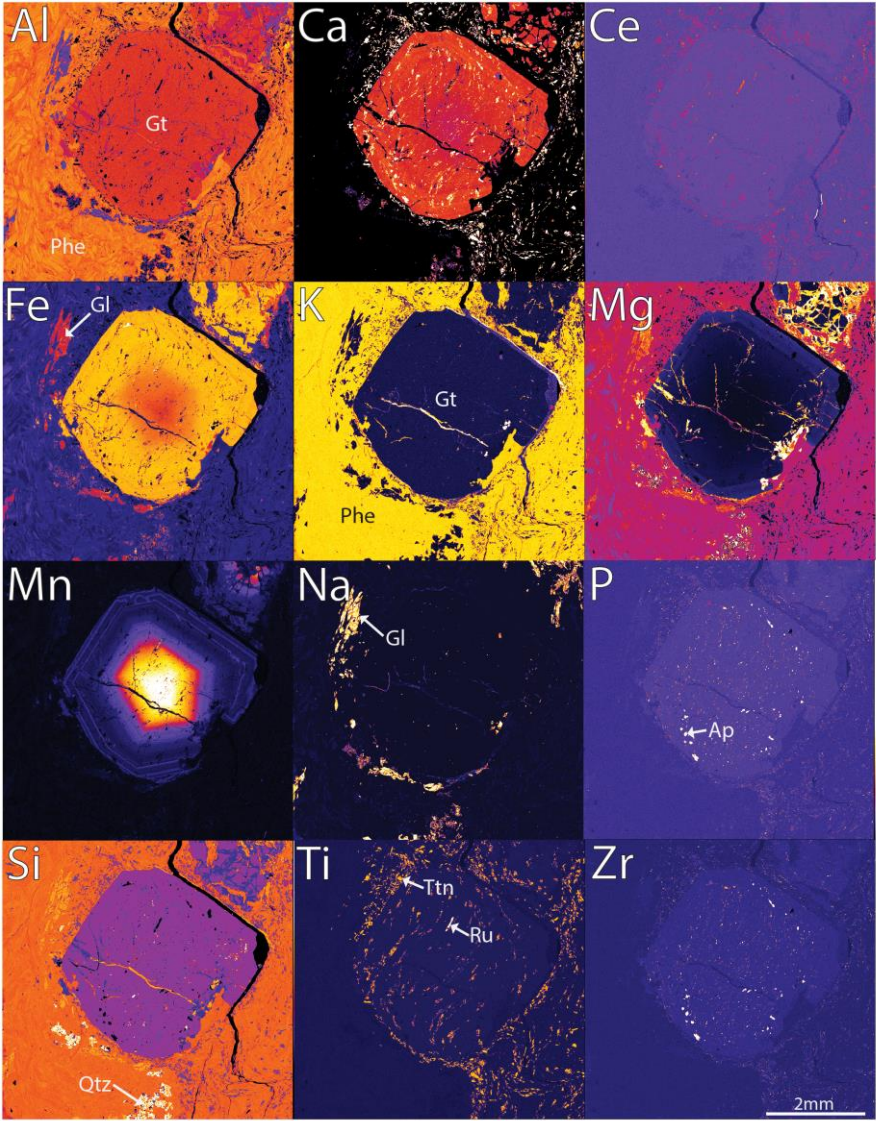
RB11 - Garnet
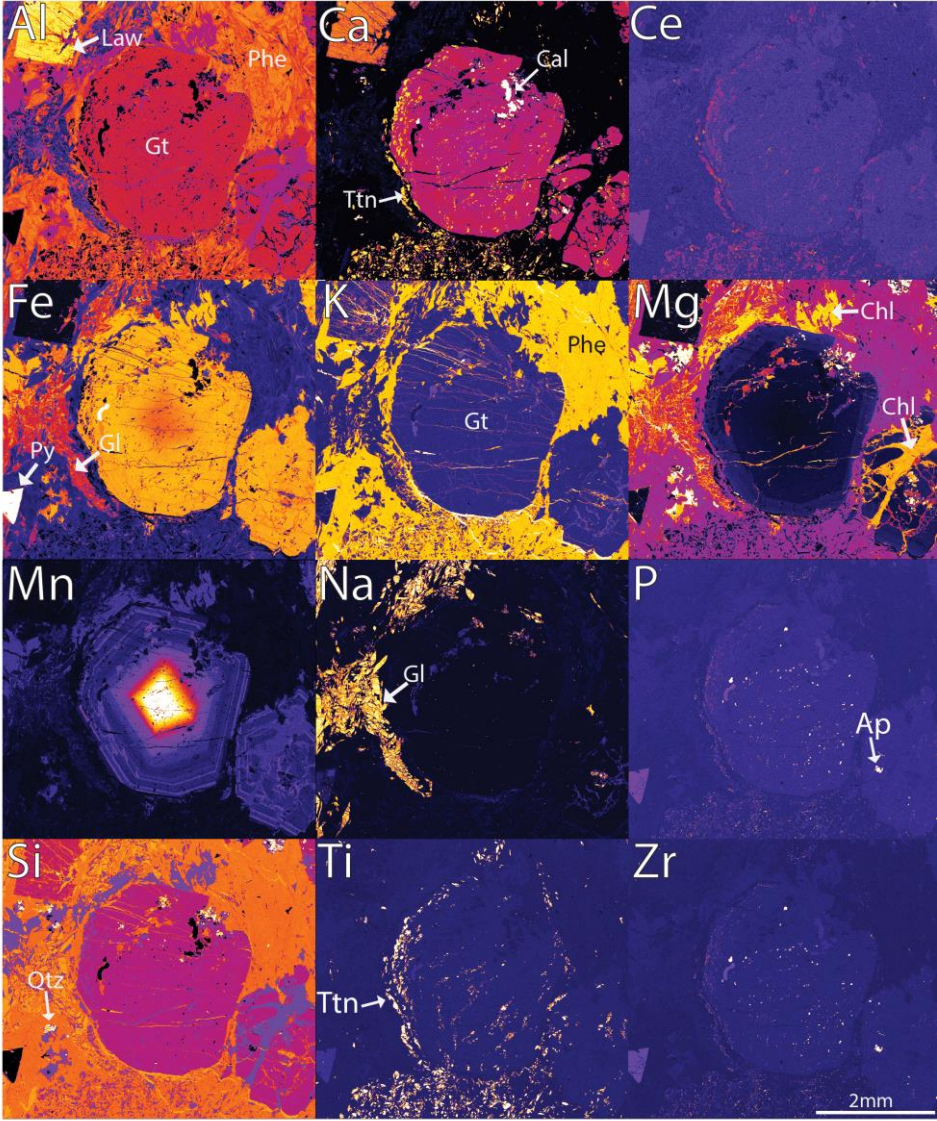
RB11 - Garnet
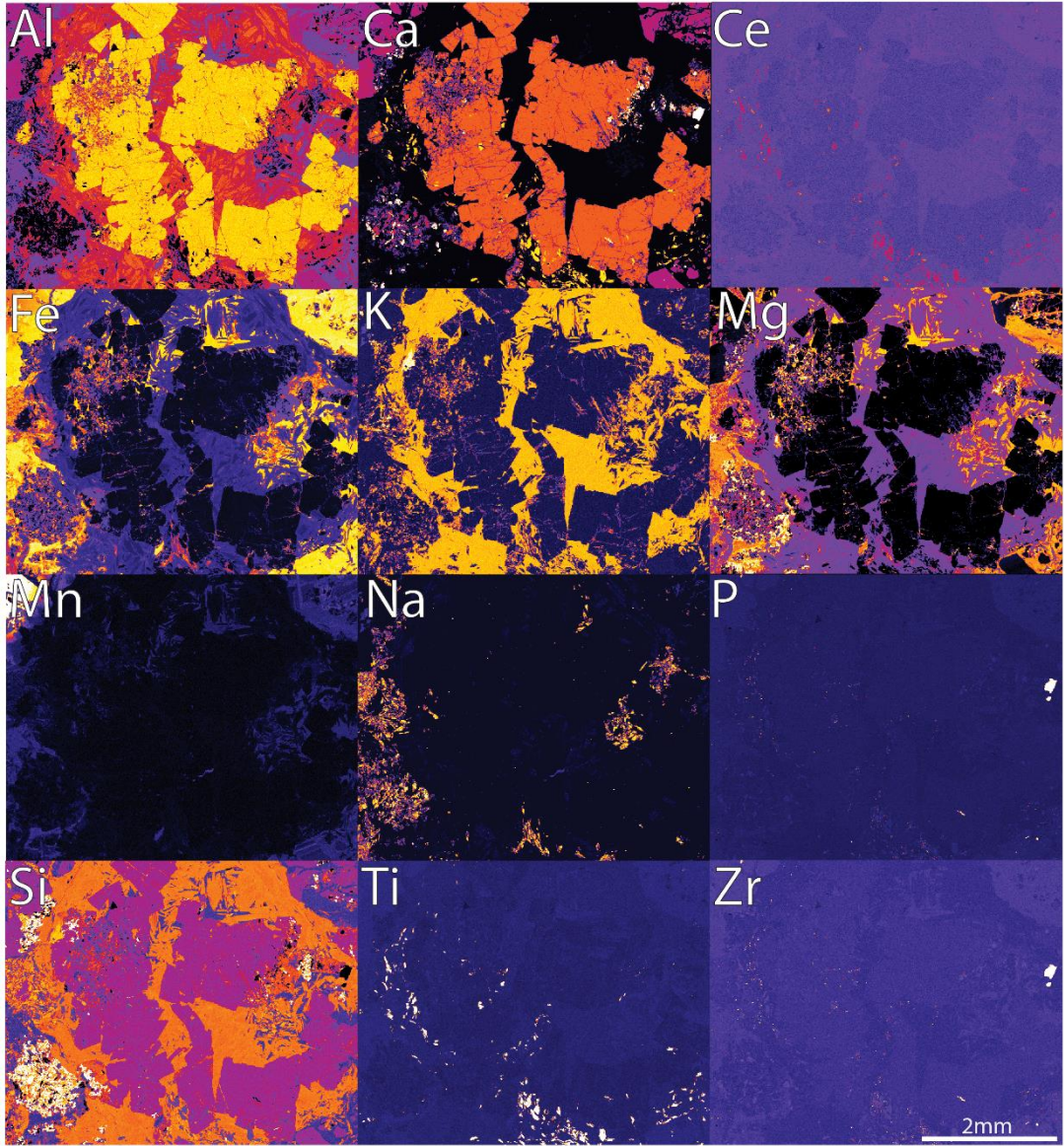
RB11 – Lawsonite and matrix
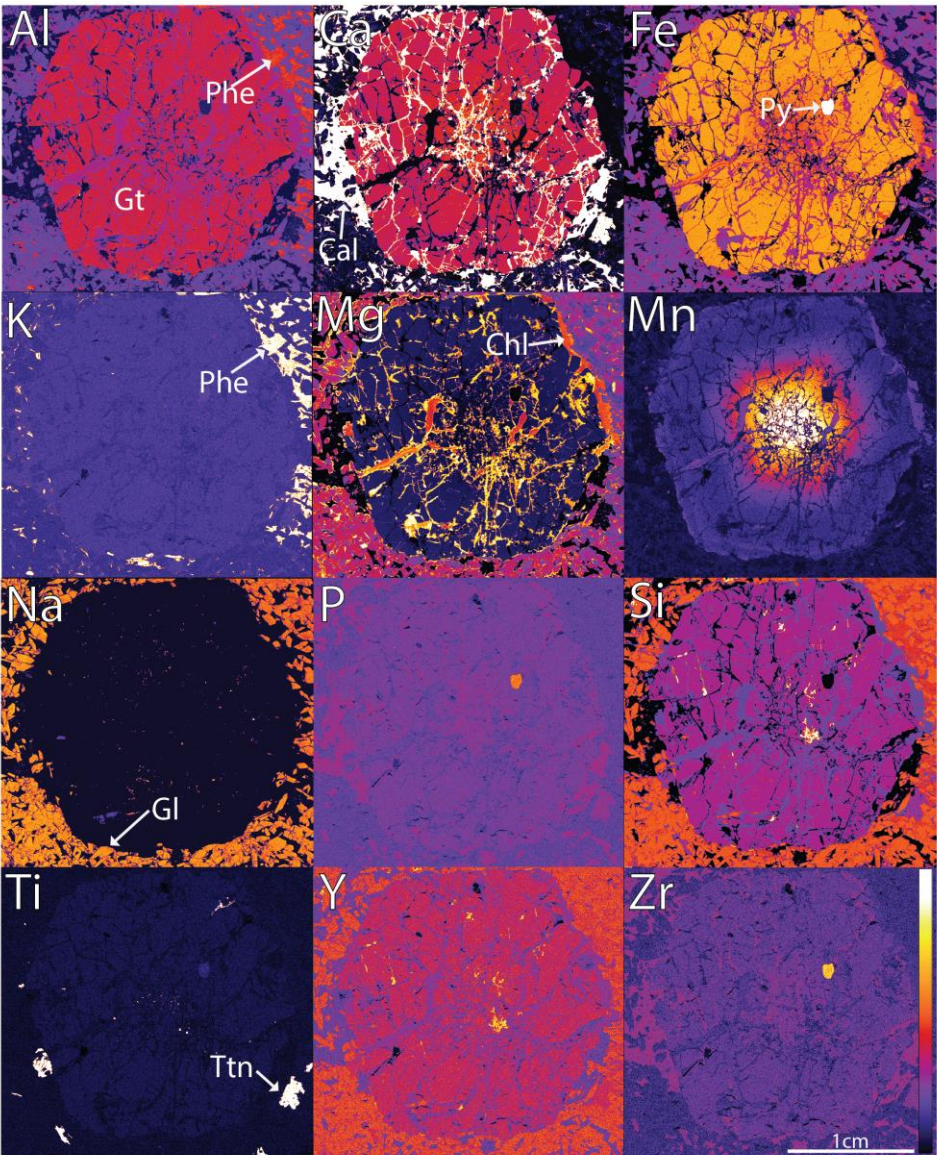
RB12 - Garnet
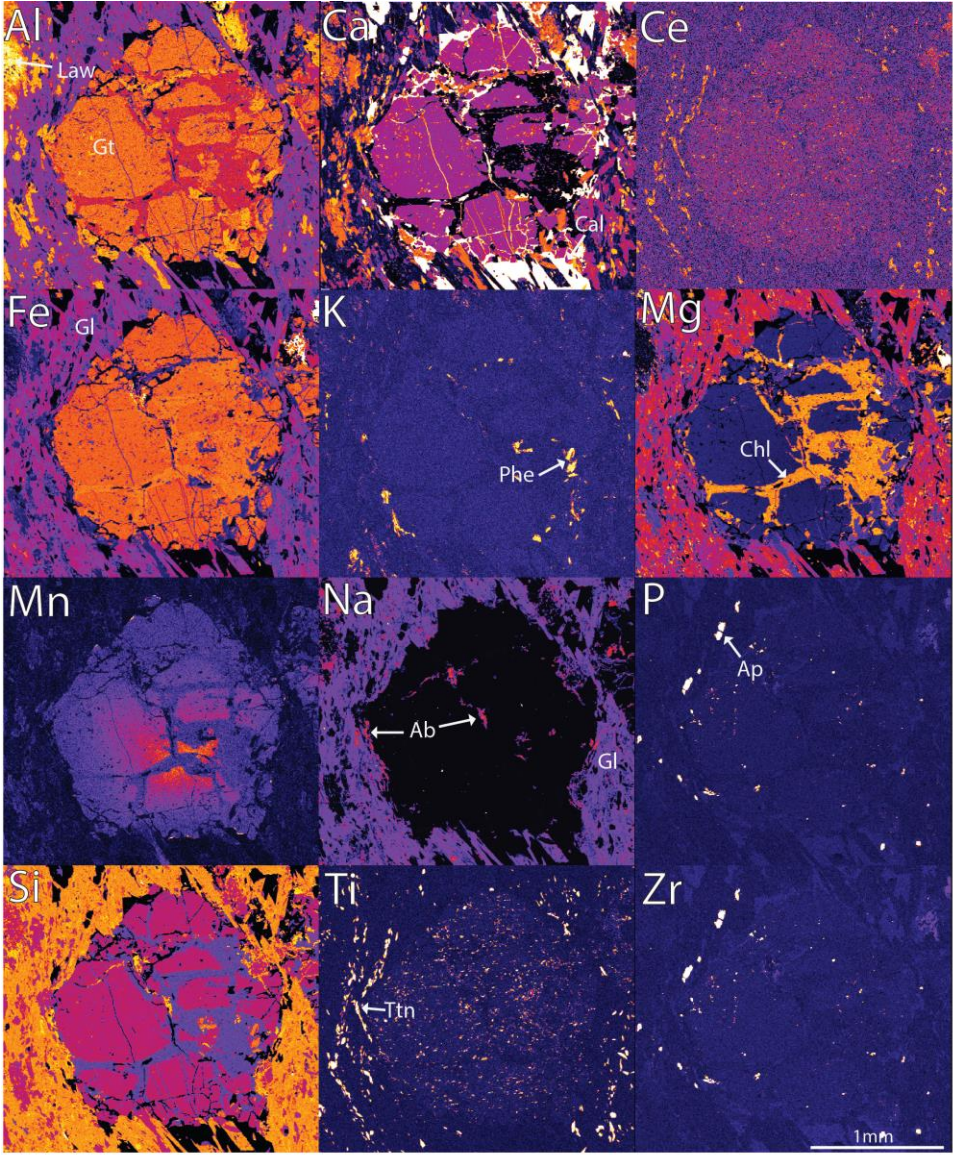
PB16 - Garnet

APPENDIX 3: U-PB GEOCHRONOLOGY DATA

	Pb207/Pb206	1σ	Pb206/U238	1σ	Pb207/U235	1σ	Pb208/Th232	1σ	conc	Pb207/Pb206	1σ	Pb206/U238	1σ	Pb207/U235	1σ	Pb208/Th232	1σ
GJ session 1																	
GJ01	0.05853	0.00329	0.10838	0.00241	0.87047	0.04667	0.02551	0.00576	120.6658177	549.7	118.16	663.3	14.03	635.8	25.34	509.2	113.61
GJ02	0.0633	0.00217	0.09251	0.00146	0.80578	0.02645	0.03743	0.00544	79.38761308	718.5	71.07	570.4	8.59	600.1	14.88	742.7	106.05
GJ03	0.05921	0.00202	0.08828	0.00137	0.71929	0.02361	0.03367	0.00515	94.88428745	574.7	72.53	545.3	8.09	550.2	13.94	669.3	100.63
GJ04	0.05872	0.00203	0.09016	0.00141	0.72772	0.02416	0.03524	0.00473	99.94612069	556.8	73.67	556.5	8.36	555.2	14.2	699.9	92.4
GJ05	0.05869	0.00203	0.09493	0.00148	0.76631	0.02548	0.03563	0.00561	105.18172	555.8	73.71	584.6	8.72	577.6	14.65	707.7	109.44
GJ06	0.05761	0.00197	0.08837	0.00137	0.6998	0.02294	0.0288	0.00398	106.0823941	514.6	73.56	545.9	8.14	538.7	13.7	574	78.16
GJ07	0.06116	0.00664	0.09762	0.00409	0.82315	0.08414	0.04307	0.01158	93.10077519	645	217.66	600.5	24.01	609.8	46.86	852.3	224.44
GJ08	0.0669	0.00546	0.09285	0.00316	0.85442	0.06515	0.04541	0.00819	68.57553612	834.7	161.53	572.4	18.64	627.1	35.67	897.6	158.28
GJ09	0.06419	0.0048	0.08874	0.00261	0.78143	0.05517	0.06996	0.01363	73.27540107	748	150.43	548.1	15.47	586.3	31.45	1366.9	257.45
GJ10	0.05969	0.00209	0.08643	0.00136	0.70957	0.0239	0.02479	0.0046	90.13324338	592.9	73.71	534.4	8.05	544.5	14.2	495	90.7
GJ11	0.05927	0.00205	0.0891	0.00139	0.72632	0.02418	0.0339	0.00557	95.33876278	577.1	73.55	550.2	8.23	554.4	14.22	673.7	108.82
GJ12	0.05856	0.00204	0.08525	0.00133	0.68663	0.02303	0.03216	0.00517	95.73425304	550.9	74.39	527.4	7.91	530.8	13.86	639.8	101.26
GJ13	0.06029	0.00209	0.08282	0.00129	0.68674	0.02286	0.02571	0.00467	83.56409839	613.9	73.14	513	7.71	530.8	13.76	513.1	91.98
GJ14	0.05886	0.00184	0.12956	0.00202	1.05168	0.03214	0.04019	0.00527	139.7508897	562	66.8	785.4	11.51	729.7	15.9	796.4	102.37
GJ15	0.06114	0.00186	0.11598	0.00179	0.97776	0.02898	0.04436	0.00476	109.8276665	644.1	64.06	707.4	10.31	692.5	14.88	877.4	92.2
GJ16	0.06158	0.00211	0.10022	0.00162	0.85102	0.0282	0.03588	0.00591	93.358605	659.5	71.68	615.7	9.49	625.2	15.47	712.5	115.38
GJ17	0.05911	0.00184	0.09999	0.00154	0.81509	0.02471	0.02999	0.00455	107.5630252	571.2	66.23	614.4	9.04	605.3	13.82	597.3	89.33
GJ18	0.06005	0.00188	0.11249	0.00175	0.9315	0.02849	0.03291	0.00492	113.5304808	605.3	66.49	687.2	10.15	668.4	14.98	654.5	96.36
GJ19	0.05985	0.00188	0.1091	0.0017	0.90041	0.02762	0.03663	0.00509	111.6034108	598.1	66.74	667.5	9.86	651.9	14.76	727.1	99.26
GJ20	0.0597	0.00191	0.10049	0.00157	0.82727	0.02571	0.02928	0.00495	104.0802563	593.1	67.27	617.3	9.18	612.1	14.29	583.4	97.27
GJ21	0.05896	0.00436	0.09846	0.00283	0.79734	0.05592	0.02309	0.00441	107.0367751	565.6	153.53	605.4	16.63	595.3	31.59	461.3	87.15
GJ22	0.0597	0.00251	0.10474	0.00186	0.86129	0.03473	0.03537	0.00664	108.2785365	593.1	88.06	642.2	10.84	630.8	18.95	702.6	129.67
GJ23	0.06119	0.00196	0.09563	0.00148	0.80704	0.02509	0.03744	0.0049	91.15962223	645.9	67.5	588.8	8.7	600.8	14.1	743	95.52
GJ24	0.06056	0.00266	0.09202	0.00173	0.76851	0.03243	0.03586	0.00586	90.98925766	623.7	92.01	567.5	10.23	578.9	18.62	712.1	114.35
GJ25	0.05944	0.00203	0.12569	0.002	1.03031	0.03403	0.04306	0.00624	130.8866404	583.1	72.39	763.2	11.46	719.1	17.02	852.1	120.86
GJ26	0.05796	0.00251	0.10994	0.00201	0.87911	0.03668	0.0254	0.00596	127.3484848	528	92.53	672.4	11.66	640.5	19.82	507.1	117.56
GJ27	0.05851	0.002	0.09763	0.00146	0.78758	0.02579	0.03257	0.00526	109.4006194	548.9	72.87	600.5	8.59	589.8	14.65	647.9	103.02
GJ28	0.05919	0.00188	0.09383	0.00137	0.76501	0.02323	0.02719	0.00338	100.7318348	573.9	67.44	578.1	8.09	576.9	13.37	542.2	66.58
GJ29	0.05881	0.00215	0.08939	0.00143	0.72404	0.0254	0.0277	0.0041	98.57142857	560	77.87	552	8.46	553.1	14.96	552.3	80.67

GJ30	0.06496	0.00433	0.09626	0.00261	0.86006	0.05404	0.03818	0.00604	76.62959131	773.2	134.35	592.5	15.34	630.2	29.5	757.3	117.6
GJ31	0.05829	0.00191	0.08955	0.00131	0.71958	0.02264	0.02598	0.00406	102.4268247	539.8	70.76	552.9	7.77	550.4	13.37	518.5	79.96
GJ32	0.06016	0.00209	0.08649	0.00131	0.71739	0.02382	0.0279	0.00481	87.77285409	609.3	73.25	534.8	7.78	549.1	14.08	556.2	94.51
GJ33	0.06469	0.00208	0.13709	0.00212	1.22219	0.03798	0.04657	0.00562	108.374771	764.2	66.48	828.2	12.02	810.8	17.36	920.1	108.58
GJ34	0.0598	0.00204	0.12081	0.00191	0.99599	0.03272	0.0394	0.00451	123.2729712	596.4	72.17	735.2	10.98	701.8	16.65	781.1	87.76
GJ35	0.06124	0.00215	0.10119	0.00164	0.85452	0.02879	0.02745	0.00371	95.93947815	647.7	73.58	621.4	9.59	627.1	15.76	547.4	73.04
GJ36	0.05641	0.00215	0.09269	0.00149	0.72067	0.0265	0.01656	0.00526	122.1723327	467.7	82.82	571.4	8.8	551.1	15.64	331.9	104.5
GJ37	0.06069	0.002	0.09653	0.00148	0.80748	0.02571	0.03351	0.00467	94.57179242	628.2	69.59	594.1	8.72	601	14.44	666.1	91.39
GJ38	0.06062	0.00237	0.09884	0.00167	0.82607	0.03112	0.03367	0.00652	97.12276215	625.6	82.27	607.6	9.81	611.4	17.3	669.4	127.55
GJ39	0.06257	0.0041	0.18243	0.00523	1.56875	0.09667	0.03907	0.00503	155.7157273	693.7	133.92	1080.2	28.53	957.9	38.21	774.6	97.75
GJ40	0.06065	0.00193	0.14015	0.00214	1.17123	0.03586	0.0386	0.00407	134.8484848	627	67.11	845.5	12.11	787.2	16.77	765.4	79.23
GJ41	0.05795	0.00198	0.11304	0.00175	0.90269	0.02972	0.03722	0.00531	130.8319121	527.7	73.35	690.4	10.11	653.2	15.86	738.7	103.57
GJ42	0.06201	0.00204	0.09484	0.00145	0.81025	0.0256	0.03319	0.00448	86.61032028	674.4	68.68	584.1	8.57	602.6	14.36	660	87.57
GJ43	0.05819	0.00222	0.09718	0.00161	0.77899	0.02859	0.03281	0.00531	111.5069004	536.2	81.91	597.9	9.48	584.9	16.32	652.6	104
GJ44	0.05845	0.00202	0.10136	0.00158	0.81623	0.02725	0.02826	0.00512	113.8467167	546.7	73.88	622.4	9.23	605.9	15.23	563.3	100.73
GJ45	0.06201	0.00282	0.11568	0.00212	0.98867	0.04297	0.02733	0.00673	104.6263345	674.4	94.3	705.6	12.23	698	21.94	544.9	132.48
GJ46	0.06081	0.0029	0.10379	0.0021	0.86827	0.03948	0.02862	0.00393	100.6482213	632.5	99.67	636.6	12.28	634.6	21.46	570.3	77.23
GJ47	0.05991	0.00195	0.10054	0.00151	0.82949	0.02603	0.03274	0.0043	102.8990337	600.2	69.02	617.6	8.85	613.3	14.45	651.1	84.12
GJ48	0.05836	0.00199	0.09815	0.00151	0.78889	0.02594	0.03192	0.0044	111.0783953	543.4	72.92	603.6	8.84	590.5	14.72	635.1	86.09
GJ49	0.06037	0.00215	0.12485	0.00198	1.03809	0.0356	0.03203	0.00574	122.937267	616.9	75.03	758.4	11.36	723	17.73	637.2	112.36
GJ50	0.06267	0.00206	0.11514	0.00178	0.99436	0.03149	0.03599	0.0044	100.7745267	697.2	68.59	702.6	10.32	700.9	16.03	714.7	85.91
GJ52	0.06096	0.00346	0.11316	0.00245	0.95066	0.05154	0.03914	0.01025	108.3568517	637.8	117.68	691.1	14.19	678.4	26.83	776	199.43
GJ53	0.06107	0.00221	0.11008	0.00176	0.92586	0.03228	0.02873	0.00553	104.925187	641.6	76.1	673.2	10.22	665.5	17.02	572.4	108.65
GJ54	0.06253	0.00246	0.09702	0.00165	0.83574	0.03154	0.0301	0.00599	86.2323028	692.2	81.64	596.9	9.68	616.8	17.45	599.4	117.49
GJ55	0.05735	0.0045	0.09773	0.00288	0.77127	0.05757	0.03447	0.00673	119.147671	504.5	164.5	601.1	16.94	580.5	33	684.9	131.42
GJ session 2																	
STDGJ_01	0.06124	0.00457	0.09906	0.00228	0.83638	0.06185	0.02071	0.00795	93.9950602	647.8	152.73	608.9	13.36	617.1	34.2	414.2	157.46
STDGJ_02	0.06227	0.0035	0.0971	0.00188	0.83351	0.04695	0.05146	0.00971	87.42865506	683.3	115.81	597.4	11.06	615.6	26	1014.3	186.61
STDGJ_03	0.05994	0.00329	0.09413	0.0018	0.77767	0.04285	0.02573	0.00659	96.4410444	601.3	114.71	579.9	10.61	584.2	24.47	513.5	129.93
STDGJ_04	0.10683	0.00506	0.09859	0.00203	1.37077	0.06514	0.00051	0.00651	34.71935853	1746	84.28	606.2	11.91	876.5	27.9	10.3	131.52
STDGJ_05	0.06895	0.00604	0.0898	0.0022	0.85224	0.07363	0.02676	0.01169	61.79224253	897.2	170.95	554.4	13.03	625.9	40.36	533.7	230.05
STDGJ_06	0.05798	0.00366	0.09998	0.00202	0.79888	0.05036	0.02277	0.00792	116.2346263	528.5	133.04	614.3	11.81	596.2	28.42	455	156.49
STDGJ_07	0.0593	0.00518	0.0931	0.00225	0.75992	0.06559	0.04145	0.01482	99.29065744	578	179.31	573.9	13.29	574	37.84	820.9	287.53
STDGJ_08	0.05279	0.00425	0.10398	0.00233	0.75663	0.05974	0.02905	0.01111	199.5306633	319.6	172.93	637.7	13.62	572.1	34.53	578.8	218.22

STDGJ_09	0.06076	0.00385	0.09565	0.00193	0.80109	0.04996	0.03297	0.00968	93.37244332	630.7	131.07	588.9	11.36	597.4	28.16	655.6	189.44
STDGJ_10	0.06	0.00383	0.09754	0.00218	0.8069	0.05197	0.03466	0.00398	99.43652635	603.4	132.42	600	12.79	600.7	29.21	688.8	77.71
STDGJ_11	0.05375	0.00491	0.09119	0.00223	0.67584	0.06033	0.03537	0.01539	156.1043285	360.4	193.87	562.6	13.19	524.3	36.55	702.5	300.45
STDGJ_12	0.05843	0.00618	0.10125	0.00281	0.81547	0.08414	0.04064	0.01939	113.8436184	546.1	215.69	621.7	16.45	605.5	47.06	805.2	376.63
STDGJ_13	0.05869	0.0045	0.0988	0.0022	0.79877	0.06025	0.03298	0.01108	109.3429343	555.5	158.98	607.4	12.89	596.1	34.01	655.8	216.77
STDGJ_14	0.06161	0.00423	0.09397	0.00198	0.7978	0.0542	0.02191	0.00861	87.6475931	660.6	140.79	579	11.7	595.6	30.61	438.2	170.33
STDGJ_15	0.05955	0.00534	0.1011	0.00258	0.82968	0.07333	0.03571	0.01061	105.7571112	587.1	183.51	620.9	15.09	613.4	40.7	709.2	207.13
STDGJ_16	0.06047	0.00421	0.10024	0.00214	0.8348	0.05757	0.03763	0.01098	99.24254633	620.5	143.43	615.8	12.56	616.3	31.86	746.7	213.93
STDGJ_17	0.05991	0.00425	0.09389	0.002	0.77509	0.05449	0.04174	0.01167	96.35243171	600.4	146.43	578.5	11.8	582.7	31.17	826.5	226.43
STDGJ_18	0.0603	0.00453	0.09509	0.00215	0.78904	0.0588	0.02882	0.00758	95.3125	614.4	154.6	585.6	12.63	590.6	33.37	574.3	148.87
STDGJ_19	0.05721	0.00432	0.09334	0.00206	0.73486	0.05515	0.03148	0.00878	115.2905812	499	158.55	575.3	12.17	559.4	32.28	626.5	172.11
STDGJ_20	0.05267	0.00603	0.09291	0.00271	0.6729	0.07619	0.03254	0.01036	181.9828408	314.7	241.4	572.7	16	522.5	46.24	647.2	202.85
STDGJ_21	0.0594	0.00445	0.09388	0.00205	0.76805	0.05733	0.02821	0.00926	99.44979367	581.6	154.98	578.4	12.09	578.6	32.92	562.3	182.11
STDGJ_22	0.05783	0.00339	0.10099	0.00195	0.80369	0.04721	0.03188	0.0079	118.585086	523	123.82	620.2	11.43	598.9	26.58	634.3	154.69
STDGJ_23	0.05894	0.00527	0.10394	0.00262	0.84156	0.07438	0.03909	0.01012	112.8740924	564.7	183.57	637.4	15.32	620	41.01	775	196.82
STDGJ_24	0.05848	0.00496	0.09696	0.00226	0.77965	0.0655	0.03492	0.01082	108.8686131	548	175.37	596.6	13.27	585.3	37.37	693.9	211.31
STDGJ_25	0.06253	0.00463	0.09366	0.00212	0.80616	0.05921	0.02781	0.00754	83.38390406	692.1	150.47	577.1	12.51	600.3	33.29	554.5	148.24
STDGJ_26	0.06628	0.00556	0.09391	0.00224	0.85652	0.07104	0.02522	0.00902	70.9764475	815.2	166.2	578.6	13.23	628.2	38.85	503.4	177.88
STDGJ_27	0.05666	0.00412	0.09677	0.00205	0.75536	0.05456	0.01498	0.00763	124.6598283	477.7	153.74	595.5	12.04	571.3	31.56	300.5	151.96
STDGJ_28	0.06419	0.00431	0.09565	0.00205	0.84619	0.05649	0.02951	0.00711	78.74047333	747.9	135.91	588.9	12.06	622.6	31.07	587.9	139.56
STDGJ_29	0.06413	0.00479	0.1005	0.00225	0.88769	0.06558	0.04708	0.01076	82.7613941	746	150.53	617.4	13.15	645.1	35.28	929.9	207.67
STDGJ_30	0.06224	0.00404	0.09834	0.00204	0.84208	0.05439	0.02883	0.00754	88.6137163	682.4	132.94	604.7	11.97	620.3	29.98	574.5	148.15
STDGJ_31	0.0649	0.00359	0.0993	0.00193	0.88726	0.0491	0.03337	0.00666	79.14667358	771.1	112.33	610.3	11.34	644.9	26.41	663.4	130.22
STDGJ_32	0.06121	0.00338	0.09519	0.00182	0.80229	0.04432	0.04928	0.00695	90.67285383	646.5	114.24	586.2	10.71	598.1	24.97	972.4	133.83
STDGJ_33	0.0599	0.00428	0.09467	0.002	0.78099	0.0554	0.02328	0.0087	97.19953326	599.9	147.74	583.1	11.76	586	31.59	465.2	171.78
STDGJ_34	0.05905	0.00406	0.09398	0.00195	0.76458	0.05223	0.02503	0.00792	101.7932489	568.8	143.08	579	11.51	576.7	30.06	499.7	156.19
STDGJ_35	0.06442	0.00353	0.09663	0.00186	0.85723	0.04703	0.02679	0.00687	78.69242986	755.6	111.6	594.6	10.94	628.6	25.71	534.4	135.31
STDGJ_36	0.05709	0.00493	0.12335	0.00339	0.9665	0.09556	0.42632	1.67395	151.6585761	494.4	180.45	749.8	19.43	686.7	49.34	7177.3	*******
STDGJ_37	0.0573	0.00556	0.12	0.00359	0.9592	0.10437	0.06792	0.06902	145.3930348	502.5	200.77	730.6	20.66	682.9	54.09	1328.2	1306.3
STDGJ_38	0.0537	0.0043	0.11514	0.00283	0.84733	0.07254	0.0776	0.07912	195.9553696	358.5	171.13	702.5	16.36	623.2	39.87	1510.6	1484.06
STDGJ_39	0.06515	0.00582	0.10638	0.00275	0.94879	0.08762	0.57024	1.68848	83.64779874	779.1	177.49	651.7	16.04	677.5	45.65	9120.4	*******
STDGJ_40	0.0601	0.00387	0.09684	0.00197	0.8041	0.0515	0.03384	0.01299	98.13869214	607.1	133.32	595.8	11.58	599.1	28.98	672.7	253.97
STDGJ_41	0.05938	0.00411	0.09504	0.00196	0.77948	0.05315	0.02745	0.01246	100.7574453	580.9	143.7	585.3	11.54	585.2	30.33	547.3	245.16
STDGJ_42	0.05703	0.0039	0.09273	0.00185	0.73121	0.04886	0.02914	0.01004	116.2228095	491.9	144.62	571.7	10.93	557.3	28.66	580.5	197.17

STDGJ_44	0.06287	0.00519	0.11683	0.00242	1.01184	0.08011	0.01668	0.00582	101.1933513	703.9	166.45	712.3	13.99	709.8	40.43	334.3	115.68
STDGJ_45	0.05803	0.00824	0.09425	0.00304	0.75119	0.10274	0.03077	0.01201	109.4232944	530.6	284.57	580.6	17.89	568.9	59.57	612.6	235.5
STDGJ_46	0.05739	0.00492	0.08394	0.00177	0.66434	0.05552	0.01922	0.00637	102.647175	506.2	178.54	519.6	10.53	517.3	33.87	384.7	126.37
STDGJ_47	0.0567	0.00496	0.11899	0.00266	0.93098	0.08107	0.0371	0.01105	151.2520868	479.2	183.24	724.8	15.32	668.1	42.63	736.2	215.45
STDGJ_48	0.05873	0.00569	0.10003	0.00252	0.81042	0.07844	0.03143	0.0111	110.3015075	557.2	198.2	614.6	14.77	602.7	44	625.6	217.54
STDGJ_49	0.05597	0.00561	0.09142	0.00235	0.70649	0.07146	0.02282	0.01064	125.1386732	450.7	208.84	564	13.87	542.7	42.52	456	210.23
STDGJ_50	0.05175	0.00394	0.11772	0.00265	0.83657	0.06347	0.03965	0.01102	261.3479053	274.5	165.37	717.4	15.29	617.3	35.09	785.9	214.16
STDGJ_51	0.05882	0.00443	0.1095	0.0025	0.88495	0.06632	0.02781	0.01026	119.5217702	560.4	156.26	669.8	14.51	643.7	35.73	554.5	201.68
STDGJ_52	0.04991	0.00497	0.10571	0.00282	0.72466	0.07146	0.02398	0.01961	339.6958574	190.7	216.59	647.8	16.42	553.4	42.07	478.9	387.06
STDGJ_53	0.0602	0.00589	0.09508	0.0026	0.788	0.07573	0.01576	0.01335	95.84220003	610.9	198.3	585.5	15.32	590	43	316	265.65
STDGJ_54	0.0599	0.00612	0.09953	0.00275	0.82018	0.08224	0.03119	0.01097	101.9839947	599.8	207.09	611.7	16.09	608.1	45.88	620.7	215.08
STDGJ_55	0.05486	0.00456	0.09884	0.00224	0.74717	0.06134	0.03753	0.0137	149.507874	406.4	176.23	607.6	13.17	566.6	35.65	744.8	266.8
STDGJ_56	0.05446	0.00487	0.09499	0.00222	0.71323	0.06288	0.02843	0.01313	149.9615483	390.1	189.25	585	13.04	546.7	37.27	566.6	257.98
STDGJ_57	0.05863	0.00559	0.1066	0.00259	0.86195	0.08007	0.02945	0.01669	118.0191578	553.3	195.63	653	15.08	631.2	43.67	586.6	327.64
STDGJ_58	0.0586	0.00574	0.105	0.00259	0.84867	0.08065	0.04078	0.02238	116.5278783	552.4	200.59	643.7	15.13	623.9	44.3	808	434.7
STDGJ_59	0.06144	0.00627	0.09865	0.00249	0.83571	0.0822	0.00959	0.01414	92.65200122	654.6	205.11	606.5	14.59	616.8	45.47	193	283.01
STDGJ_60	0.05792	0.00699	0.09718	0.00275	0.77577	0.09016	0.03726	0.02267	113.5396886	526.6	245.03	597.9	16.15	583.1	51.55	739.5	441.82
Ples session 1																	
PLES01	0.05332	0.00166	0.04875	0.00071	0.35767	0.01073	0.01793	0.00205	89.68439509	342.2	68.9	306.9	4.35	310.5	8.03	359.2	40.79
PLES02	0.05504	0.00169	0.0477	0.00069	0.36109	0.01072	0.01759	0.00196	72.57791737	413.9	66.74	300.4	4.25	313	7.99	352.4	38.94
PLES03	0.05436	0.00146	0.05435	0.00078	0.40747	0.01079	0.01765	0.00128	88.37088837	386.1	59.13	341.2	4.76	347.1	7.78	353.7	25.49
PLES04	0.05333	0.0016	0.04979	0.00072	0.36635	0.01067	0.0163	0.00136	91.3677457	342.9	66.36	313.3	4.45	316.9	7.93	326.9	27.01
PLES05	0.05245	0.00195	0.05064	0.0008	0.36582	0.01309	0.01643	0.00167	104.3577982	305.2	82.7	318.5	4.88	316.6	9.73	329.4	33.21
PLES06	0.05392	0.00197	0.05158	0.0008	0.38325	0.01349	0.01987	0.0021	88.21768707	367.5	80.15	324.2	4.9	329.4	9.9	397.6	41.63
PLES07	0.05614	0.002	0.05273	0.00082	0.40782	0.01399	0.01711	0.00182	72.36180905	457.7	76.91	331.2	5.05	347.3	10.09	343	36.16
PLES08	0.05444	0.00198	0.08624	0.00134	0.64664	0.02276	0.01923	0.00196	137.0951157	389	79.08	533.3	7.97	506.4	14.03	385	38.94
Ples session 2																	
PLES_01	0.05617	0.00284	0.0511	0.00095	0.39569	0.0201	0.01844	0.003	70.03051439	458.8	108.58	321.3	5.82	338.5	14.62	369.3	59.49
PLES_02	0.05476	0.00289	0.05125	0.00096	0.38677	0.02048	0.01804	0.00305	80.0695825	402.4	113.62	322.2	5.9	332	14.99	361.4	60.52
PLES_03	0.05162	0.00276	0.06713	0.00124	0.47751	0.02542	0.02134	0.00367	155.9776536	268.5	118.35	418.8	7.51	396.4	17.47	426.9	72.56
PLES_04	0.05179	0.00329	0.06237	0.00126	0.44513	0.028	0.01754	0.00331	141.1509229	276.3	139.08	390	7.64	373.9	19.68	351.5	65.83
PLES_05	0.04178	0.00252	0.05207	0.00095	0.29966	0.01816	0.01493	0.00208	327200	0.1	0	327.2	5.81	266.1	14.18	299.6	41.43
PLES_06	0.05257	0.00263	0.05332	0.00097	0.38602	0.01947	0.01385	0.00197	107.9626048	310.2	109.93	334.9	5.96	331.5	14.26	278	39.35
PLES_07	0.05723	0.00282	0.05014	0.00092	0.39522	0.01966	0.01197	0.00157	63.09261852	499.9	105.64	315.4	5.67	338.2	14.3	240.5	31.35

PLES_08	0.05383	0.0027	0.05267	0.00097	0.39059	0.01975	0.01309	0.00169	90.98157822	363.7	108.74	330.9	5.94	334.8	14.42	262.8	33.68
PLES_09	0.05371	0.00384	0.05372	0.00111	0.39722	0.02821	0.0161	0.00228	93.98161048	358.9	153.47	337.3	6.76	339.6	20.5	322.8	45.41
PLES_10	0.05272	0.00322	0.05357	0.00102	0.38891	0.02377	0.01559	0.0018	106.1533607	316.9	132.91	336.4	6.27	333.6	17.38	312.7	35.79
PLES_11	0.05495	0.00327	0.05655	0.00117	0.42957	0.02661	0.0312	0.01339	86.42456739	410.3	127.39	354.6	7.13	362.9	18.9	620.9	262.36
PLES_12	0.05726	0.00478	0.05359	0.00125	0.42389	0.03548	0.06629	0.0623	67.15226502	501.1	174.47	336.5	7.63	358.8	25.3	1297.3	1180.89
PLES_13	0.05317	0.00535	0.06487	0.00151	0.47579	0.04688	0.01495	0.0035	120.5952381	336	213.11	405.2	9.13	395.2	32.26	300	69.78
PLES_14	0.0507	0.00547	0.05181	0.00126	0.36251	0.03858	0.00867	0.00257	143.4361233	227	231.56	325.6	7.75	314.1	28.75	174.6	51.41
PLES_15	0.04776	0.00332	0.05553	0.00116	0.36504	0.02517	0.01246	0.00287	404.1763341	86.2	157.84	348.4	7.11	316	18.72	250.3	57.26
PLES_16	0.0532	0.00378	0.05842	0.00127	0.4275	0.03002	0.02049	0.00463	108.5731237	337.1	152.89	366	7.73	361.4	21.35	410	91.68

SAMPLES	Italicized: Not used															
	Pb207/Pb206	1σ	Pb207/U235	1σ	Pb206/U238	1σ	Pb208/Th232	1σ	conc	Pb207/Pb206	1σ	Pb206/U238	1σ	Pb207/U235	1σ	Pb208/Th232	1σ
R4-O	0.0552	0.00497	0.60151	0.05114	0.07935	0.00269	0.01115	0.00154	117.1068285	420.3	189.35	492.2	16.04	478.2	32.42	224.2	30.83
R4-ND	0.06707	0.00673	0.80534	0.07481	0.08746	0.00374	0.00804	0.0009	64.3452381	840	196.07	540.5	22.15	599.8	42.08	161.8	18.05
R4-NC	*0.09961*	*0.02325*	*1.04376*	*0.21321*	*0.07709*	*0.0094*	*0.01635*	*0.00318*	*29.61405245*	*1616.8*	*381.33*	*478.8*	*56.23*	*725.8*	*105.93*	*327.9*	*63.31*
R4-NB	0.05781	0.00424	0.62759	0.04375	0.07894	0.00218	0.0161	0.00199	93.7775225	522.3	153.33	489.8	13	494.6	27.3	322.8	39.51
R4-NA	0.05734	0.00822	0.65518	0.08859	0.08345	0.00441	0.01058	0.00256	102.4588539	504.3	288.28	516.7	26.23	511.7	54.34	212.8	51.26
R4-L	*0.0571*	*0.00412*	*0.52818*	*0.03599*	*0.06721*	*0.0019*	*0.00661*	*0.00198*	*84.70707071*	*495*	*152.23*	*419.3*	*11.48*	*430.6*	*23.91*	*133.3*	*39.86*
R4-JB	*0.34602*	*0.07598*	*8.98697*	*1.52583*	*0.19496*	*0.03232*	*0.00868*	*0.00206*	*31.1199046*	*3689.6*	*299.82*	*1148.2*	*174.38*	*2336.7*	*155.13*	*174.6*	*41.2*
R4-JA	*0.31968*	*0.0395*	*6.07242*	*0.59751*	*0.14628*	*0.01239*	*0.02454*	*0.00555*	*24.66440602*	*3568.3*	*178.09*	*880.1*	*69.66*	*1986.3*	*85.78*	*490.1*	*109.43*
R4-H	*0.15833*	*0.02288*	*2.8976*	*0.36615*	*0.13493*	*0.0107*	*0.02944*	*0.00826*	*33.46732844*	*2437.9*	*226.05*	*815.9*	*60.77*	*1381.3*	*95.39*	*586.6*	*162.27*
R4-GB	*0.19153*	*0.02327*	*6.42743*	*0.67586*	*0.25591*	*0.01934*	*0.00782*	*0.00161*	*53.30986427*	*2755.4*	*186.73*	*1468.9*	*99.28*	*2036*	*92.4*	*157.4*	*32.29*
R4-GA	*0.05884*	*0.0065*	*0.6978*	*0.0715*	*0.0867*	*0.004*	*0.0122*	*0.00562*	*95.52664409*	*561.1*	*224.2*	*536*	*23.76*	*537.5*	*42.76*	*245*	*112.24*
R4-F	*0.04533*	*0.00617*	*0.5936*	*0.07648*	*0.09746*	*0.00476*	*0.02776*	*0.00388*	*599500*	*0.1*	*262.99*	*599.5*	*27.99*	*473.2*	*48.73*	*553.4*	*76.32*
R4-DB	*0.06011*	*0.0054*	*0.66843*	*0.05664*	*0.08099*	*0.00279*	*0.01084*	*0.00157*	*82.63374486*	*607.5*	*183.24*	*502*	*16.61*	*519.8*	*34.47*	*217.8*	*31.32*
R4-D	0.06175	0.00188	0.6597	0.01943	0.07749	0.00117	0.02933	0.00905	72.30237451	665.4	63.88	481.1	6.98	514.4	11.89	584.4	177.67
R4-C	*0.06042*	*0.00949*	*0.68962*	*0.09822*	*0.08282*	*0.00604*	*0.00232*	*0.00063*	*82.91302942*	*618.6*	*307.12*	*512.9*	*35.96*	*532.6*	*59.03*	*46.8*	*12.71*
R4-B	0.06266	0.00827	0.63071	0.07688	0.07382	0.00407	0.00624	0.00126	65.87745731	696.9	258.52	459.1	24.43	496.5	47.87	125.6	25.21
R4-AG	0.05936	0.01146	0.68563	0.1258	0.08367	0.00553	0.04111	0.00751	89.2641737	580.3	371.91	518	32.87	530.2	75.78	814.3	145.73
R4-AC	*0.06127*	*0.00947*	*0.65058*	*0.09542*	*0.0772*	*0.00416*	*0.00886*	*0.00237*	*73.91304348*	*648.6*	*301.29*	*479.4*	*24.89*	*508.8*	*58.7*	*178.3*	*47.5*
R4-AB	*0.05349*	*0.01082*	*0.69054*	*0.12643*	*0.09328*	*0.00881*	*0.03365*	*0.00893*	*164.4921316*	*349.5*	*402.26*	*574.9*	*51.95*	*533.1*	*75.93*	*669*	*174.64*
R4-AA	*0.06439*	*0.00699*	*0.68112*	*0.06765*	*0.07674*	*0.00371*	*0.02543*	*0.01337*	*63.15928969*	*754.6*	*213.8*	*476.6*	*22.22*	*527.5*	*40.86*	*507.5*	*263.48*
R1A-8AA	*0.064*	*0.00726*	*1.07869*	*0.11555*	*0.1233*	*0.00534*	*0.09191*	*0.022*	*101.0788941*	*741.5*	*223.2*	*749.5*	*30.63*	*743*	*56.44*	*1777.2*	*407.26*
R1A-8A	*0.04882*	*0.00824*	*0.62353*	*0.09792*	*0.09208*	*0.00631*	*0.00429*	*0.00076*	*407.9022989*	*139.2*	*354.08*	*567.8*	*37.27*	*492.1*	*61.24*	*86.6*	*15.29*

R1A-6B	*0.09562*	*0.01634*	*0.95086*	*0.14942*	*0.07552*	*0.00546*	*0.01042*	*0.00078*	*30.4661127*	*1540.4*	*291.21*	*469.3*	*32.75*	*678.6*	*77.77*	*209.5*	*15.62*
R1A-5C	0.05886	0.00503	0.67749	0.05504	0.08396	0.00266	0.0134	0.0023	92.45685821	562.1	175.92	519.7	15.81	525.3	33.31	269	45.89
R1A-5BB	0.06185	0.00327	0.64226	0.0325	0.0754	0.00161	0.01293	0.00339	70.0553147	668.9	109.25	468.6	9.66	503.7	20.09	259.7	67.7
R1A-5BA	*0.05962*	*0.00898*	*0.67053*	*0.09546*	*0.08236*	*0.00449*	*0.03349*	*0.00612*	*86.50389963*	*589.8*	*296.99*	*510.2*	*26.76*	*521*	*58.02*	*665.9*	*119.6*
R1A-5AB	0.06044	0.00633	0.5564	0.05482	0.06703	0.00266	0.51118	0.11959	67.50605327	619.5	211.08	418.2	16.04	449.2	35.76	8345.5	1599.48
R1A-5A	*0.05985*	*0.00813*	*0.63675*	*0.08176*	*0.07723*	*0.00383*	*0.4085*	*0.09988*	*80.18394649*	*598*	*269.94*	*479.5*	*22.9*	*500.3*	*50.72*	*6923.2*	*1433.24*
R1A-4A	0.05706	0.0033	0.55671	0.03073	0.07103	0.00159	0.32133	0.06511	89.69783005	493.1	123.26	442.3	9.58	449.4	20.05	5631.9	996.03
R1A-2A	*0.05319*	*0.00669*	*0.60879*	*0.07241*	*0.08301*	*0.00382*	*0.3838*	*0.14423*	*152.6581527*	*336.7*	*262.42*	*514*	*22.74*	*482.8*	*45.7*	*6565.6*	*2106.64*
R1A-10ED	*0.04607*	*0.00454*	*0.45344*	*0.04255*	*0.07154*	*0.00244*	*0.0159*	*0.00234*	*445400*	*0.1*	*222.89*	*445.4*	*14.7*	*379.7*	*29.72*	*318.9*	*46.63*
R1A-10EC	*0.06125*	*0.00736*	*0.55628*	*0.06286*	*0.06601*	*0.00299*	*0.01105*	*0.00198*	*63.59567901*	*648*	*239.13*	*412.1*	*18.07*	*449.1*	*41.01*	*222.2*	*39.66*
R1A-10EB	*0.05467*	*0.00322*	*0.56463*	*0.03182*	*0.07497*	*0.00171*	*0.02*	*0.00369*	*116.8212585*	*398.9*	*126.66*	*466*	*10.25*	*454.5*	*20.65*	*400.3*	*73.12*
R1A-10E	0.05881	0.00392	0.63798	0.04032	0.07877	0.00204	0.02267	0.00701	87.28571429	560	138.86	488.8	12.18	501.1	25	453	138.63
R1A-10C	0.05663	0.00292	0.66374	0.03258	0.08531	0.00182	0.01463	0.00217	110.7660021	476.5	110.74	527.8	10.8	516.9	19.89	293.6	43.26
R1A-10A	0.05592	0.00535	0.64244	0.05856	0.08346	0.00285	0.00525	0.00092	115.1548919	448.7	200	516.7	16.93	503.8	36.2	105.9	18.41
G1A-9B	*0.14332*	*0.03899*	*1.21141*	*0.30079*	*0.0619*	*0.00713*	*0.00212*	*0.00015*	*17.07456895*	*2267.7*	*406.32*	*387.2*	*43.29*	*805.8*	*138.11*	*42.8*	*3.09*
G1A-9A	0.06846	0.01169	0.75167	0.12629	0.07983	0.00303	0.00396	0.00069	56.10834089	882.4	318.17	495.1	18.07	569.2	73.2	80	13.92
G1A-8A	0.04904	0.00798	0.52546	0.08436	0.07814	0.0031	0.0199	0.00841	323.76502	149.8	341.88	485	18.53	428.8	56.15	398.4	166.67
G1A-7B2	0.04803	0.00799	0.49079	0.07995	0.07414	0.00328	0.00079	0.00008	458.250497	100.6	352.13	461	19.7	405.5	54.45	16	1.65
G1A-7B1	0.05484	0.02154	0.67095	0.25999	0.08878	0.00632	0.04706	0.0072	135.149125	405.7	699.35	548.3	37.43	521.3	157.98	929.6	139.04
G1A-7A	0.05963	0.01082	0.6405	0.11367	0.07783	0.00393	0.03404	0.02896	81.85668304	590.3	351.35	483.2	23.53	502.6	70.36	676.5	566.12
G1A-5C2	0.06099	0.00771	0.62703	0.07828	0.07465	0.00244	0.02088	0.00442	72.64047582	638.9	250.92	464.1	14.61	494.2	48.85	417.8	87.59
G1A-5C1	*0.03505*	*0.00726*	*0.36126*	*0.07339*	*0.07474*	*0.00378*	*0.00172*	*0.0008*	*464600*	*0.1*	*0*	*464.6*	*22.64*	*313.2*	*54.74*	*34.8*	*16.06*
G1A-5B1	0.06179	0.00492	0.68036	0.05308	0.08475	0.00188	0.00706	0.00102	78.64427115	666.8	161.96	524.4	11.16	527	32.08	142.2	20.49
G1A-3A2	0.0648	0.01048	0.79677	0.11425	0.09504	0.00369	0.01002	0.00167	76.22086209	767.9	308.07	585.3	21.72	595	64.56	201.5	33.33
G1A-3A1	0.06423	0.01014	0.75463	0.11677	0.08516	0.00331	0.01826	0.00566	70.31500267	749.2	302.41	526.8	19.64	570.9	67.58	365.8	112.27
G1A-1A2	*0.10294*	*0.04656*	*0.97667*	*0.14355*	*0.06855*	*0.00779*	*0.00298*	*0.00044*	*25.47535316*	*1677.7*	*662.4*	*427.4*	*46.97*	*691.9*	*223.71*	*60.1*	*8.85*
G1A-1A1	*0.07366*	*0.01411*	*0.78757*	*0.14051*	*0.0785*	*0.00536*	*0.00775*	*0.00125*	*47.19046696*	*1032.2*	*345.34*	*487.1*	*32.06*	*589.8*	*79.81*	*155.9*	*25.17*
G1A-1A	*0.05029*	*0.00941*	*0.56259*	*0.10094*	*0.08189*	*0.00428*	*0.06747*	*0.0446*	*243.4740883*	*208.4*	*384.71*	*507.4*	*25.49*	*453.2*	*65.59*	*1319.7*	*844.56*
G1A-15B	0.05549	0.01003	0.63446	0.11209	0.08299	0.00353	0.02121	0.006	119.0917516	431.6	359.42	514	20.99	498.9	69.64	424.3	118.74
G1A-15A2	0.05898	0.00629	0.63987	0.06685	0.07872	0.00226	0.00841	0.00134	86.26169875	566.3	216.66	488.5	13.49	502.2	41.39	169.2	26.96
G1A-15A	0.05492	0.00538	0.56612	0.05446	0.07479	0.0021	0.01751	0.00393	113.69528	408.9	205.48	464.9	12.57	455.5	35.31	350.8	78.12
G1A-14A	*0.02398*	*0.00793*	*0.28387*	*0.09257*	*0.08633*	*0.00538*	*0.00259*	*0.00039*	*533800*	*0.1*	*0*	*533.8*	*31.92*	*253.7*	*73.21*	*52.3*	*7.78*
G1A-12E	*0.03934*	*0.00459*	*0.3867*	*0.04633*	*0.07122*	*0.00247*	*0.01515*	*0.0057*	*443500*	*0.1*	*0*	*443.5*	*14.86*	*332*	*33.92*	*304*	*113.55*
G1A-12D	0.05591	0.01119	0.61412	0.1274	0.07873	0.00387	0.00936	0.00181	108.9429081	448.4	392.33	488.5	23.14	486.2	80.14	188.3	36.2

G1A-12B	0.05592	0.00634	0.70239	0.08016	0.09104	0.00296	-0.09689	0.0495	125.1280909	448.9	234.33	561.7	17.52	540.2	47.81	******	1107.76
G1A-12A	0.0625	0.0084	0.69142	0.07802	0.08122	0.00459	0.01361	0.00317	72.82986111	691.2	263.39	503.4	27.39	533.7	46.84	273.2	63.13
G1A-10C	0.05778	0.00932	0.6275	0.09488	0.08024	0.00308	0.00964	0.00259	95.47111879	521.1	319.74	497.5	18.4	494.5	59.19	193.8	51.78
G1A-10B	0.04972	0.00758	0.49243	0.07139	0.0725	0.00287	0.02311	0.00379	247.9120879	182	320.59	451.2	17.23	406.6	48.57	461.7	74.84
G1A-10A	*0.03909*	*0.00441*	*0.3905*	*0.04294*	*0.07231*	*0.00226*	*0.00857*	*0.00155*	*450000*	*0.1*	*0*	*450*	*13.6*	*334.7*	*31.36*	*172.5*	*31.02*

U-Pb standard information

Primary zircon standard used was GJ, with a 1% uncertainty assigned (TIMS normalisation data: $^{207}Pb/^{206}Pb$ = 608.3 Ma, $^{206}Pb/^{238}U$ = 600.7Ma and $^{207}Pb/^{235}U$ = 602.2 Ma; (Payne et al. 2008). Weighted averages for primary zircon standard GJ over the two LA-ICP-MS sessions were: $^{207}Pb/^{206}Pb$ = 617±28 Ma (n = 115, MSWD = 2.3), $^{206}Pb/^{238}U$ = 608±12 Ma (n = 115, MSWD = 33), and $^{207}Pb/^{235}U$ = 613±12 Ma (n = 115, MSWD = 9.3). Weighted averages for in-house secondary zircon standard PLES were: $^{207}Pb/^{206}Pb$ = 371±40 Ma (n = 24, MSWD = 0.5), $^{206}Pb/^{238}U$ = 336±18 Ma (n = 24, MSWD = 48), and $^{207}Pb/^{235}U$ = 338±17 Ma (n = 24, MSWD = 9.3).

APPENDIX 4: WHOLE ROCK GEOCHEMISTRY

Whole rock geochemistry methods

Whole rock geochemical analyses were undertaken by Wavelength Dispersive X-ray Fluorescence (WD–XRF) spectrometry for samples RB11 and PB16, at the Department of Earth and Environment, Franklin and Marshal College, Lancaster PA, USA. Ferric vs ferrous iron content was determined by titration, whereas major elements were analysed on fused disks prepared using a lithium tetraborate flux.

Whole rock bulk chemistry results. Total iron is analysed and presented as ferric iron.

	RB11	PB16
SiO_2	45.26	44.83
TiO_2	1.25	2.18
Al_2O_3	18.98	13.79
Fe_2O_3T	15.09	14.76
MnO	0.61	0.29
MgO	4.33	6.88
CaO	4.79	13.78
Na_2O	0.65	3.43
K_2O	5.26	0.11
P_2O_5	0.19	0.28
Total	99.96	100.33
LOI	4.85	7.21

APPENDIX 5: GEOCHEMICAL PLOTS AND GRAPHS
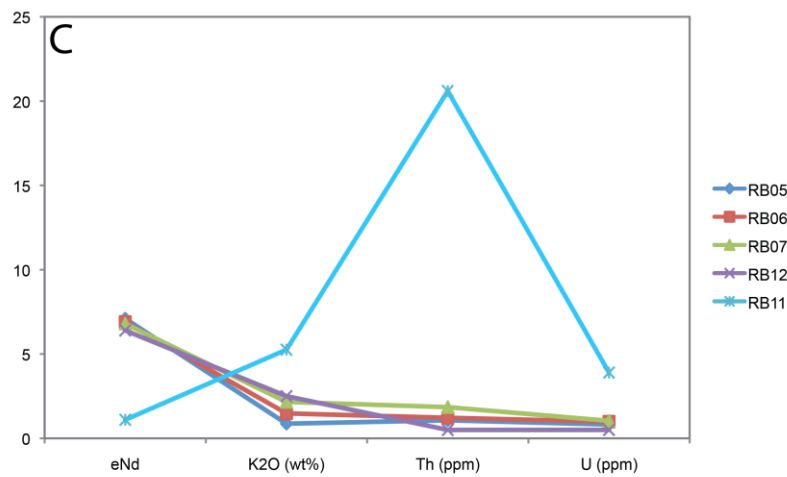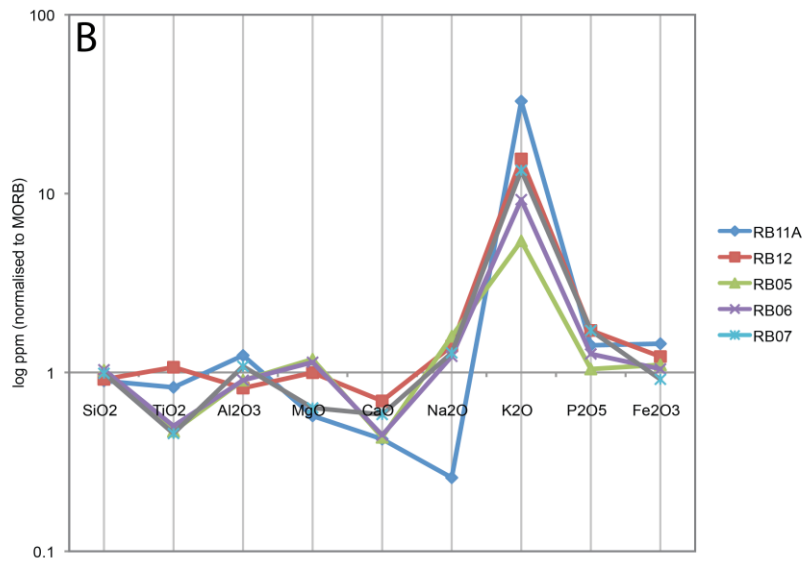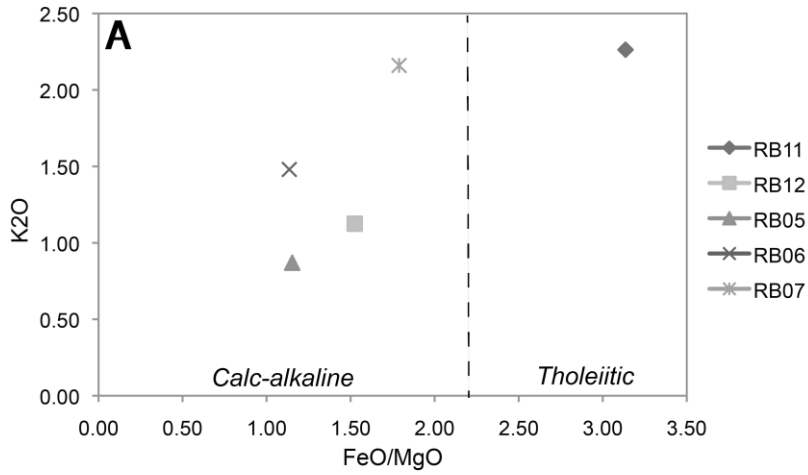
APPENDIX 6: DETRITAL ZIRCON DATA FROM ROCKY BEACH AND TOWN BEACH, PORT MACQUARIE